UNIVERSITA' DEGLI STUDI DI PAVIA

FACOLTA' DI INGEGNERIA
DIPARTIMENTO DI INGEGNERIA INDUSTRIALE E DELL'INFORMAZIONE

DOTTORATO DI RICERCA IN BIOINGEGNERIA E BIOINFORMATICA
XXXVII CICLO - 2024

MODEL-INFORMED DRUG DEVELOPMENT IN ONCOLOGY: HARNESSING PATIENT-DERIVED XENOGRAFT MODELS FOR CLINICAL PREDICTION AND SUPPORT OF TREATMENT OUTCOMES

PhD Thesis by

DAVIDE RONCHI

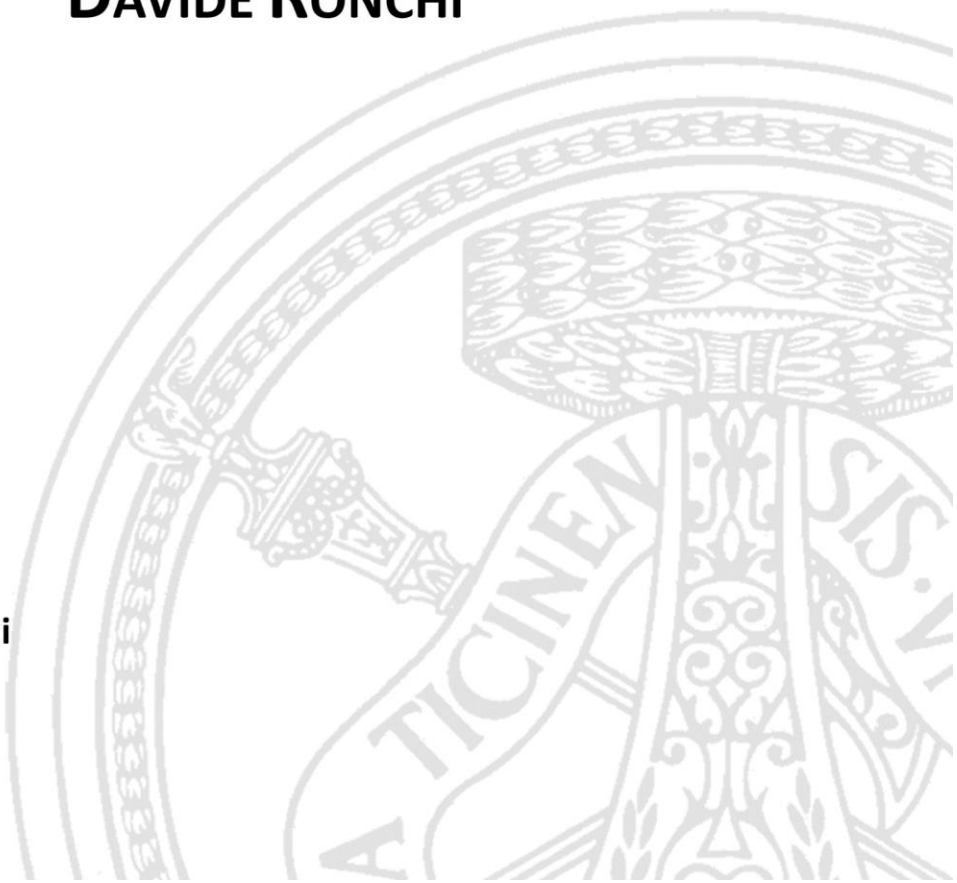

Advisor:
Prof. Paolo Magni

PhD Program Chair:
Prof. Silvana Quaglini

Acknowledgments

Abstract (Italiano)

In questa tesi è stato sviluppato e poi applicato un framework di modellistica traslazionale che ha lo scopo di predire la crescita tumorale e le curve di progressione della patologia (PFS) in pazienti affetti da tumore tramite l'utilizzo di dati preclinici derivanti da esperimenti effettuati su topi immunosoppressi derivati da paziente (PDX). Il framework ha permesso di predire accuratamente le dinamiche tumorali sia in pazienti non trattati che in pazienti trattati. Per quanto riguarda il caso senza trattamento, la validazione è stata condotta confrontando i tempi di raddoppiamento del volume tumorale (TVDT) e le PFS predetti con quelli osservati su un pannello di undici diverse tipologie di tumori. Due casi di studio sono invece stati utilizzati per validare la predizione delle dinamiche tumorali e la predizione delle PFS nel caso di pazienti trattati, i.e., tumore al pancreas trattato con Gemcitabina e carcinoma epatocellulare (HCC) trattato con Sorafenib. In seguito allo sviluppo dell'approccio traslazionale, abbiamo esplorato le sue potenziali applicazioni nella pratica clinica, proponendo due applicazioni testate nello scenario HCC-Sorafenib.

La prima applicazione ha come obiettivo quello di innovare il design dei trial oncologici tramite l'integrazione di pazienti virtuali, generati a partire da modelli preclinici PDX, attraverso l'approccio traslazionale sviluppato, in bracci di controllo ibridi tramite tecniche di *dynamic borrowing*. Essi possono essere una alternativa all'utilizzo di pazienti coinvolti in studi clinici diversi da quello in analisi. È stato dimostrato che, nel caso di studio in analisi, l'approccio sviluppato è stato in grado di replicare i risultati osservati utilizzando bracci di controllo tradizionali, riducendo la necessità di arruolare molti pazienti, e migliorando l'efficienza e la sostenibilità della sperimentazione oncologica. La seconda applicazione si colloca nell'ambito della modellizzazione bayesiana congiunta delle dinamiche tumorali e degli esiti di sopravvivenza. Utilizzando il framework per costruire distribuzioni a priori informative, questo approccio è stato in grado di migliorare l'accuratezza e diminuire i tempi computazionali. Queste applicazioni dimostrano il potenziale del framework per migliorare la ricerca clinica e la sua rilevanza più ampia in oncologia.

Abstract (English)

This thesis develops and applies a translational modeling framework aimed at predicting tumor growth and progression-free survival (PFS) in cancer patients by leveraging preclinical data from patient-derived xenograft (PDX) mouse models. The framework successfully predicts tumor dynamics in both untreated and treated patients. Validation was conducted comparing predicted tumor volume doubling time (TVDT) and PFS across eleven different cancer types for the untreated predictions. Two case studies, i.e., pancreatic cancer treated with Gemcitabine and hepatocellular carcinoma (HCC) treated with Sorafenib, were used to validate tumor dynamics and PFS predictions for patients receiving treatment.

Following the development of the translational approach, we explored its potential applications in clinical practice, proposing two applications tested in the HCC and Sorafenib scenario.

The first application focuses on innovating clinical trial design by integrating virtual patients generated from PDX mouse data into hybrid control arms, as an alternative to historical patients, using *dynamic borrowing* techniques. This approach closely replicates the outcomes of traditional control arms while reducing the need for large patient enrollments, potentially enhancing the efficiency and feasibility of cancer trials.

The second application advances the development of Bayesian joint modeling of tumor dynamics and survival outcomes. By utilizing informative priors derived from preclinical data, this approach enhances the accuracy and speed of parameter estimation in complex models, offering a more robust and data-informed method for predicting clinical outcomes. These applications demonstrate the framework's potential to improve clinical research and its broader relevance in oncology.

Contents

Chapter 1

Introduction

Cancer is a leading cause of death globally and presents a significant barrier to increasing life expectancy. According to the World Health Organization (WHO) in 2019, cancer was the primary cause of death before age 70 in 112 out of 183 countries and ranked third or fourth in another 23 countries [1]. This rise in cancer mortality can be partly attributed to the notable decline in deaths from stroke and coronary heart disease respect to cancer in many regions [2]. However, recent medical advancements have resulted in declining absolute mortality rates. According to the American Cancer Society's Cancer Statistics 2023 report, overall cancer mortality has decreased by 33% since 1991 [3]. Improvements in cancer prevention, early detection, and development of novel anti-cancer therapies have significantly contributed to this decline in death rates. However, the development of new and more effective treatment is still an urgent need.

1.1. Drug development in oncology

1.1.1. Stages of oncology drug development

Drug discovery and development is a long, complicated and expensive process aiming to bring safe and effective new treatments to the patients [4]. Although, the entire process can be divided into different phases [5, 6] (summarized in Figure 1.1), it is highly integrated, with overlap and sharing of information across phases that are described hereafter.

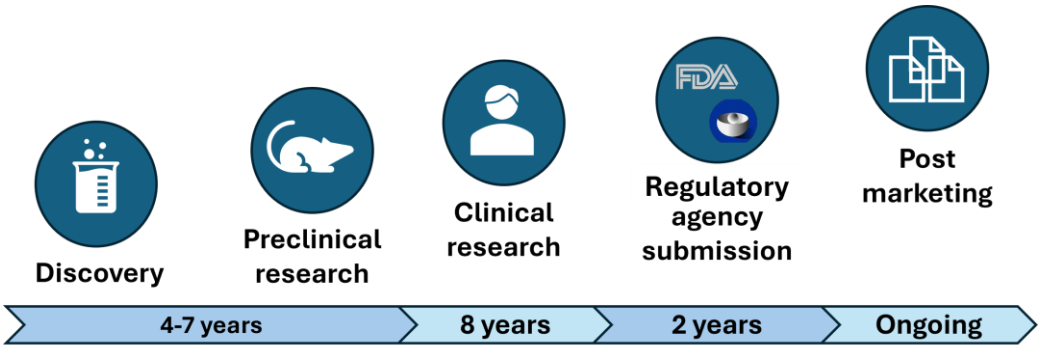

Figure 1.1 The drug discovery and development process

During the discovery process, the most promising compounds are selected based on their potential to target specific biomarkers or mutations in cancer cells [7]. The first step in drug development begins with preclinical studies, which are essential for evaluating the safety and efficacy of potential treatments before they are tested in humans, particularly in the context of cancer research [8]. These preliminary investigations are conducted using in vitro experiments or animal models to comprehensively assess pharmacokinetics (PK), pharmacodynamics (PD), and potential toxicity profiles [9]. The primary objectives of preclinical studies include establishing a safe starting dose that also demonstrates therapeutic promise, identifying any potential adverse effects on organs, and determining whether these effects are reversible.

Phase I clinical trials (typically involving 20-50 patients) mark the crucial transition from preclinical testing to the first administration of a drug in humans and represent a pivotal stage in drug development. Phase I trials in oncology primarily aim to establish the tolerability of investigational agents across a diverse patient population with various solid tumors. The assumption is that tolerance to the drug would be consistent regardless of tumor origin, disease stage, or prior treatments. In addition to safety and tolerability, these trials include PK assessments to understand the drug absorption, distribution, metabolism, and excretion in humans. Data from these trials are used to determine a recommended Phase II dose and assess initial safety, guiding further testing [5, 10, 11].

Phase II clinical trials (typically involving 30-100 patients) are designed to assess whether a treatment demonstrates sufficient activity or promise of efficacy to warrant further investigation in a Phase III trial. These trials usually involve a homogeneous cohort of participants with the same type of cancer. The primary objectives include evaluating treatment efficacy through endpoints such as tumor response rates or progression-free survival, identifying responsive cancer types, refining optimal dosages, and further

exploring safety and tolerability profiles. Additionally, Phase II trials continue to include PK assessments to further refine dosing strategies and better understand the behavior of the drug in the body. Phase II trials may also include exploratory assessments like biomarker analysis to enhance understanding of treatment mechanisms and potential benefits [5, 12].

Phase III clinical trials (typically involving multiple hundreds of patients) are pivotal in clinical research, aiming to provide conclusive evidence on how new treatments compare to the current standard-of-care. These trials involve significantly larger cohorts of patients compared to Phase I or Phase II trials, often enrolled across multiple hospitals and countries. The primary objective is to determine which treatment option offers superior efficacy for specific types of cancer, while also thoroughly assessing side effects and their impact on patients' quality of life [5, 12, 13].

Following the successful completion of Phase III trials, the next critical step is Regulatory Review and Approval. This involves the submission of a New Drug Application (NDA) or a Biologics License Application (BLA) to regulatory bodies such as the FDA or EMA. These agencies meticulously review the submitted clinical trial data, manufacturing processes, and labeling information to ensure the drug safety, efficacy, and quality. This phase is crucial as it determines whether a drug can be marketed and made available to the public, signifying the transition from experimental treatment to standard therapy for patients [5, 14].

Finally, Phase IV trials (Post-Marketing Surveillance) focus on the long-term safety and effectiveness of a drug once it is on the market. These trials aim to monitor adverse effects in the broader population and gather information on the drug performance in real-world settings. This phase is essential for detecting rare or long-term side effects that may not have been evident in earlier trials [5, 15].

1.1.2. Challenges in oncology drug development

The current model for developing oncology drugs is marked by high attrition rates, with average cost estimates ranging from $765 million to $4.6 billion (in 2020 US dollars) [16, 17]. The likelihood of a compound moving from initial clinical evaluation to market entry is less than 5%, highlighting the difficulties in oncology drug development and the disparities between positive preclinical results and later challenges in patient trials.

Indeed, the development of oncology drugs presents unique challenges compared with treatments for other diseases [18]. For instance, cancer patients differ significantly from healthy individuals in demographics and physiology, which can alter the PK profile of drugs. Additionally, cancer patients typically take multiple medications to manage not only their cancer but also comorbidities and treatment-associated side effects, increasing the risk of drug-drug interactions and other safety issues.

Furthermore, historically, cancer treatment has relied heavily on cytotoxic chemotherapy drugs, leading to standard practices focused on identifying the maximum tolerated dose and using toxicity-guided regimens [19]. In contrast, modern therapies emphasize targeted treatments, including small-molecule agents, monoclonal antibodies, immuno-oncology options, and their combinations. The development of these new drugs departs from the previous cytotoxic paradigm, emphasizing targeted activity and toxicity/efficacy-guided dose determination rather than only toxicity-guided dose determination [20–23]. To support this transition, more sophisticated preclinical models able to mimic the complexity of human cancers more accurately, and enhanced translational approaches are essential.

However, despite these advancements in cancer drug development, a significant challenge remains in translating preclinical success into clinical efficacy. One of the most critical issues is the high attrition rate in drug development, where 95% of drugs are discarded between initial human testing and approval [24]. Although many new cancer drugs show promise in the preclinical and early clinical phases, predicting their success across all clinical phases is highly complex. Phase II, in particular, has the lowest success rate, with only about 36% of drugs advancing beyond this stage [25]. This low success rate underscores a critical issue: the therapeutic index hypothesis established during preclinical studies often fails to translate effectively to the clinical setting. Consequently, predictions regarding a drug efficacy and safety in early-stage trials frequently do not align with outcomes in later clinical phases. Several factors contribute to these challenges. Notably, the reproducibility of preclinical findings is often limited due to the inherent complexity of cancer biology and constraints associated with preclinical research tools. Additionally, evaluations of tumor response in preclinical models frequently rely on metrics such as tumor size reduction following animal sacrifice, which may not accurately reflect the drug impact on overall survival [25].
Furthermore, the transition from preclinical experiments to clinical trials underscores the need for precise endpoint selection tailored to trial phases. Early-phase trials generally focus on safety and biological activity, while later-phase trials are designed to assess clinical benefits such as survival

extension. For instance, early trials may investigate whether a drug reduces tumor size, whereas later trials aim to determine whether the drug translates into prolonged patient survival. This shift in focus from early efficacy indicators to ultimate clinical outcomes illustrates the critical gap between preclinical predictions and clinical realities, further emphasizing the challenges in bridging the preclinical to clinical gap.

1.1.3. Cancer models in preclinical research

Experimental systems for studying human cancer encompass a variety of models, including 2D cancer cell cultures, 3D cultures, and living organisms such as zebrafish, xenograft mouse models, and genetically engineered mouse models (Figure 1.3), among others [26]. These diverse models serve as essential tools for investigating the biochemical and genetic pathways involved in cancer, as well as understanding its underlying pathology [27].

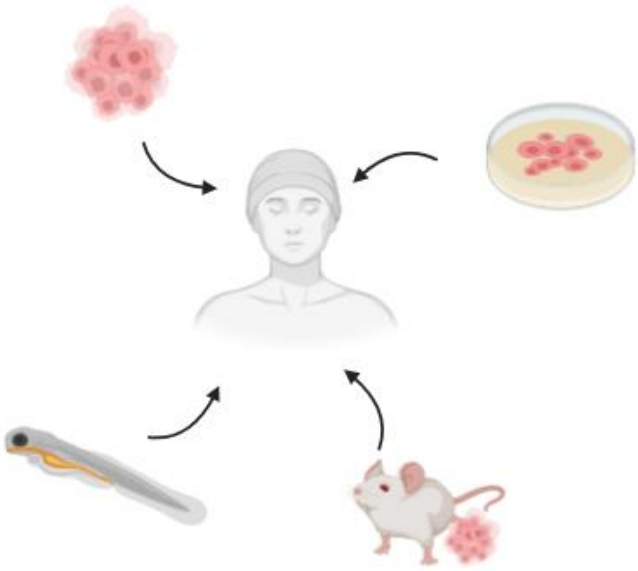

Figure 1.3 Preclinical cancer models.

2D Cancer Cell Cultures 2D cancer cell cultures are widely used as in vitro tumor models in oncology. They retain many intrinsic characteristics of cancer and demonstrate similar gene expression patterns to primary human tumors. Their copy number alterations and transcriptional profiles exhibit genomic changes comparable to those found in primary human tumors [28, 29]. 2D cell cultures are the primary preclinical cancer model due to their ease of management, low cost, immortality, limited cellular heterogeneity, and high proliferation rates [26].

3D In Vitro Models 3D in vitro cancer models are emerging as a promising approach to bridge the gap between traditional 2D cell cultures and animal models. Various 3D models, including spheroids and organoids, have been developed, each differing in tumor cell sources, culture protocols, and establishment time. These models offer several advantages over 2D cell cultures, as they more accurately replicate in vivo tumor features. These include natural tumor architecture, cell–cell interactions, nutrient and oxygen gradients, drug penetration and resistance, and, to varying degrees, the tumor microenvironment [30, 31].

Zebrafish Models A recent promising model for studying human cancer is the zebrafish. Several normal human tumor types have been modeled in zebrafish using transgenesis, demonstrating that the molecular mechanisms underlying mammalian tumorigenesis also apply in zebrafish. Zebrafish cancer models are particularly useful for identifying novel cancer markers, differentiating between molecular prognostic biomarkers, and establishing their roles in disease development. Their small size, large clutch size, low cost, ability to generate hundreds of embryos from a single mating, translucent embryos, and ex utero growth enhance their utility as a cancer model [32–34].

Xenograft Models Xenograft models are among the most used animal models, in which tumor cells from standardized cell lines are inoculated subcutaneously into immunocompromised animals, typically mice or rats. Despite ongoing debates about their validity, xenograft models remain popular due to their significant advantages: experiments are easy to reproduce, and they allow for the evaluation of the behavior and response of various tumor lines [35, 36]. To develop a model that more closely mimics human tumors and overcome the limitations of standard xenograft models, patient-derived tumor xenografts (PDXs) have emerged as valuable tools for translational research. In PDX studies, small fragments of primary tumors surgically excised from cancer patients are implanted into highly immunocompromised mice, allowing for the growth of tumors that closely mimic the original patient tumors in terms of histology and genetic profile. This model maintains the tumor cellular heterogeneity and microenvironment, providing a more accurate representation of the human disease. PDXs are particularly valuable for evaluating the efficacy of novel therapies, understanding tumor evolution, and studying patient-specific responses to treatment [37–40].

Genetically Engineered Mouse Models (GEMMs) Since the innate characteristics and physiology of xenografts do not fully capture the genetic

characteristics of human tumors, genetically engineered mouse models (GEMMs) have been established. Advances in technology over recent decades have enabled researchers to make specific alterations in the genome of mice, conditionally or constitutively changing the expression of important genes that lead to the development of specific tumors. GEMMs have provided insights into oncogenesis by elucidating molecular pathways, and their genomes can be manipulated to achieve loss or gain of oncogene or tumor suppressor gene function. The effects of these genetic changes are reflected in tumor phenotype, and GEMMs have proven valuable for validating key genes as therapeutic targets [41, 42].

1.1.4. Tumor Growth Experiments in Xenograft Mouse Models

In xenograft mouse experiments, tumor fragments are implanted subcutaneously into immunocompromised mice. Once the tumors reach a palpable size, typically around 0.1-0.2 cm^3, the animals are randomized into groups, with some receiving the test compound and others serving as controls. These studies, known as tumor growth inhibition (TGI) studies, are designed to evaluate the anticancer effectiveness of treatments by comparing tumor growth between the treated and control groups.

Tumor dimensions (length and width) are measured by caliper, typically from once a day to every 4 days, and tumor mass calculated as:

$$weight = \frac{\rho_{tr}(length \cdot width^2)}{2}$$

approximating tumor shape with the ellipsoid generated by the rotation of a semi-ellipse around its larger axis (length) and assuming unit density ($\rho_{tr} = 1\frac{g}{cm^3}$).

Drug administrations can differ for dosages, duration of treatment, schedule (number and time of administrations), way of administration (i.e. Intra-Venous, Intra-Peritoneal, Oral, etc.) and administration profile (bolus or infusion).

Key endpoints in these studies include the percentage of tumor growth inhibition (TGI%) at specific time points, the tumor growth delay (TGD), which measures the time difference for tumors to reach a defined size between treated and control groups, the dose required to achieve a particular level of inhibition, such as TGI50 (50% tumor growth inhibition), and the threshold concentration for tumor eradication C_t that represent the hypothetical steady-state drug concentration that, if reached, enables tumor eradication.

1.1.5. Clinical trial endpoints

Clinical trials in oncology are designed to answer specific questions, such as whether one drug is more effective than another at preventing a particular event. These trials focus on assessing the efficacy and safety of new cancer treatments through various endpoints, providing valuable insights into the therapeutic benefits and risks of these interventions [43]. A clinical endpoint is an objective metric measuring how beneficial a medical intervention is to a patient's feeling, function, and survival. Clinical endpoints are used in clinical trials to assess validity and generalizability of the study, and the evidence they generate is important to clinicians and patients alike. Clinical endpoints also have the capacity to evaluate the outcomes of using a medical intervention to guide clinical decision making. Endpoints in clinical trials are classified as either primary or secondary, based on their relevance to the study's objectives. The primary endpoint is directly linked to the primary objective of the trial and is designed to answer the main research question. Secondary endpoints, on the other hand, provide additional information by either supporting the primary objective or addressing secondary objectives [44, 45].
Following FDA guidelines [46], but limiting to the purposes of this thesis, the endpoints that are discussed in this section include only overall survival (OS) and progression-free-survival (PFS). Additional relevant endpoints such as other tumor-based assessment endpoints (i.e, objective response rate, disease free survival), endpoints involving symptom assessment or endpoints based on blood or body-fluid biomarkers, are not considered in this discussion.

Overall Survival (OS) OS is defined as the time from randomization until death from any cause and is measured in the intent-to-treat population (i.e, the set of all randomized patients included in the trial). OS is considered the most reliable endpoint in cancer trials because it directly reflects patient survival and is straightforward to measure, with death dates well-documented. Since the endpoint is objective, it is not susceptible to bias in measurement. When feasible, OS is typically the preferred endpoint for evaluating the clinical benefit of cancer therapies [43]. OS is best evaluated in randomized controlled trials (RCTs), as data from externally controlled trials are usually poorly reliable for overall survival. Challenges in survival studies include long follow-up periods and the potential for subsequent cancer treatments to affect survival analysis.

Progression-Free Survival (PFS) PFS measures the time between study randomization and either tumor progression or death, providing an indication

of how effectively a treatment can halt or slow disease progression [47]. PFS can reflect tumor growth and be assessed before the determination of a survival benefit. Its determination is not confounded by subsequent therapy. Treatment effect measured by PFS can be a surrogate endpoint to support accelerated approval, a surrogate endpoint to support traditional approval, or it can represent direct clinical benefit [48, 49].

For the PFS evaluation, it is important to carefully define tumor progression criteria in the protocol. There are no standard regulatory criteria for defining progression, and during the drug submission process, various criteria have been used, including RECIST (Response Evaluation Criteria in Solid Tumors) criteria [50].

RECIST provides standardized criteria for evaluating changes in tumor size and defines specific thresholds for categorizing responses to treatment. For solid tumor, tumor size is generally quantified by measuring the sum of the longest diameter (SLD) of target lesions [50]. The definitions of the criteria used to determine objective tumor response for solid tumors are reported in Table 1.1.

Table 1.1 RECIST criteria for solid tumors.

Name	Acronym	Description
Complete Response	CR	Disappearance of all target lesions. Any pathological lymph nodes (whether target or non-target) must have reduction in short axis to <10 mm.
Partial Response	PR	At least a 30% decrease in the sum of diameters of target lesions, taking as reference the baseline sum diameters.
Progressive Disease	PD	At least a 20% increase in the sum of diameters of target lesions, taking as reference the smallest sum on study. In addition to

Name	Acronym	Description
		the relative increase of 20%, the sum must also demonstrate an absolute increase of at least 5 mm. (Note: the appearance of one or more new lesions is also considered progression).
Stable Disease	SD	Neither sufficient shrinkage to qualify for PR nor sufficient increase to qualify for PD, taking as reference the smallest sum diameters while on study.

1.2. Model-Informed Drug Development in oncology

Model-Informed Drug Development (MIDD) can be defined as the use of mathematical models and simulations to support the key program decisions [51]. It is characterized by a learn and confirm paradigm which is shown in Figure 1.2 along with several application in different context. In recent years, there has been an increased trend in the development and incorporation of MIDD approaches into new policy and regulatory guidance [52].

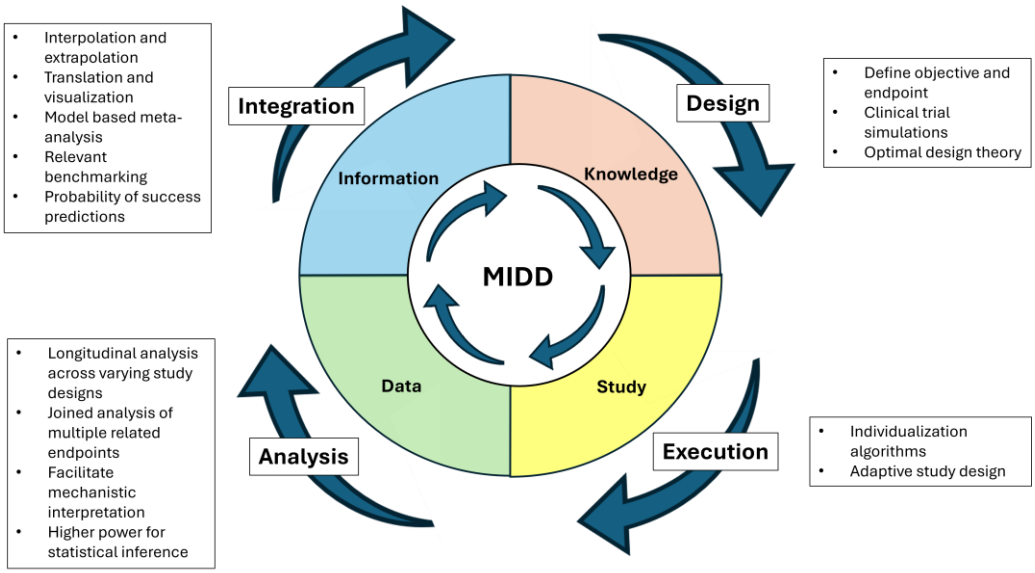

Figure 1.2 The learning and confirm paradigm in MIDD and its several applications.

Despite MIDD can be applied across all therapeutic areas, this section focuses on its application in oncology drug development. MIDD informs every stage of oncology drug development, from early to late clinical phases [53, 54].

- **Early Development Stages** MIDD helps understand the PK and safety profile of an investigational oncology drug in nonclinical species. This information is crucial for translating findings to first-in-human studies, where it can significantly inform the dosing strategy [55, 56].
- **Clinical Development** In clinical trials, PK/PD modeling characterizes the impact of intrinsic (e.g., genetic factors, organ function, demographics) and extrinsic (e.g., drug interactions, diet) covariates on drug exposure and efficacy [57]. For example, modeling can predict how a patient's liver function might alter the drug's exposure.
- **Combination Regimens** Oncology drugs are often administered in combination with novel compounds or standard-of-care treatments [58]. Choosing the optimal drug combination through conventional clinical trials can be challenging due to the high cost and difficulty in patient enrollment. MIDD addresses these challenges by simulating "what if" scenarios, helping to optimize the clinical trial process without the need for numerous costly trials [59].

- **Commercial and Regulatory Support** MIDD supports commercial decisions, such as go/no-go assessments for drug development, comparator effectiveness evaluations, and alternative pricing strategies [60]. Additionally, it aids in regulatory filings by providing robust data to demonstrate return on investment (ROI) to payers once the product is commercially available [61].

1.2.1. Model-based analysis of xenograft mice models

Several mathematical models have been proposed and widely applied to describe TGI studies in xenograft mice. These models facilitate the analysis of data collected during xenograft experiments. Most models use ordinary differential equations (ODEs) to describe changes in tumor burden [62].
The natural tumor growth in the absence of treatment is commonly characterized by different-shaped functions, which are summarized in Table 1.2. These functions help in understanding the baseline growth patterns of tumors, providing a reference for evaluating the effects of treatments.

Table 1.2 Modeling frameworks for characterizing natural tumor dynamics in xenograft mouse models.

Model	Equation	Parameters	Reference
Linear growth	$\frac{dT}{dt} = k_g$	k_g = linear growth rate	[63]
Exponential growth	$\frac{dT}{dt} = k_g \cdot T$	k_g = exponential growth rate	[64]
Logistic growth	$\frac{dT}{dt} = k_g \cdot T \cdot (1 - \frac{T}{T_{max}})$	k_g = growth rate, T_{max} = maximum tumor size	[65]
Gompertz growth	$\frac{dT}{dt} = k_g \cdot T \cdot ln(\frac{T}{T_{max}})$	k_g = growth rate, T_{max} = maximum tumor size	[66]
Simeoni growth (linear + exponential growth)	$\frac{dT}{dt} = \frac{\lambda_0 \cdot T}{\left[1 + \left(\frac{\lambda_0}{\lambda_1} \cdot T\right)^{20}\right]^{\frac{1}{20}}}$	λ_0 = exponential growth rate, λ_1 = linear growth rate	[67]

Notes: T = tumor weight.

Subsequently, tumor shrinkage resulting from drug treatment is typically quantified using an empirical drug-induced shrinkage term. Some of the most

used model structures describing the therapeutic effect are summarized in Table 1.3.

Table 1.3 Modeling frameworks for characterizing tumor growth inhibition.

Model	Equation	Parameters	Reference
First-order treatment effect ("log-kill" pattern)	$\frac{dT}{dt} = f(T) - k_d \cdot T$	k_d = first-order shrinkage rate	[63]
Exposure-dependent treatment effect	$\frac{dT}{dt} = f(T) - k_d \cdot Exposure \cdot T$	k_d = first-order shrinkage rate	[68]
Exposure-dependent treatment effect with resistance	$\frac{dT}{dt} = f(T) - k_d \cdot e^{-\lambda t} \cdot Exposure \cdot T$	k_d = first-order shrinkage rate, λ = rate of decrease in treatment effectiveness	[69]
Introducing a damaged cell compartment	$\begin{cases} \frac{dS}{dt} = f(S) - k_d \cdot Exposure \cdot S \\ \frac{dD}{dt} = k_d \cdot Exposure \cdot S - d \cdot D \\ T = S + D \end{cases}$	k_d = first-order death rate, d = first-order shrinkage rate of damaged cells	[70]
Nonlinear drug exposure–effect relationship	$k_g' = k_g \cdot (1 - \frac{E_{max} \cdot Exposure}{IC_{50} + Exposure})$	E_{max} = maximum growth rate inhibition, IC_{50} = exposure for which growth is inhibited by 50%	[71]

Notes: T = tumor weight, S = weight of proliferating tumor cells, D = weight of damaged tumor cells, Exposure: measure of drug exposure to treatment

1.2.2. Model-based analysis of oncology trial endpoints

OS and PFS data are classified as time-to-event (TTE) data. TTE data consist of two tightly linked components: the time variable and the event indicator. The first component, the time variable, is the interval from the starting time to the event time or the last follow-up time whichever occurs first. The event indicator is a categorical variable indicating the patient's status at the ending time which meaning could vary depending on the time of TTE model. For OS, the event indicator variable is often coded as 1 (= dead) for patients who die during the follow-up period and 0 (= censored) for patients who are alive at the last follow-up. For PFS, the event indicator is one (= dead or

progressive disease) if the patient has a cancer progression or dies; and zero (= censored) if the patient is alive without cancer progression at the last follow-up.

TTE data are commonly summarized using Kaplan-Meier (KM) curves, a non-parametric approach that estimates survival probabilities over time by incorporating data from both patients who have experienced the event of interest and those who are censored. Statistical summaries derived from KM estimates include the median survival time (the time point in which the survival probability is 50%) and survival probabilities at fixed time points throughout the study.

The goal of many clinical studies is to compare survival between treatment groups or to evaluate the association between patient demographics or disease-related risk factors and survival. The most widely used survival analysis techniques are the log-rank test and the Cox proportional hazards model.
The log-rank test compares the hazard rates (the rates at which the event of interest occurs among those still at risk for that event) between groups. However, the log-rank test is strictly a testing procedure that produces a *p*-value but does not provide an estimate of the treatment effect. The log-rank test compares the entire survival curves rather than the Kaplan-Meier estimates at a specific time point.
When an estimate of the treatment effect on survival is needed or when the comparison needs to adjust for other covariates or confounding factors, Cox models are fit to provide hazard ratio estimates and corresponding confidence intervals. Cox models are often used to identify potential biomarkers associated with survival outcomes. One important assumption of the Cox model is that the hazard ratio is constant over time, known as the proportional hazards (PHs) assumption. If there are indications of non-PHs, models with time-varying effects should be considered.

In oncology trials, in addition to TTE models, TGI models are also fundamental mathematical tools. Tumor dynamics form the basis for calculating RECIST criteria, which define tumor-based endpoints such as PFS. Additionally, model-based estimates of early TGI metrics or predicted time courses of tumor dynamics have been shown to predict OS in later development stages [60, 72]. The complexity of tumor dynamic models depends on the available data, more data allows for more detailed or mechanistic models, and the model's purpose. Examples of commonly used models, also applied in preclinical research, are already listed in Table 1.3.

1.2.3. Translational oncology

Translational oncology is an interdisciplinary field that bridges the gap between laboratory research and clinical practice [73]. This discipline encompasses various aspects, from well-established practices in drug development, such as defining the first dose in humans, to more experimental areas like correlating circulating cell-free DNA and mitochondrial DNA between animals and humans. As the focus of this thesis, this section will concentrate exclusively on the translational aspects of efficacy in relation to tumor dynamics [25].

In this field, the seminal works of Wong [74], Rocchetti [75], Inaba [76, 77], and their coworkers have demonstrated the potential to predict the clinical efficacy, at least in ranking, of multiple compounds by considering PK differences between species as well as drug potency. Furthermore, through an analysis of the National Cancer Institute nonclinical and clinical databases [78] it has been shown that achieving unbound drug exposure and biomarker modulation in patients similar to those observed in preclinical studies is necessary (but not sufficient) for observing efficacy in the clinic [79].

More recent work led by Garcia-Carmades [80] aims to predict clinical response in patients using preclinical data obtained from mice carrying xenograft tumors. The proposed methodology combines preclinical PK/PD model, clinical PK models and dosing schemes, along with allometry-based mouse-human conversion to describe tumor response and survival data of gemcitabine-treated patients. In this work, assuming that the drug-specific PD parameters are likely to be similar across species, the effect parameters were not transformed from those estimated in mice. Baaz et al [81] instead used PDX models to calibrate the preclinical TGI model using xenograft data from the literature on published RECIST clinical data for three drug combinations. After replacing the preclinical PK model with the clinical model, based on the RECIST response, translational factors are estimated highlighting a possible drug/cancer type-specific scaling.

Translational Applications in Different Oncology Trial Phases:

Phase I: Translational tumor dynamics modeling can support the planning of dose range and dosing frequency. By identifying the target efficacious concentration through xenograft studies, this information can be coupled with predicted or observed human PK to project the efficacious dose range in humans that maximizes tumor shrinkage. Additionally, this approach could help in choosing the appropriate pharmacodynamic sampling schedule.

The PD response characterized preclinically may inform PD sample collection time points in clinical studies.

Phase II/III: Challenges in Phase II/III trials often include combining an experimental treatment with the current standard of care and/or another experimental treatment to increase the pool of responding patients. With many innovative combinations available, nonclinical trials and translational modeling play a crucial role in guiding clinical development and Phase II/III combination trials by prioritizing the choice of combination partner, i.e. selecting the most promising combination partners based on preclinical efficacy or assessing administration strategies, i.e. determining whether concomitant administration or a specific sequence is more promising or worth exploring [82–84]. Furthermore, another potential application is in supporting the development of clinical tumor growth inhibition models [74, 85]. TGI parameters have been shown to be important for Phase II/III patient death risk stratification; consequently, precise estimation of these parameters is needed. Translational modeling can inform TGI parameter estimation, thereby reducing issues related to "flip-flop" phenomena or overcoming non-identifiability problems. By refining these models, researchers can improve the prediction accuracy of treatment outcomes, enhancing the reliability of clinical trials.

Mechanistic Clinical Longitudinal Models:

Another application that spans throughout the entire development process involves developing more mechanistic clinical longitudinal models. Longitudinal tumor size models end to be agnostic of the mechanism of action (MoA) [62, 70]. A careful review of the dynamic features of nonclinical data, accompanied by MoA-based hypothesis generation and model-based hypothesis validation, can help identify mechanistic model features in nonclinical data. These features may be challenging to establish in clinical data due to small subject numbers and limitations of clinical practice [86].

1.2.4. Challenges in translational oncology

The challenges of translational oncology include several critical factors that must be addressed to optimize translation into the clinical setting. For example, poor reproducibility of preclinical research in different laboratories may compromise the reliability of translational predictions [87]. Second, broader validation of translational approaches across various tumor types and drugs is needed to support the validity of proposed approaches. In

addition, there are differences in measurement techniques between clinical and preclinical settings that pose a significant challenge; while xenograft studies typically use endpoints such as percentage of tumor growth inhibition and growth retardation, clinical evaluations often lack comparable placebo-controlled or untreated comparisons. To mitigate these challenges, it is critical to improve the heterogeneity of nonclinical data sets, reduce operational bias, and establish standardized and translatable efficacy endpoints. Addressing these issues through improved methodologies and practices is essential to increase the reliability of translational predictions and advance more effective cancer treatments [25].

1.3. Thesis overview

This thesis aims to leverage the potential of PDX mouse models and MIDD approaches to develop and implement a translational preclinical-to-clinical framework. The work is organized around two main objectives

Chapter 2 and 3: Development of the Translational Framework

- **Chapter 2** This chapter presents the initial steps of the multistep framework, focusing on the translation of the natural tumor growth in the absence of treatment. It demonstrates how to effectively map natural tumor growth patterns from preclinical settings to clinical contexts. This step serves as a foundation for more complex analyses and interventions in later stages of the framework.

- **Chapter 3** This chapter extends the translational by incorporating the effects of therapeutic interventions, specifically focusing on the impact of drug treatments on tumor growth inhibition (TGI). It builds upon earlier models of natural tumor growth and develops a comprehensive approach that integrates drug-induced changes in tumor dynamics.

Chapter 4 and 5: Applications of the Translational Framework

- **Chapter 4** This chapter introduces a *dynamic borrowing* approach to integrate virtual patients (generate through the developed framework) with real patients to build hybrid control arms in clinical trials. These methods offer a mathematically rigorous and robust approach to increase efficiency and strengthen evidence by integrating external data into a new clinical trial without relying on historical patients.

- **Chapter 5** In this chapter information from preclinical contexts, via the developed translational framework, is translated into the clinical setting to inform Bayesian estimation of joint longitudinal-OS nonlinear mixed-effects models.

Chapter 2

Predicting tumor volume doubling time and Progression-Free Survival in untreated patients from PDX mice experiments*

The first step of this work involved the development of a translational framework to scale natural tumor growth from PDX mouse models to untreated cancer patients. This approach was applied to predict PFS and tumor volume doubling times (TVDTs) and validated on clinically available data. PFS, as previously introduced in Section 1.6, is an important primary endpoint in cancer clinical trials. TVDT represents a useful tool for the clinical management of cancer with important implications for a multitude of medical decisions. For example, it could allow to determine the optimal follow-up times for screening patients [88], to assess the impact of delaying diagnosis and/or treatment, to accurately estimate the period of risk and the time of metastasis, to correctly select between pharmaceutical or surgical options, and to optimize treatment protocols [88–90]. TVDT was also shown to be strongly correlated with tumor response to therapy and, therefore, to tumor progression and patient survival [91, 92].

** The content of this chapter was published as Tosca, E.M., Ronchi, D., Rocchetti, M. et al. Predicting Tumor Volume Doubling Time and Progression-Free Survival in Untreated Patients from Patient-Derived-Xenograft (PDX) Models: A Translational Model-Based Approach. AAPS J 26, 92 (2024). https://doi.org/10.1208/s12248-024-00960-4*

This chapter is structured as follows: Section 2.1 introduces the general framework for translating natural tumor growth from PDX mouse models to cancer patients.
Section 2.2 presents case studies, and the associated data used to develop and validate the framework. Subsequently, Section 2.3 focuses on the developed tumor growth model in PDX mice, while Section 2.4 discusses the scaling process and compares predicted TVDT and PFS values with those observed in existing literature. Finally, Section 2.5 summarizes and discusses the results, providing rationale for advancing to the next phase of the study.

2.1. Translational framework for the natural (untreated) tumor growth

A multistep procedure is devised to predict TVDTs and PFS curves in untreated cancer patients using tumor growth data from PDX mouse studies (Figure 2.1).

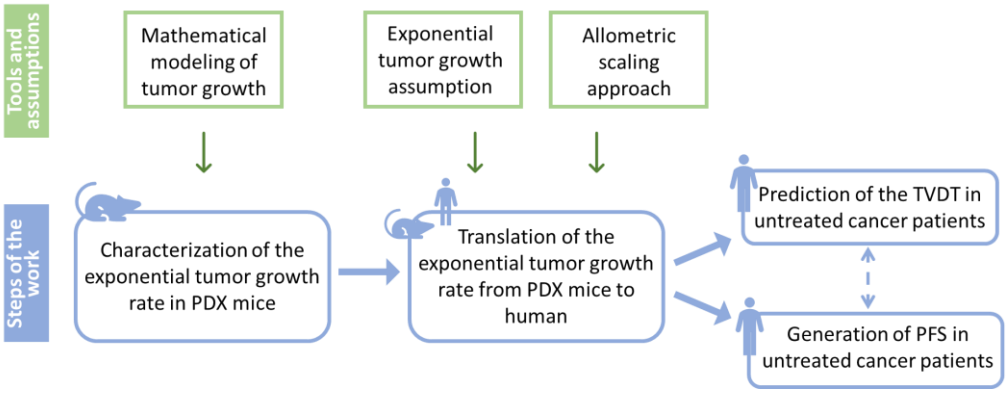

Figure 2.1 Flow chart representing the translational modeling approach developed to predict TVDTs and PFS in untreated cancer patients from tumor growth data in PDX mice.

The first step of the framework involves the development of a population model that describes natural tumor growth in PDX mice, in order to characterize the distribution of the exponential tumor growth rates in these models. Subsequently, an allometric scaling approach is employed to extrapolate tumor growth rates from PDX mice to humans, assuming exponential growth of untreated tumor mass in humans. Finally, these scaled tumor growth rates are used to predict TVDTs and PFS curves in patients.

2.1.1. Mathematical modeling of natural tumor growth in PDX mice

An unperturbed growth model describing the time-course of average tumor mass weight is used to characterize the distribution of exponential tumor growth rate, k_g. A population approach is adopted to simultaneously analyze multiple PDX studies. Individual model parameters follow a log-normal distribution, with model fitting performed accordingly. The log-normal distribution of the exponential growth rate is estimated using parameterization $k_{g,i} = k_{g,pop} \cdot e^{\eta_i}$ where $k_{g,pop}$ represents the typical population parameter (median) for a specific cancer type, and η is a normally distributed variable with mean zero and standard deviation ω_{k_g}, accounting for inter-PDX model variability. $k_{g,i}$ represents the exponential tumor growth rate of the i^{th} - PDX model.

Importantly, k_g, the exponential growth rate, is not specific to any particular model. For translation to humans, the focus is on accurately characterizing the tumor growth rate in PDX model, regardless of the mathematical model used to describe tumor dynamics.

2.1.2. Scaling the exponential tumor growth rate from PDX mice to human

Based on clinical evidence, human cancers are assumed to grow exponentially with a rate $k_{g,human}$, at least during the clinically observable period. The exponential tumor growth rates observed in PDX mice are scaled up to humans using an allometric scaling approach:

$$k_{g,human}\left[\frac{1}{months}\right] = 30 \cdot k_g[\frac{1}{days}] \cdot \left(\frac{BW_{human}}{BW_{mice}}\right)^{-\alpha} \quad (1)$$

where BW_{human} and BW_{mice} represent the typical body weight of human (70Kg) and mice (0.025Kg), respectively, 30 was the unit conversion factor from day to month and α the allometric exponent that was fixed to 1/3 embracing the 2/3-power scaling rule [93].

A lognormal distribution of $k_{g,human}$ is predicted propagating the k_g variability ω_{k_g}. Distribution of $k_{g,human}$ is parameterized as $k_{g,human,i} = k_{g,human,pop} \cdot e^{\eta_{human,i}}$ where $k_{g,human,pop}$ is the typical value (median) and

$\eta_{k_{g,human}}$ a normally distributed variable with mean zero and standard deviation $\omega_{k_{g,human}} = \omega_{k_g}$.

2.1.3. Predicting TVDT distributions in untreated cancer patients

TVDTs in untreated cancer patients are directly computed from $k_{g,human}$ through the following formula:

$$TVDT_{human} = \frac{\ln(2)}{k_{g,human}}. \quad (2)$$

Therefore, $TVDT_{human}$ resulted lognormally distributed. $TVDT_{human,i} = TVDT_{human,pop} \cdot e^{\eta_{TVDT,human,i}}$ where $TVDT_{human,pop} = \frac{\ln(2)}{k_{g,human,pop}}$ is the typical (median) value and $\eta_{TVDT,human} = -\eta_{k_{g,human}}$ a normally distributed variable.

2.1.4. Simulating PFS curves in untreated patients

PFS predictions in untreated cancer patients are obtained following a strategy based on the work of Kay et al. [94].

First, PD events due to target lesion progression are considered. Simplifying the RECIST [95], they are defined as a 20% increase of the SLDs of target tumor lesions. Second, tumors are supposed to be composed by a single lesion with a spherical shape (i.e., same growth dynamics along the three spatial dimensions), that can be considered representative of the overall tumor burden due to target lesions. Under these assumptions, the tumor volume change associated to a 20% increase in diameter was found to be 1.728-fold (for more details on the conversion see Supplementary Material *Calculation of time of progression*). Finally, since tumor volume grows exponentially with a rate $k_{g,Human}$, the time of tumor progression, t_{event}, is computed as:

$$t_{event} = \frac{ln(1.728)}{k_{g,human}} \quad (3)$$

For each cancer type, 200 values are sampled from the log-normal distribution of $k_{g,human}$, the corresponding times of progression are computed through Eq.4 and used to construct the KM curve for PFS. This process is repeated 1000 times propagating uncertainty of parameter estimates, i.e., 1000 studies each composed by 200 patients are simulated. The 1000 simulated KM curves were used to construct the KM-visual predict check (VPC) plots, where simulations are overlaid with the published PFS plots (when available).
The predicted and observed median PFS (i.e., time at which the PFS curve crosses the 50% point) are also compared.

2.2. Case studies and data availability

2.2.1. Case studies

Eleven different solid cancers classified by primary site and/or histological type are considered: breast cancer (BR), cholangiocarcinoma (CC), colorectal cancer (CR), head and neck cancer (HN), gastric cancer (GA), liver cancer (LI), melanoma (ME), pancreatic cancer (PA), sarcoma (SA) and two subtypes of non-small-cell lung cancer (LU), i.e., adenocarcinoma (ADC) and squamous cell carcinoma (SCC). They are selected based on the concomitant availability of tumor growth studies in PDX mouse models and adequate characterization of TVDT in untreated cancer patients.

2.2.2. In vivo tumor growth studies in PDX mice

Specifically, a panel of 265 PDX mouse models (25 for each cancer type except for CC (n=24) and SA (n=16)), originally derived from cancers of 265 patients, is considered. For each PDX mouse model, a single study, involving several mice, is selected and data obtained from HuBase database (Crownbio Bioscience Inc., https://www.crownbio.com/). All the in vivo experiments were performed at Crownbio as follows: tumor fragments were inoculated subcutaneously in several immunodeficient mice and tumor dimensions were measured by caliper. Tumor volume was derived as $(length \cdot width^2)/2$ and converted to weight assuming unit density. For each study, average tumor weight is made available.
The complete list of the analyzed experiments is reported in Table A1 of Appendix A.

2.2.3. Collection and curation of TVDTs and PFS data in cancer patients

To ensure robust validation of tumor growth predictions and therapeutic response modeling, it is important to collect accurate clinical data on clinical TVDT and PFS across different cancer types.

For each cancer type, studies measuring the TVDT value of primary tumors in untreated cancer patients were retrieved from the literature. Studies were selected if they reported the median, minimum, and maximum TVDT values, as well as the population size, or alternatively individual TVDT values. In total, twenty-six studies were included. Table A2 of Appendix A lists the reported median, minimum, and maximum TVDT values and the population size for each study.

Clinical data indicated that the frequency distribution of TVDT obtained is positively skewed, with some very long TVDTs compared to the typical value. To mitigate the impact of these outliers, a range of TVDT variation is estimated for each study based on the strategy detailed in the *TVDT data in untreated cancer patients* section in Appendix A.

In addition, for each cancer type, literature was searched to retrieve appropriate PFS data to validate PFS predictions. Because placebo arms are rarely available in clinical trials, published PFS data from different clinical trials including patient cohorts receiving placebo, supportive care or active treatments exerting little to no effect on tumor growth (i.e., overall response rate, ORR, ≤10%) were selected For BR cancer, ADC and SCC of lung, works reporting suitable PFS data were not found. The selected references (n=25) are listed in Table A3 in Appendix A together with details about the clinical studies. KM plots from these studies were digitalized, their 95% CIs were reconstructed and the median PFS values, i.e., time at which the PFS curve passes cross the 50% point, extracted.

2.3. Tumor growth model in PDX mice

For each cancer type, the Simeoni growth model is used to model PDX studies [67]. It assumes that the unperturbed tumor growth can be described by an exponential growth phase, characterized by the rate λ_0 [1/day], followed by a linear one (with slope λ_1 [cm3/day]).

Model fitting is performed assuming a proportional residual error, i.e., $y = \boldsymbol{f} + b \cdot \boldsymbol{f} \cdot \boldsymbol{\varepsilon}$, where $\boldsymbol{y}$ is the measurement, b a coefficient representing the

coefficient of variation, $\boldsymbol{f}$ the model prediction and $\boldsymbol{\varepsilon}$ a standardized random variable normally distributed. Details about model fitting and diagnostic plots are provided in the section Tumor growth model in *Model fitting of tumor growth studies in PDX mice* in Appendix A.
The model parameter estimates together with their estimation uncertainty are reported in table format in Table 2.1 and in density plot format in Figure A2 in Appendix A. Individual PDX estimates are also reported in Table A4 in Appendix A.

Table 2.1 Parameter estimates of the population Simeoni tumor growth models in PDX mice together with estimation uncertainty (CV%).

Cancer Type	λ_0 [1/day] - Rate of exponential growth		λ_1 [cm^3/day]- Rate of linear growth		W_0 [g]- Initial tumor weight		b [-] – Coefficient of RUV model
	$\lambda_{0,pop}$	$\omega_{\lambda 0}$	$\lambda_{1,pop}$	$\omega_{\lambda 1}$	$W_{0,pop}$	ω_{w0}	
BR	0.066 (10%)	0.50 (15%)	0.053 (17%)	0.67 (18%)	0.013 (21%)	1.02 (14%)	0.066 (5%)
CC	0.142 (9%)	0.37 (17%)	0.040 (18%)	0.84 (16%)	0.003 (25%)	0.46 (24%)	0.117 (7%)
CR	0.057 (8%)	0.39 (16%)	0.030 (14%)	0.59 (18%)	0.027 (14%)	0.64 (14%)	0.072 (5%)
GA	0.053 (10%)	0.5 (14%)	0.026 (20%)	0.79 (18%)	0.024 (14%)	0.69 (15%)	0.072 (5%)
HN	0.088 (10%)	0.5 (15%)	0.065 (8%)	0.23 (25%)	0.018 (16%)	0.76 (15%)	0.083 (7%)
LI	0.110 (12%)	0.58 (15%)	0.069 (18%)	0.75 (20%)	0.009 (24%)	1.03 (18%)	0.088 (6%)
LU ADC	0.064 (11%)	0.55 (14%)	0.037 (12%)	0.46 (19%)	0.017 (14%)	0.65 (14%)	0.061 (5%)
LU SCC	0.100 (11%)	0.55 (15%)	0.046 (13%)	0.63 (15%)	0.012 (17%)	0.81 (15%)	0.063 (5%)
ME	0.096 (10%)	0.51 (15%)	0.064 (13%)	0.42 (30%)	0.014 (16%)	0.68 (19%)	0.064 (8%)
PA	0.081 (11%)	0.54 (15%)	0.050 (15%)	0.67 (16%)	0.016 (12%)	0.54 (13%)	0.093 (5%)
SA	0.200 (8%)	0.27 (21%)	0.15 (21%)	0.70 (23%)	0.006 (20%)	0.48 (24%)	0.117 (10%)

Therefore, the lognormal distribution of the exponential tumor growth rate λ_0 and the individual $\lambda_{0,i}$ values are successfully derived.

It is crucial to note that in this framework, k_g, the exponential growth rate, corresponds directly to the parameter λ_0 of the Simeoni model. This connection is essential for the subsequent translation of tumor growth rates from mice to humans.

2.4. Prediction of clinical endpoints in untreated cancer patients

The exponential growth rate values obtained from the Simeoni model (parameter λ_0) are scaled up from mice to humans through Eq. 1. For each cancer type, a lognormal distribution of $k_{g,human}$ is obtained. The estimation uncertainty affecting mice-related parameters is propagated to the parameters of the $k_{g,human}$ distributions, which are reported in Table A5 in Appendix A. Density plots are displayed in Fig A3. Additionally, individual $k_{\mathrm{g},human,i}$ values are computed and are reported in Table A5 as well.

2.4.1. TVDTs

For each cancer type, the lognormal distribution of TVDT in untreated cancer patients is derived from $k_{\mathrm{g},human}$ using Eq. 2, with propagation of estimation uncertainty. The 80% prediction intervals (PI) for the predicted TVDTs in humans is calculated and reported in Table 2.2, alongside typical values and observed ranges from the literature. These calculations followed the methodology described in the *Predicting TVDTs and PFS in untreated cancer patients* section of Appendix A.

Table 2.2 Observed and predicted TVDT [month] in untreated cancer patients.

Cancer Type	Predicted TVDT [month], median and range* by cancer type	Observed TVDT [month], median and range** by literature studies		Observed TVDT [month], median and range** by cancer type
		Reference	TVDT	
BR	4.93 [2.01, 12.38]	Fournier [96]	7.97 [2.4, 26.7]	5. 66 [1.92, 16.55]
		Gershon-Cohen [97]	4 [1.98, 8.12]	
		Ryu [98]	4.7 [1.87, 11.85]	
		Tabbane [99]	3.83 [1.06, 13.76]	
		Zhang [100]	5.47 [2.81, 10.66]	
CC	2.33 [1.17, 4.87]	De Rose [101]	2.33 [0.75, 7.32]	-
CR	5.71 [2.80, 11.98]	Bolin [102]	4.33 [1.46, 12.93]	6.12 [2.87, 13.02]
		Burke [103]	7.03 [4.66, 10.59]	
		Tada [104]	8.11 [3.75, 17.44]	
GA	6.14 [2.53, 15.57]	Haruma [105]	8.1 [3.8, 17.22]	8.57 [3.33, 22.16]
		Seung-Young [106]	8.63 [3.27, 22.97]	
HN	3.69 [1.53, 9.06]	Jensen [107]	3.3 [1.36, 7.96]	2.99 [1.26, 7.18]
		Waaijer [108]	1.9 [0.85, 4.25]	
LI	2.93 [1.03, 8.56]	Barbara [109]	5.72 [2.12, 15.28]	3.22 [1.35, 7.7]
		Kubota [110]	2.77 [1.16, 6.63]	
		Park [111]	2.03 [0.98, 4.22]	
		Sheu [112]	3.9 [1.69, 8.96]	
		Nakajima [113]	2.48 [1.03, 6.02]	
LU ADC	5.09 [1.88, 14.19]	Honda [114]	8.53 [2.61, 27.63]	5.52 [1.77, 17.3]
		Kanashiki [115]	4.47 [1.47, 13.67]	
		Mackintosh [116]	8.3 [2.53, 27.44]	

Cancer Type	Predicted TVDT [month], median and range* by cancer type	Observed TVDT [month], median and range** by literature studies		Observed TVDT [month], median and range** by cancer type
		Reference	TVDT	
LU SCC	3.26 [1.21, 9.04]	Honda [114]	4.37 [2.51, 7.55]	3.46 [1.5, 7.95]
		Kanashiki [115]	3.3 [1.31, 8.27]	
		Mackintosh [116]	3.23 [2.08, 4.98]	
ME	3.39 [1.34, 8.88]	Carlson [117]	3.13 [1.69, 5.78]	-
PA	4.02 [1.52, 10.85]	Furukawa [118]	4.8 [3.07, 7.53]	3.74 [2.36, 5.94]
		Rezai [119]	2.99 [1.87, 4.83]	
SA	1.63 [0.93, 2.86]	Galante [120]	0.24 [0.06, 0.99]	0.27 [0.07, 1.06]
		Spratt [121]	0.83 [0.42, 1.63]	

** Range = 80%PI (see section 2.2.3.1) ** Range = 80%CI*

Predicted TVDT median values are very close to the typical values observed in clinics, with 91% of the predictions within 1.5-fold of the observations and a root mean squared error (RMSE) of 0.9244 months (Figure 2.2).

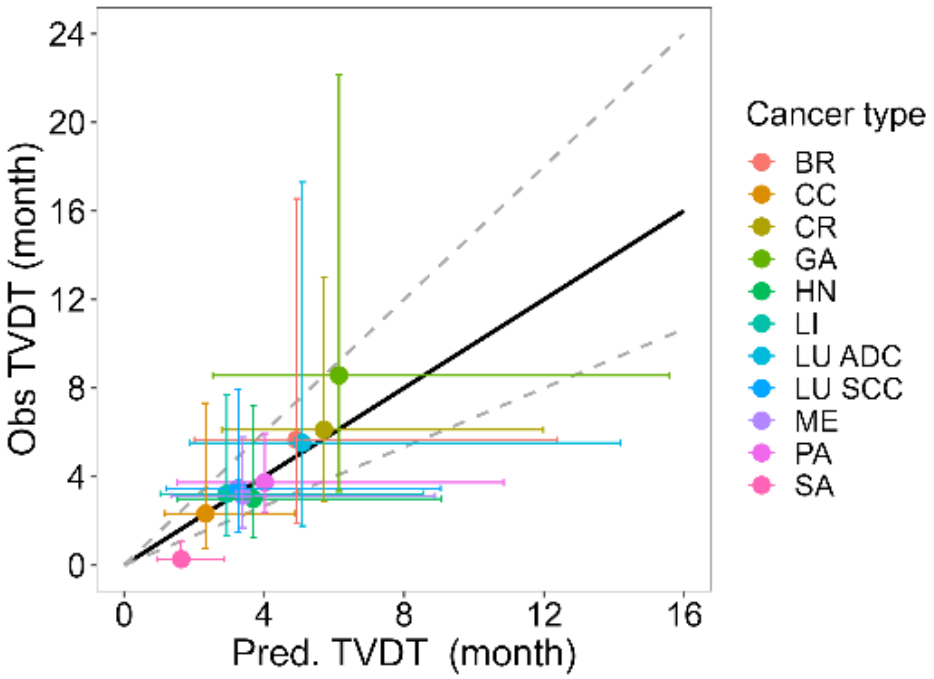

Figure 2.2 Predicted versus observed TVDTs stratified by cancer type. Dots mark the typical values, vertical and horizontal bars the 80%-intervals of the

observed and predicted TVDTs, respectively. Identity line and 1.5-fold areas are represented by solid and dashed black line, respectively. The 80%-intervals represent the 80%CIs for observed TVDTs and 80%PI for the predicted TVDTs.

Considering the individual TVDTs, directly derived from the 265 analyzed PDX mouse models (Table A6 in Appendix A), 83.59% of the predictions falls within the reported clinical 80%CI ranges. Among the considered cancer types, sarcoma is the worst predicted case study, with predicted TVDTs generally higher than the observed (Figure 2.3).

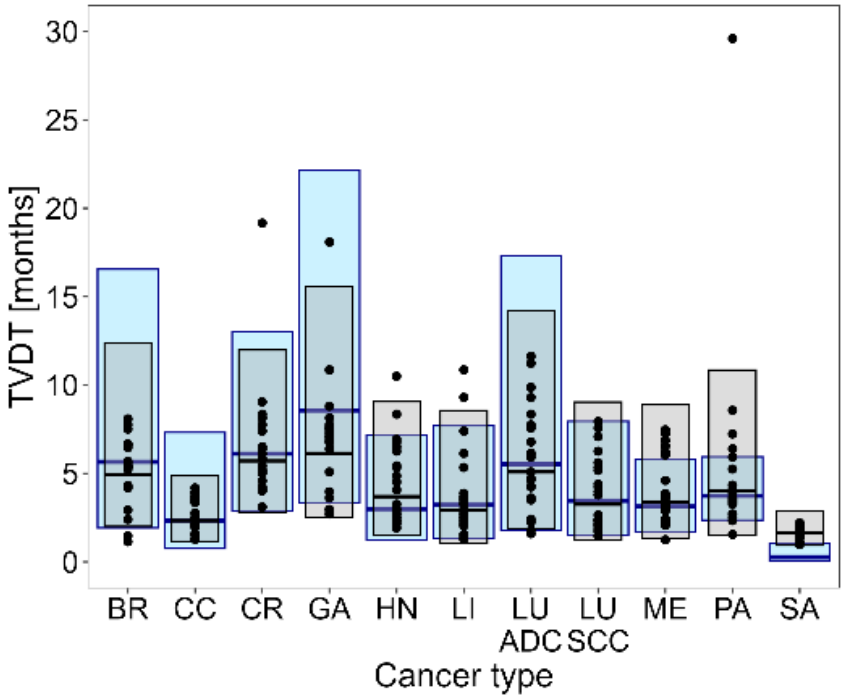

Figure 2.3 Box plots (medians and 80%-intervals) of the observed (lightblue) and predicted (grey) TVDTs in untreated cancer patients stratified by cancer type. Dots mark the individual TVDTs predicted from the 265 analysed PDX mouse models. The 80%-intervals represent the 80%CIs for observed TVDTs and 80%PI for the predicted TVDTs.

For what regard the TVDT inter-patient variability, values vary significantly among studies reported in the literature, even if they are related to the same cancer type (Figure 2.4).

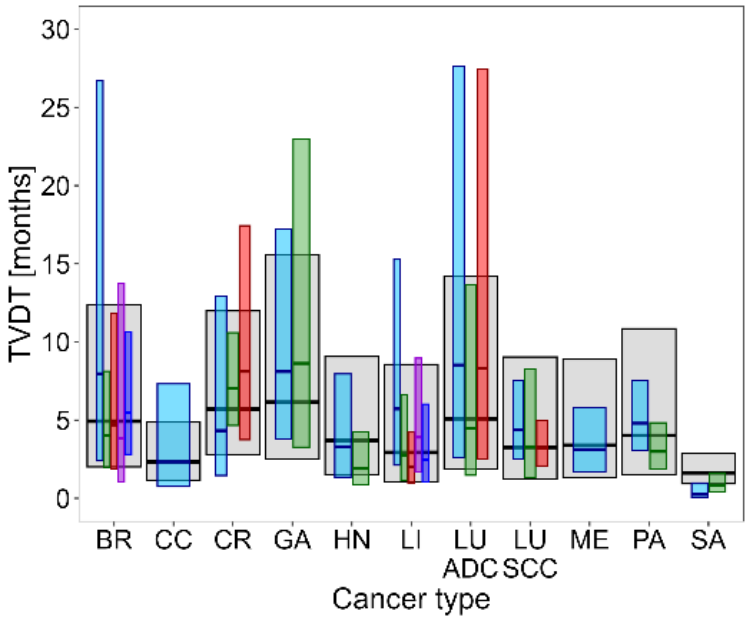

Figure 2.4 Box plots (medians and 80%-intervals) of the observed (colored) and predicted (grey) TVDTs in untreated cancer patients stratified by cancer type and literature study. The 80%-intervals represent the 80%CIs for observed TVDTs and 80%PI for the predicted TVDTs.

The 80%PIs of predicted TVDTs are quite consistent with the 80%CIs of the clinical TVDTs for almost all the cancer types, however, the comparison of the observed and predicted standard deviation of TVDTs (i.e., ν_{TVDT} vs ω_{TVDT} in Table A2 and A6) reveals an underestimation of the clinically observed inter-patient variability for some cancer types.

2.4.2. PFS

PFS curves are generated from the distributions of the scaled exponential growth rates, $k_{g,human}$, accounting for the uncertainty of parameter estimates. Fig. 2.5 shows the KM-VPC plots generated from 1000 simulated clinical studies (each composed by 200 individuals) superimposed over the observed PFS curves for cancer types. Simulated KM curves are overlaid to the literature PFS curves throughout the time course, demonstrating that the translational modeling approach can adequately predict PFS in untreated cancer patients.

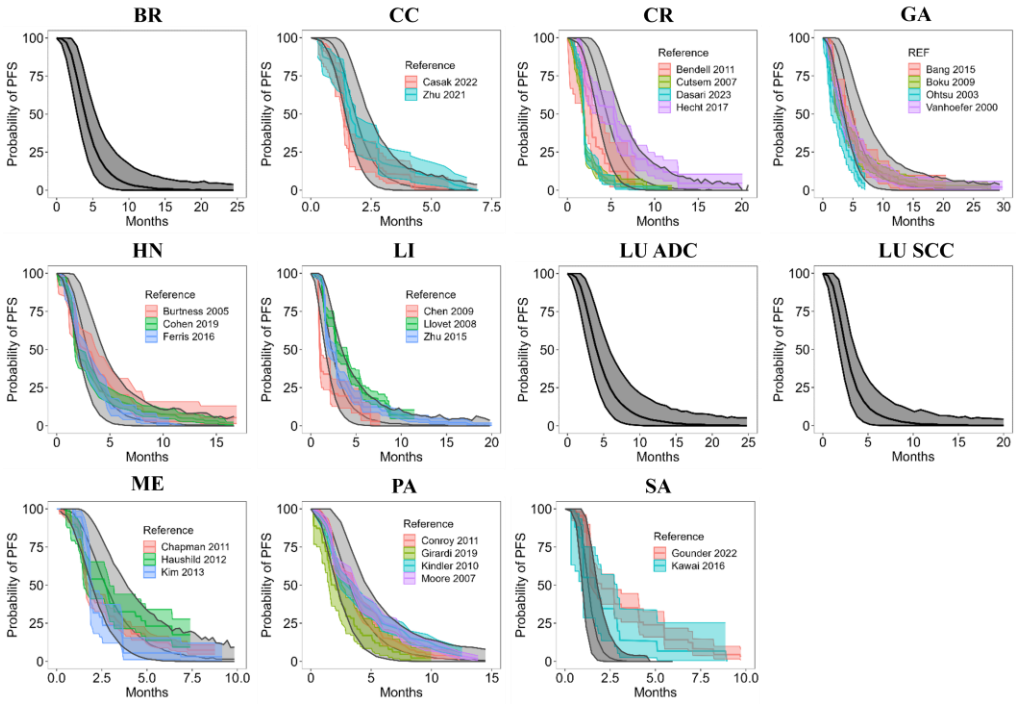

Figure 2.5 KM-VPC plots (grey areas) generated from 1000 simulated clinical studies composed of 200 individuals each superimposed to PFS curves taken from literature studies (colored areas), stratified by cancer types. Median and 95% CI are reported.

The predicted and observed median PFS (i.e., time at which the PFS curve passes cross the 50% point) together with its 95%PIs are reported in Table 2.3 in comparison with observations and plotted in Figure 2.6.

Table 2.3 Observed and predicted median PFS [month] in untreated cancer patients.

Cancer type	Reference	Observed median PFS [month] with 95% CI	Predicted median PFS [month] with 95% PI
BR	-	-	4 [3., 5.6]
CC	Casak [122]	1.4 [1.34, 1.85]	1.9 [1.5, 2.6]
	Zhu [123]	1.63 [1.46, 1.86]	
CRC	Bendell [124]	2.53 [1.65, 3.26]	4.6 [3.7, 5.9]
	Van Cutsem [125]	1.82, [1.77, 2.02]	
	Dasari [126]	1.8 [1.8, 1.93]	

Cancer type	Reference	Observed median PFS [month] with 95% CI	Predicted median PFS [month] with 95% PI
	Hecht [127]	5.4 [3.4, 5.66]	
GA	Bang [128]	3.55 [2.35, 5.12]	4.9 [3.7, 6.8]
	Boku [129]	2.9 [1.7, 5.7]	
	Ohtsu [130]	2.4 [1.3, 3.2]	
	Vanhoefer [131]	3.3 [2.9, 4.43]	
HN	Burtness [132]	2.7 [1.9, 4.01]	3 [2.3, 4.2]
	Cohen [133]	2.31 [1.79, 2.8]	
	Ferris [134]	2.3 [1.9, 3.14]	
LI	Cheng [135]	1.4 [1, 1.55]	2.4 [1.7, 3.6]
	Llovet [136]	2.8 [2.7, 4.11]	
	Zhu [137]	2.1 [1.6, 2.83]	
LU ADC	-	-	4.1 [3., 6.1]
LU SCC	-	-	2.7 [2., 3.8]
ME	Chapman [138]	1.6 [1.55, 1.77]	2.8 [2.1, 3.9]
	Hauschild [139]	2.7 [1.51, 2.95]	
	Kim [140]	1.8 [1.78, 2.04]	
PA	Conroy [141]	3.3 [2.2, 3.83]	3.3 [2.4, 4.7]
	Girardi [142]	1.7 [0.98, 2.57]	
	Kindler [143]	2.9 [2.4, 4.52]	
	Moore [144]	3.6 [3.29, 4.11]	

Cancer type	Reference	Observed median PFS [month] with 95% CI	Predicted median PFS [month] with 95% PI
SA	Gounder [145]	2.10 [1.51, 3.06]	1.4 [1.1, 1.7]
	Kawai [146]	1.75 [0.93, 2.91]	

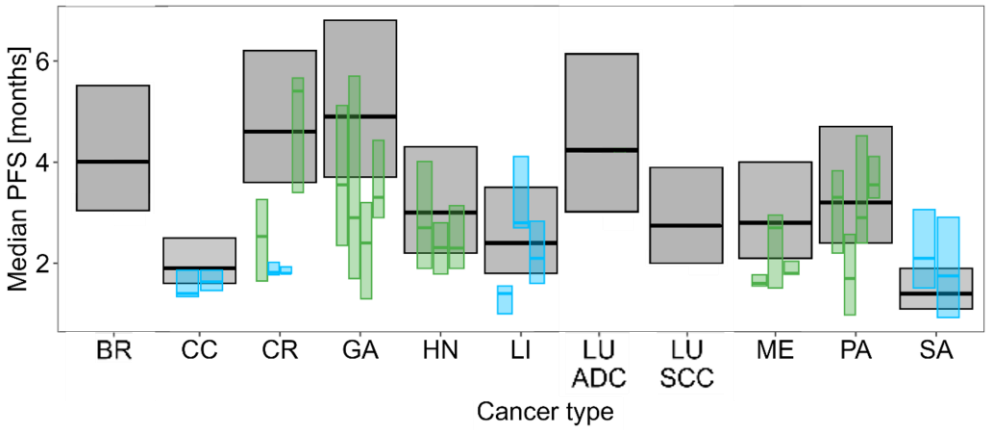

Figure 2.6 Box plot of the observed (colored) and predicted (grey) median PFS in untreated cancer patients stratified by cancer type and references. For observations, patient cohorts receiving placebo or active treatments were marked in blue and green, respectively. Medians and 95%PI are reported.

Predictions and observations are in close agreement with 95%-ranges overlapping in most of the cases.

2.5. Wrap up and future developments

A translational modeling approach to predict TVDT distributions and PFS curves in population of untreated cancer patients from tumor growth data in PDX mice was developed and successfully applied on eleven types of solid cancers. It is a multistep procedure that essentially relied on the assumption of an exponential growth of human solid tumors.

First, for each cancer type, a set of tumor growth studies in PDX mice was analyzed through a mathematical modeling approach, allowing to derive the exponential tumor growth rate characterizing the initial tumor growth phase in mice. To this aim, the Simeoni growth model [67] was applied and combined with a population approach. A lognormal distribution for the exponential tumor growth rate was identified for each cancer type, accounting for the variability between different PDX mouse models (called

inter-PDX variability). Then, the exponential growth rates were scaled up from mice to humans. According to the allometric scaling rules, the values of the exponential growth rate in mice, $k_{g,mice} = \lambda_0$, were adjusted based on body weight. The inter-PDX variability was propagated, and a lognormal distribution was derived for the exponential tumor growth rates in humans, $k_{g,human}$, for each cancer types. The obtained $k_{g,human}$ (individual values and distributions) were used to predict the TVDT distributions and PFS in untreated cancer patients.

TVDT predictions were compared to literature values in untreated cancer patients, showing very good agreement. Predicted and observed TVDT medians were very close (RMSE = 0.9244 months), with predictions within 1.5-fold of observations for all cancer types except for sarcoma, which was the worst-predicted case. 83.59% of the 265 individual TVDTs fell within the reported clinical ranges (80% CI). Regarding inter-patient variability, the 80% PI of predicted TVDTs aligned with the 80% CI of the clinical values. However, the comparison of observed and predicted standard deviations of TVDTs highlighted an underestimation of inter-patient variability for some cancer types. This could be partially due to the limited number of considered PDX mouse models (n=25) for each cancer type compared to the wider cohorts of patients from which the clinical estimates of TVDT were derived. Indeed, the estimated inter-PDX variability increased with the number of PDX mouse models (intermediate results not shown), supporting this hypothesis. Other causes, such as the intrinsic limitation of PDX mouse models in capturing inter-patient heterogeneity or non-exponential growth of tumors in humans, could not be excluded.

Regarding PFS curves, KM-VPC plots were constructed comparing simulated clinical trials, each composed of 200 patients, with PFS plots from published clinical studies. No useful PFS data were found in the literature for BR cancer, ADC, and SCC of the lung. Additionally, studies including patient cohorts receiving placebo were available only for some cancer types (i.e., CC, CR, LI cancers, and SA). For others, PFS predictions were compared with those reported in studies involving patient cohorts treated with supportive care or therapies exerting limited anticancer effects on tumor growth (ORR $\leq$ 10%). Even though the comparison is qualitative, it is interesting to note that in most cases, the observed and simulated curves are close, suggesting that the translational modeling approach is suitable for predicting PFS in the absence of drug anticancer effects. Results are further confirmed by the agreement between the observed and predicted median PFS.

Nevertheless, further considerations about the assumptions and hypotheses made are needed.

First, the approach relies on the assumption that the natural growth of human solid tumors can be approximated by exponential growth, at least during the clinical observational period. Second, the exponential tumor growth rates were allometrically scaled from mice to humans according to body weight raised to the power of $-\alpha$, as typically done for metabolic rates. Even though the allometric scaling approach to tumor growth has already been applied in other translational works, this is the first study where tumor growth dynamics were simultaneously scaled in a multitude of cancer types using the same allometric mouse-human conversion factor, which is a different assumption compared to the one made by Baaz et al [81]. α was first fixed to 1/3, and then estimated by minimizing the differences between the observed and predicted median TVDTs. The value simultaneously estimated for all eleven cancer types (α = 0.3444, SE = 0.00684) was very close to the fixed allometric factor, supporting the initial choice. α values separately estimated for each cancer type were strongly consistent (α ranged from 0.3068 to 0.3753 for all cancer types, except for SA, for which α = 0.1070 – see Table A7 in Appendix A) and always close to 1/3, providing further empirical support to the adopted allometric scaling rule. Third, PFS curves consider, by definition, both PD events and deaths. In RECIST 1.1, PD events were defined as: i) target lesion progression (i.e., at least a 20% increase in SLD of target lesions with an absolute increase of at least 5 mm, taking as reference the smallest sum), ii) unequivocal progression of existing non-target lesions, or iii) appearance of one or more new lesions. However, in this work, PFS curves were simulated considering only PD events triggered by target lesion progression, simply defined as a 20% SLD increase. Of course, neglecting non-target progression and death events could lead to a possible overprediction of PFS. Conversely, not imposing the 5 mm threshold on the absolute SLD increase of the target lesions could potentially result in an overprediction of PD events and thus in an underprediction of PFS, balancing the previous bias. Finally, in this work, eleven different solid cancer types were considered, clustered and classified by primary site and/or histological type. More specific sub-stratification based on molecular characteristics and/or gene expression was hampered by the lack of adequate panels of PDX mouse models and clinical data for validating predictions. This led to an over-generalization of certain cancer types.

Overall, the proposed framework is able to adequately predict TVDT distributions and PFS in untreated cancer patients starting only from tumor growth data in PDX mice. Due to the encouraging results, we decided to

move to the next step and include the drug effect in the translational framework.

Chapter 3

Predicting tumor growth dynamics and Progression-Free Survival in treated patients from PDX mice experiments*

In this chapter, we expand upon the previous translational framework to incorporate the impact of drug treatments on tumor dynamics. In this step our approach aims to predict both the temporal tumor dynamics and the PFS, which is subsequently derived. This chapter serves a dual purpose: proposing a framework for predicting tumor dynamics in clinical settings and validating this approach using two preclinical-clinical case studies.

This chapter structure mirrors Chapter 2. Section 3.1 introduces the general framework for translating TGI from PDX mouse models to clinical settings. Section 3.2 presents case studies, and the associated data used to develop and validate the framework. Subsequently, Section 3.3 focuses on the developed TGI model in PDX mice, while Section 3.4 discusses the scaling process and compares tumor growth dynamics and PFS curves with those observed in existing literature. Finally, Section 3.5 summarizes and discusses the key findings, providing a detailed interpretation of the results and offering a rationale for advancing to the next phase of the study. It also briefly addresses potential directions for future research.

** The content of this chapter is also presented in the article titled "Predicting Tumor Dynamics and Progression-Free Intervals in Treated Patients from Patient-Derived Xenograft Mouse Models: A Translational Model-Based Approach," which has been submitted to the Journal of Pharmacokinetics and Pharmacodynamics.*

3.1. Translational framework for tumor growth dynamics under anticancer treatments

Starting with the translational framework introduced in Section 2.1, a modeling approach is developed to forecast tumor size dynamics and PFS curves for cancer patients undergoing specific anticancer treatments, using TGI data obtained from PDX mice. This approach (Figure 3.1) follows a multistep procedure. Initially, a population TGI model is constructed to characterize the distribution of exponential tumor growth rates and the potency of anticancer drugs in PDX mice. Subsequently, these parameters are scaled allometrically from mice to humans and utilized to construct a TGI model that predicts tumor size dynamics in treated cancer patients. Next, OS TTE model built on historical clinical studies is integrated to incorporate mortality outcomes. Finally, the predicted tumor size dynamics and mortality processes are employed to derive corresponding PFS curves.

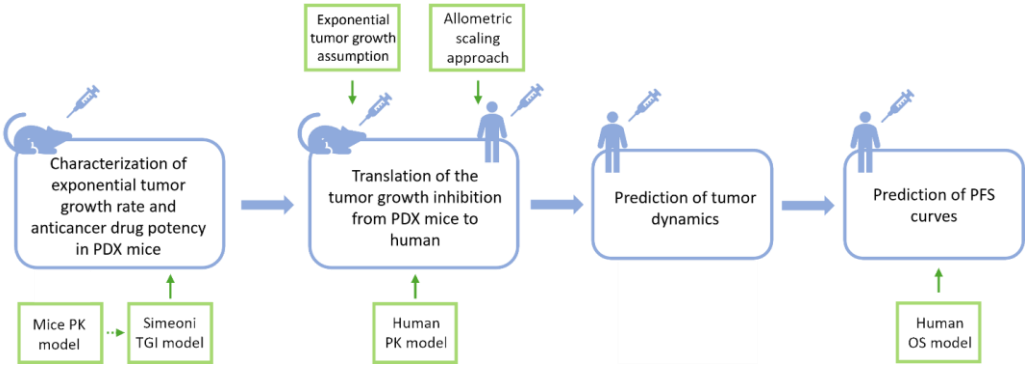

Figure 3.1 Flow chart representing the translational modeling approach.

3.1.1. Mathematical modelling of TGI in PDX mice

The first step is the characterization of PDX tumor size dynamics using a TGI model describing exponential tumor growth and drug effects. A population-based approach is employed to simultaneously analyze data from all PDX studies. In herein described version of this framework, drug effects are driven by drug concentration profiles and modeled with a first-order drug effect parameter. This model structure will be referred to henceforth, while the overall framework can be adapted affectively to accommodate variations.

Both the exponential growth rate, k_g, and drug effect, k_d, are assumed to follow lognormal distributions and are parametrized accordingly. The lognormal distribution of the exponential growth rate is parametrized as

$k_{g,i} = k_{g,pop} \cdot e^{\eta_{k_g,i}}$ as well as the drug effect $k_{d,i} = k_{d,pop} \cdot e^{\eta_{d,i}}$, where $k_{g,pop}$ and $k_{d,pop}$ represents the typical population parameter (median) for a specific cancer type, and (η_{k_g}, η_{k_d}) are normally distributed and follow a multivariate normal distribution with mean zero and standard deviation $\Omega = \begin{pmatrix} \omega_{k_g}^2 & \omega_{k_g,k_d} \\ \omega_{k_g,k_d} & \omega_{k_d}^2 \end{pmatrix}$, accounting for inter-PDX model variability and eventual correlation between random effects. $k_{g,i}$ and $k_{d,i}$ represents the exponential tumor growth rate and the drug potency of the i^{th} - PDX model, respectively.

Plasma concentration values can be incorporated into the model using different approaches. If PK data were collected simultaneously with the TGI study being analyzed, a PK/PD model could be developed. However, if PK information was already available from a previously developed model, that model could be used to derive the plasma concentration values.

3.1.2. Scaling of exponential growth rate and anticancer drug potency

The exponential tumor growth rate and drug potency are scaled up from PDX mice to humans. Following the strategy proposed in the unperturbed tumor step (Eq. 1), an allometric scaling approach is applied also to drug-related parameter:

$$k_{d,human}\left[\frac{L/g}{months}\right] = 30 \cdot k_d[\frac{L/g}{days}] \cdot \left(\frac{BW_{human}}{BW_{Mice}}\right)^{-\alpha} \cdot \frac{f_{u,human}}{f_{u,mouse}} \quad (4)$$

where BW_{human} and BW_{mouse} represented the standard body weight of humans (70Kg) and mice (0.025Kg), respectively, α (=1/3) was the allometric exponent and $f_{u,human}$ and $f_{u,mouse}$ represent the drug-specific unbound fraction in human and mouse, respectively.
A multivariate lognormal distribution is predicted propagating the inter-PDX variability. Distribution is parametrized as follows:

$$\begin{pmatrix} k_{g,human,i} \\ k_{d,human,i} \end{pmatrix} = \begin{pmatrix} k_{g,human,pop} \\ k_{d,human,pop} \end{pmatrix} e^{\overline{\eta}_{human,i}} \quad (5)$$

where $\overline{\eta}_{human} = \left(\eta_{k_{g,human}}, \eta_{k_{d,human}}\right)^T \sim N(0, \Omega_{human})$ with $\Omega_{human} = \Omega$.

3.1.3. Predicting tumor dynamics in treated cancer patients

Tumor volume dynamics in treated cancer patients is supposed to be described by the Claret's TGI model [64] assuming no resistance effect acting of the drug effect in inhibiting tumor growth:

$$\frac{dTV(t)}{dt} = (k_{g,human} - k_{d,human} \cdot c(t)) \cdot TV(t) \quad (6)$$

where *TV(t)* denotes the tumor volume, $k_{g,human}$ the exponential tumor growth rate, $k_{d,human}$ the anticancer drug potency and $c(t)$ the plasma drug concentration.

As tumor diameter is generally used as a measure of structural tumor changes in the clinical settings, the model-predicted tumor volume $TV(t)$ is converted into the corresponding tumor diameter $TD(t)$ using the formula for a sphere:

$$\boldsymbol{TD(t) = 2 \cdot \sqrt{\frac{3 \cdot TV(t)}{4\pi}}}$$

Drug concentration profiles could be either simulated from an existing PK model or could be predicted from preclinical/nonclinical study for a fully translational step.

3.1.4. Simulating tumor dynamics and PFS curves in treated cancer patients

In order to simulate tumor dynamics, 200 virtual cancer patients are generated, each characterized by a set of individual parameters of the Claret TGI model [64], i.e., ($k_{g,human,j}$; $k_{d,human,j}$; $TV_{0,j}$). In particular, $k_{g,Human,j}$ and $k_{d,Human,j}$ are extracted from the scaled multivariate lognormal distribution. Instead, $TV_{0,j}$ is sampled from the distribution of observed tumor volumes, if the purpose is to compare tumor growth trajectories, or fixed at a unit value, if the purpose is only to derive disease progression curves. For each virtual cancer patient, the dynamics of tumor diameter are simulated assuming strict adherence to the treatment protocol without any modifications or interruptions throughout the entire simulation time.

To compute PFS, the time to progression, $T_{p,j}$, for the virtual patient j is derived from the predicted individual tumor dynamics, $TD_j(t)$. To this end, following the simplification hypothesis adopted in the previous Chapter, only PD events caused by a 20% increase of pre-identified target lesion are considered. Then, to account for death events, a TTE model for mortality risk is coupled to sample patient's time of death $T_{d,j}$. Finally, time of PFS event (i.e. PD event or death) is computed combining time to progression and time to death as $T_{PFS,j} = \min(T_{p,j}, T_{d,j})$. A Monte Carlo simulation framework, accounting for parameter estimation uncertainty, is employed to enhance the generalizability and robustness of predictions. To this end, the previous procedure is repeated 1000 times, i.e., 1000 in silico trials in 1000 virtual patient cohorts each composed by 200 individuals are performed. Medians and 90% prediction intervals (90%PIs) across the 1000 replicates are, then, computed for both tumor diameter trajectory and PFS curve. Additional details on the simulation procedure were reported in the Appendix B (*Montecarlo simulation procedure* section).

3.2. Case studies and data availability

Two case studies have been used to develop and validate this translational step. The choices of this case studies have been due to data availability of both preclinical and clinical data. The first case study regards patients with pancreatic cancer treated with Gemcitabine, the second one regards patients with hepatocellular cancer treated with Sorafenib.

3.2.1. In vivo TGI studies in PDX mice

Two panels of PDX mouse models for pancreatic (n=27) and hepatocellular (n=24) cancer were derived from HuBase database (Crownbio Bioscience Inc., https://www.crownbio.com/). For each PDX mouse model a single TGI study composed of a control and a treated arm (both involving several mice) was selected. For pancreatic cancer, treated mice received Gemcitabine administered intraperitoneally (i.p.) or intravenously (i.v.) with different protocols. For hepatocellular cancer, Sorafenib was administered orally (o.s.) to treated mice at different dose and schedules.
For each TGI study, average tumor weights in control and treated arms were made available. The complete list of analyzed experiments with information on the administration protocols can be found in Table B1 and Table B2 in Appendix B for pancreatic cancer-Gemcitabine and hepatocellular cancer-Sorafenib, respectively.

3.2.2. TGI and PFS data in cancer patients

To accurately validate TGI and PFS predictions, it is essential to gather reliable clinical data across various cancer types and treatments.

Longitudinal tumor profiles in pancreatic and hepatocellular patients receiving Gemcitabine or Sorafenib, respectively, were searched to validate predicted tumor dynamics. For Gemcitabine treatment of pancreatic cancer, the TGI model for the SLDs developed by Garcia-Cremades et al. [80] was taken as reference. Instead, for sorafenib treatment of hepatocellular cancer, no adequate clinical data or models for longitudinal tumor dynamics were found.

Additionally, for each case study, literature was searched to retrieve appropriate PFS data to validate PFS predictions. KM plots from clinical studies published in the literature were digitized. The median PFS values and their 90% confidence intervals (90%CI) were reconstructed, following the procedure described in the previous chapter.

For pancreatic cancer, in all the selected studies (reported in Table 3.1) patients are assumed to be treated following the nominal standardized protocol for Gemcitabine monotherapy: weekly 30-minute i.v. infusion of 1000 mg/m2 for 7 weeks (or until unacceptable toxicity), followed by a 1-week rest period; subsequent cycles involved weekly infusions for 3 consecutive weeks out of every 4 [147].

Table 3.1 Selected PFS data for the gemcitabine treatment of the pancreatic cancer.

Reference	Number of patients in the Gemcitabine group	Median [90%CI] PFS time [months]	1-year survival rate
Hong [148]	56	3.6 [3.0 – 4.2]	31.7%
Kindler [149]	316	4.4 [3.9 – 5.0]	24.0%
Nakai [150]	53	3.6 [2.3 – 4.8]	30.2%
Ozaka [151]	59	3.8 [2.4 – 5.1]	29.0%

For hepatocellular cancer, ethnicity resulted a significant covariate for both tumor growth rate and response to sorafenib treatment [136, 152]. Studies have shown that Asian patients experienced shorter PFS compared to non-Asian ones [135]. Since all the considered PDX mouse models are derived from Asian patients (Table B2), the analysis is limited to clinical trials involving only Asian patients. Selected studies are listed in Table 3.2. In all

of them, the nominal protocol involved 400 mg of Sorafenib (two 200 mg tablets) taken orally twice daily, amounting to a total daily dose of 800 mg. Treatment should be maintained until either a clinical benefit is evident or unacceptable levels of toxicity are reached [153].

Table 3.2 Selected PFS data for the gemcitabine treatment of the pancreatic cancer.

Reference	Number of patients in the Sorafenib group	Median [90%CI] PFS time [months]	1-year survival rate
Park [154]	169	3.6 [3.1 -3.8]	46.5%
Qin [155]	331	3.6 [3.1 – 3.7]	45.0%
Kudo [156]	103	3.5 [2.7 - 4.3]	46.1%
Lyu [157]	132	4.3 [3.7 – 4.9]	25.8%

3.3. TGI Model in PDX mice

For each case study, the PK/PD Simeoni TGI model [67] is used to describe TGI data and characterize the exponential tumor growth rate and anticancer potency in PDX mice. In absence of treatment, the model assumes an exponential tumor growth pattern followed by a linear one, which are determined by the rates $\lambda_0\,[1/day]$ and $\lambda_1\,[cm3/day]$, respectively. In treated animals, the model assumes that a fraction of cells, hit by the drug, becomes not proliferating and progresses to death through a sequence of three damage stages according to the first-order constant $k_1\,[1/day]$. Anticancer drug effect is governed by plasma concentration through the $k_2\,[\frac{L}{mg \cdot day}]$ parameter representing the drug potency.

Drug concentration profiles in input to the Simeoni TGI model is simulated with PK models derived from the literature. For Gemcitabine i.v. the two compartment model with linear elimination reported in [75] is used. For i.p. administration, a linear absorption compartment is added, and absorption rate is identified on data derived from [74]. For Sorafenib o.s., the two compartment PK model developed by Choi et al. [158] is adopted. For both the case studies, details about the PK models and the parameter values are reported in the *Mice PK models* in Appendix B.

Model fitting is performed assuming i) for the Gemcitabine – pancreatic cancer case study, a combined residual error, i.e., $y = f + b \cdot f \cdot \varepsilon_1 + a \cdot \varepsilon_2$, where $\boldsymbol{y}$ is the measurement, a a coefficient representing the standard error, b a coefficient representing the coefficient of variation, $\boldsymbol{f}$ the model

prediction and ε_1 and ε_2 standardized random variables normally distributed and ii) for the Sorafenib – hepatocellular cancer case study, a proportional residual error, i.e., $y = f + b \cdot f \cdot \varepsilon$, where $\boldsymbol{y}$ is the measurement, b a coefficient representing the coefficient of variation, $\boldsymbol{f}$ the model prediction and ε a standardized random variable normally distributed. Random effects accounting for inter-PDX variability is introduced on all the parameters. Correlation is included only between random effects of λ_0 and k_2.

Estimated parameters for the two case studies are reported in Table 3.3, diagnostic plots in the *Model fitting of preclinical TGI studies* section in Appendix B.

Table 3.3 Estimated TGI model parameters in PDX mice.

Parameter		**Gemcitabine - Pancreas cancer ****	**Sorafenib - Hepatocellular cancer *****
$\lambda_0[day^{-1}]$	$\lambda_{0,pop}$	0.1 (11.4%)	0.11 (3.72%)
	ω_{λ_0}	0.61 (16.6%)	0.54 (18.3%)
$\lambda_1[cm^3 \cdot day^{-1}]$	$\lambda_{1,pop}$	0.037 (16.2%)	0.056 (11.9%)
	ω_{λ_1}	0.8 (14.4%)	0.51 (17.3%)
$k_1[day^{-1}]$	k_1	0.21 (46.4%)	2.17 (33.8%)
	ω_{k_1}	1.97 (24.4%)	1.01 (28.1%)
$k_2[L * mg^{-1} * day^{-1}]$	k_2	0.56 (32.4%)	0.0061 (13.2%)
	ω_{k_2}	1.55 (19.0%)	0.63 (16.1%)
TV_0 $[cm^3]$	TV_0	0.0069 (26.0%)	0.18 (4.0%)
	ω_{TV_0}	1.23 (14.7%)	0.17 (16.5%)
ρ_{k_2,λ_0} *		0.44 (64.1%)	0.87 (6.8%)
$a[-]$		0.0036 (21.4%)	-
$b[-]$		0.13 (4.2%)	0.092 (3.8%)

Notes: (*) $\rho_{k_2,\lambda_0} = \omega_{\lambda_0,k_2}/(\omega_{\lambda_0} \cdot \omega_{k_2})$ is the correlation between the random effects of λ_0 and k_2. (**) Initial tumor size is referred to time of the inoculous. (***) Initial tumor size is referred to the first measurement.

It is critical to note that within this framework, the exponential tumor growth rate k_g corresponds directly to the parameter λ_0 , while the anticancer drug potency rate k_d corresponds to the parameter k_2. This correspondence is fundamental for translating purposing.

3.4. Predicted tumor growth dynamics and PFS in treated cancer patients

Estimated values for the tumor growth rate and anticancer drug potency, λ_0 (equivalent to k_g) and k_2 (equivalent to k_d), are scaled up from mice to humans according to the allometric rules reported in Eq.1 and Eq.4. $\frac{f_{u,human}}{f_{u,mouse}}$ ratio is set to 1 in both case studies [159, 160], assuming no significant difference in the unbound fraction between species.

To complete the translational framework, for both case studies, the TTE models for mortality risk were developed based on OS data from the literature clinical trials with the largest patient cohorts, i.e. [149, 154], respectively (please refer to *Time to event model building for OS* section in Appendix B).

3.4.1. Gemcitabine treatment of pancreatic cancer

Virtual patients ($k_{\mathrm{g},human,j}$; $k_{\mathrm{d},human,j}$) distribution is plotted in Figure 3.2.

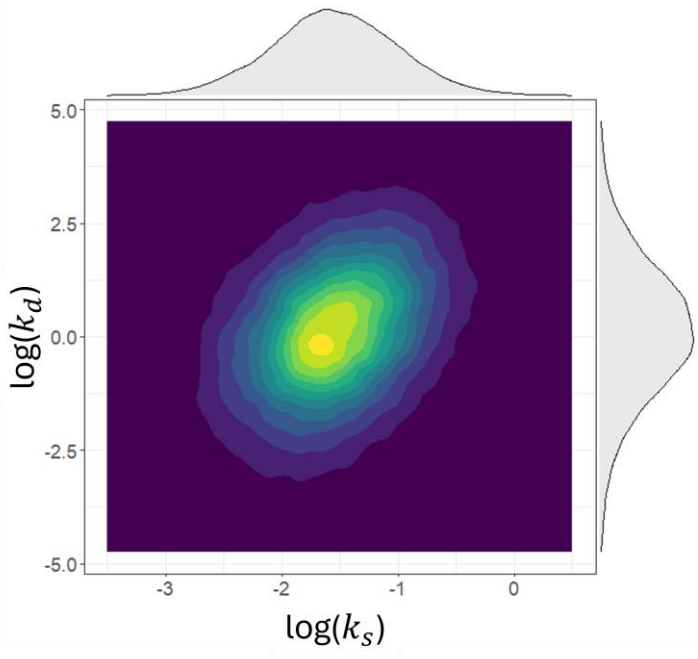

Figure 3.2 Log-transformed marginal distributions of the $k_{\mathrm{g,Human}}$ and $k_{\mathrm{d,Human}}$ for the generated pancreatic cancer virtual patients treated with gemcitabine.

The initial tumor size TV_0 values are derived from a lognormal distribution based on the work of Garcia-Cremades et al [80]. In particular, $TV_{0,i}$ $[cm^3]$= 115.3e$^{\eta_{TV\,i}}$ where $\eta_{TV\,i} \sim N(0,0.16)$ is obtained transforming the distribution of initial tumor size reported in terms of volumes.

Drug concentration profiles are simulated using the population PK model developed by Zhang et al. [161] where gemcitabine i.v. pharmacokinetic is described by the two compartment-model.

Longitudinal tumor dynamics predicted from the PDX data are compared with SLD profiles simulated using the TGI model of Garcia-Cremades et al [80]. To allow comparison, the simulation procedure to simulate clinical data from preclinical is applied also for the clinical TGI model adopted as reference. Comparing predictions of the two models (Figure 3.3), a notable overlap between the curves is evident.

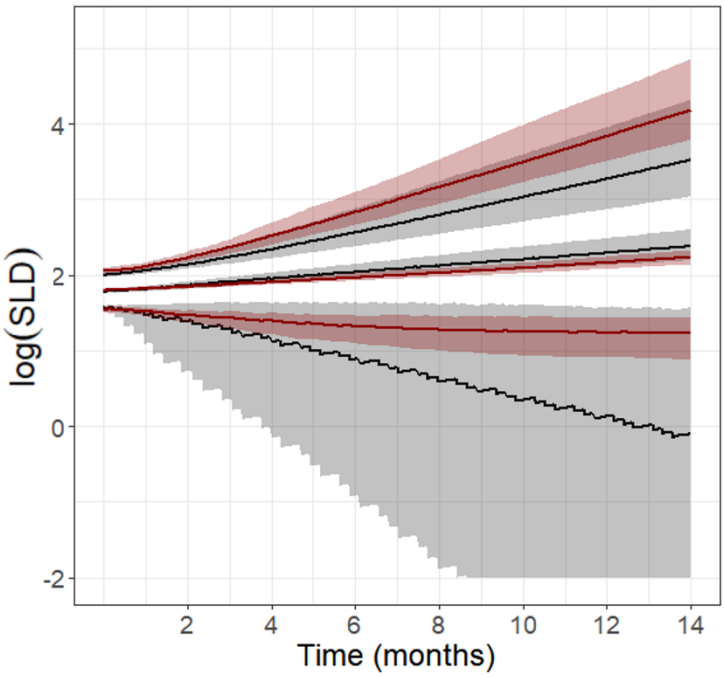

Figure 3.3 VPC of the simulated SLD trajectories over a 14-months period under the standard gemcitabine treatment schedule. Simulated tumor dynamics predicted from PDX mice data and by the Garcia-Cremades TGI model were reported in black and red, respectively. Solid lines represent the median and the 5th and 95th percentiles; dashed areas the corresponding 90%PI.

Overall, tumor profiles predicted from PDX data are in good agreement with the SLD trajectories simulated using the reference clinical model. In particular, the two median tumor profiles result very closed for the entire

period, showcasing nearly complete alignment between the model informed by the PDX studies and the one developed based on clinical data. However, considering the 5th and 95th percentiles, the model informed from the PDX data predicts a greater anticancer effect for Gemcitabine or a slower tumor growth respect to the clinical model. This discrepancy is probably due to the presence of a drug resistance mechanism that is incorporated in the model developed by Garcia et al., resulting in a diminished effect already after 2 months, and not consider in the TGI model scaled from PDX mice.

Regarding PFS, the translational approach predicts a median T_P of 5.6 months, with a 90%PI between 2.6 and 8.5 months. The TTE model that best describes the mortality risk is a generalized gamma distribution which predicts a median T_d of 8.1 months, with a 90%PI = [6.6, 9.5]. Time of PFS events is computed combined T_p and T_d. According to the fact that pancreatic cancer is associated with elevated mortality risk and shorter life expectancy (Table 3.1), deaths are the most frequent triggering events for PFS dynamics, accounting for an average of 60.0% (range 38.5-78.0%) of PFS events. The predicted median PFS duration T_{PFS} stood at 3.7 months, with a 90%PI = [2.4, 5.5] months. Both the median duration (Table 3.1, Figure 3.4A) and the overall shape of the PFS curve (Figure 3.4B) align closely with clinical observations.

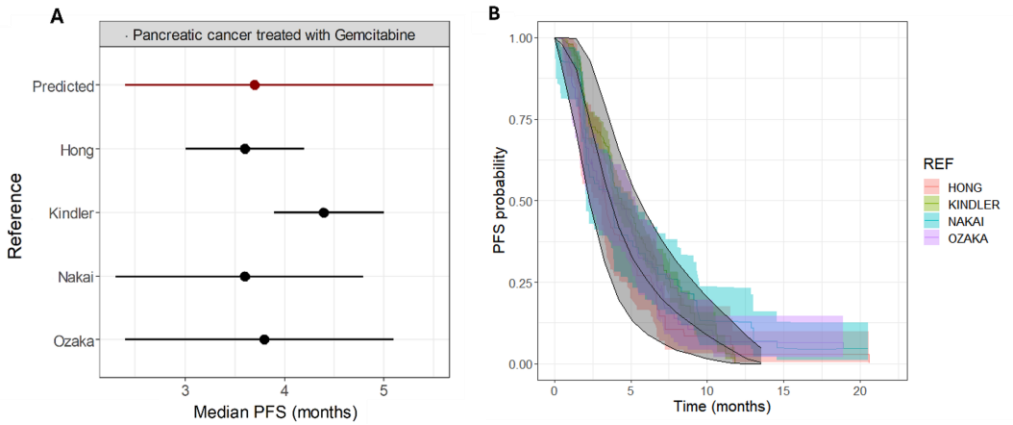

Figure 3.4 (A) Median PFS times for pancreatic cancer treated with Gemcitabine. Solid dots and lines indicate the median PFS times and their 90%PI, respectively, with black representing reference data and red representing predicted values. **(B)** KM-VPC plots (grey areas) generated from 1000 virtual clinical trials composed of 200 individuals with pancreatic cancer treated the standard gemcitabine schedule were superimposed to PFS curves taken from literature studies (colored areas). Medians and 90%PI were reported.

3.4.2. Sorafenib treatment of hepatocellular cancer

Virtual patients ($k_{\mathrm{g},human,j}$; $k_{\mathrm{d},human,j}$) distribution is plotted in Figure 3.5.

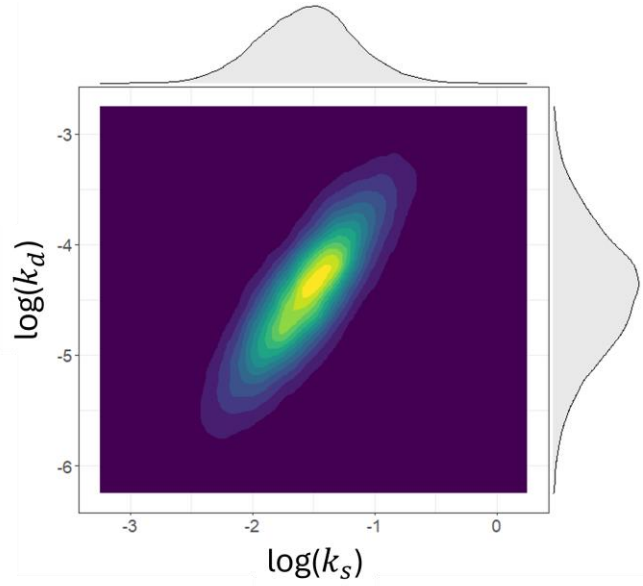

Figure 3.5 Log-transformed marginal distributions of the k_{g} and k_{d} for the generated hepatocellular cancer virtual patients treated with sorafenib.

Sorafenib concentration profiles are simulated using the population PK model developed by Jain e al. [162]. It is composed by a central compartment and a four-compartment transition chain to account for absorption delay. Additionally, a semi-mechanistic model is integrated to depict the recirculation of the drug within the intestinal tract, known as enteropathic circulation.

Unfortunately, for this case study adequate clinical data or mathematical models for longitudinal tumor dynamics to use as reference are not available. Therefore, initial tumor volume size $TV_{0,j} = 1\,cm^3$ since only PFS prediction can be matched with clinical data.
Despite so, longitudinal tumor dynamics predicted from the PDX data are still produced and reported in Figure 3.6.

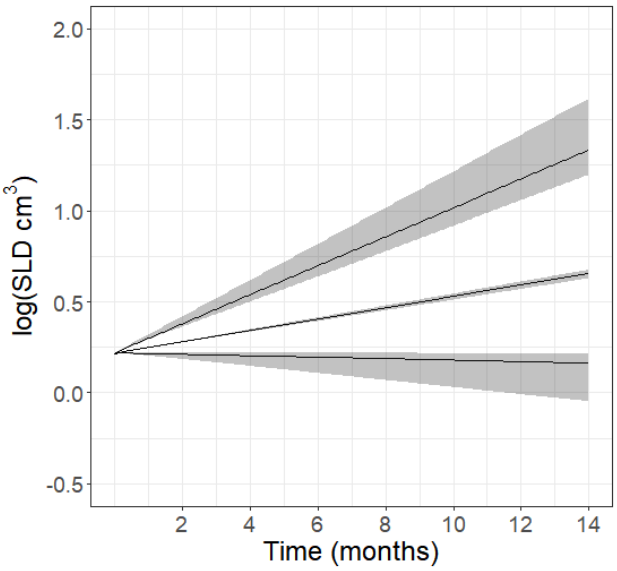

Figure 3.6 VPC of the simulated SLD trajectories over a 14-months period under the standard sorafenib treatment schedule. Solid lines represent the median and the 5th and 95th percentiles; dashed areas the corresponding 90%PI.

Regarding the PFS predictions, the translational approach predicts a median T_p of 5.1 months, with a 90%PI from 4.2 to 5.9 months. In this case, death events, modeled using a log-logistic function predicts a median T_d of 10.8 months, with a 90%PI = [8.1, 14.9]. Death has a smaller impact on PFS dynamics according to the relatively lower aggressiveness of hepatocellular cancer compared to pancreatic cancer (Table 3.1, 3.2 and Table B5, B8). Death triggered only 26.0% of PFS events (range of 19.5-41.5%). Ultimately, while the predicted median PFS of 4.3 months (90% PI 3.6-5.2 months) shows reasonable alignment with the observed data (Fig. 3.7), it is worth noting that the median predicted PFS falls outside the confidence intervals for three out of four studies. Additionally, while the shape of the PFS vs. time curve generally reflects the observed data, there are some deviations, particularly towards the end.

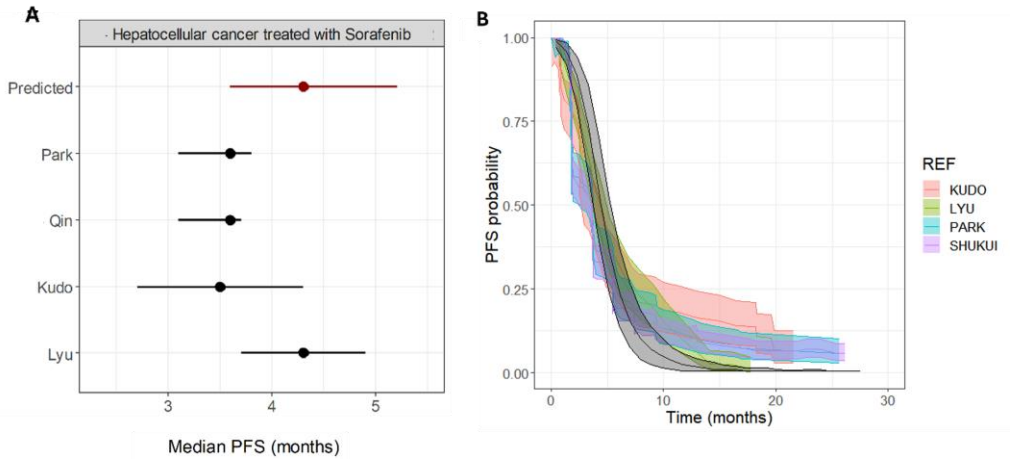

Figure 3.7 (A) Median PFS times for hepatocellular cancer treated with Sorafenib. Solid dots and lines indicate the median PFS times and their 90%PI, respectively, with black representing reference data and red representing predicted values. **(B)** KM-VPC plots (grey areas) generated from 1000 virtual clinical trials composed of 200 individuals with hepatocellular cancer treated the standard Sorafenib schedule were superimposed to PFS curves taken from literature studies (colored areas). Medians and 90%PI were reported.

3.5. Wrap up and future developments

In this work, a translational modeling framework to predict longitudinal tumor size dynamics and PFS curves in cancer patients undergoing an anticancer treatment from TGI data in PDX mice was proposed. To this end, the unperturbed tumor-based translational approach presented in the previous section was extended to incorporate the effects of anticancer therapies. The result is a multistep procedure that, from a theoretical point of view, can be applicable to a multitude of cancer type and anticancer treatment. This general approach was here applied on two case studies, i.e., the gemcitabine treatment of pancreatic cancer and the sorafenib treatment of hepatocellular cancer. For each cancer type and anticancer treatment, first, a set of TGI studies in a panel of PDX mouse models was analyzed through a mathematical modeling approach to estimate the exponential tumor growth rate and the drug anticancer potency in PDX mice. To this aim, the Simeoni TGI model [67] was applied and combined with a population (non-linear mixed effect) approach. A multivariate lognormal distribution for the exponential tumor growth rate and anticancer drug potency was identified accounting for the inter-PDX variability. Second, parameters were scaled up from PDX mice to humans adopting an allometric scaling strategy (Eq. 1,4). The inter-PDX variability was propagated, and a multivariate log-normal

distribution was derived for, $k_{g,Human} - k_{d,Human}$ (Eq. 5). Scaled parameters were used to inform a TGI model predicting tumor size dynamics in cancer patients under anticancer drug treatment. To this end, the Claret TGI model [64] was adopted and combined with clinical PK models derived from the literature. Third, PD events were computed based on the simulated tumor size dynamics. They were combined with a TTE model for mortality risk, which was derived from literature data, to construct the expected PFS curves.

For the case study of gemcitabine treatment of pancreatic cancer, a panel of 27 TGI studies in PDX mouse model was considered. From that, the longitudinal tumor size dynamics in a population of virtual patients undergoing standard Gemcitabine administration protocol were predicted. SLD profiles simulated with a TGI model directly developed on clinical data were used as benchmark against which validate the predictions. The scaled TGI model informed from PDX data demonstrated robust predictive capabilities, predicting a median SLD profile extremely closed to the clinical one. Differently, more extreme percentiles, i.e., 5th and 95th percentiles, of clinical SLD profiles resulted under-predicted by the PDX-informed TGI model. This discrepancy could be due to different factors. For example, the model derived from the PDX data did not consider the mechanism of resistance to Gemcitabine, which was instead incorporated into the clinical model. Further, the inter-individual variability affecting tumor growth and response to Gemcitabine in cancer patients could not be fully grasped by the inter-PDX viability identified on limited number of PDX mouse model. A not-perfectly exponential growth of pancreatic cancer could not be a priori excluded. For what regard predictions of PFS, considering only PD events (due to target lesions), not including any drug-resistance, and neglecting deaths resulted in overestimation of the PFS times reported in the clinical trials (Figure B7 and B8 of Appendix B). However, when death events were incorporated by integrating a TTE model for mortality risk, the predicted PFS curves were closely aligned with clinical outcomes.

Similarly, for sorafenib treatment of hepatocellular cancer, 24 TGI studies in PDX mice were analyzed with the Simeoni TGI model and parameter estimates used to inform the TGI model in humans. The predicted tumor size profiles in patients under standard sorafenib administration exhibited plausible dynamics. However, the lack of adequate clinical data or model prevented an actual validation. Regarding PFS, the translational modeling approach was able to adequate predict PFS curves, providing estimates of median PFS in good agreement with clinical observations. Here including death events in the PFS computation exerted a limited effect respect to the Gemcitabine case study, although predictions of PFS curves were improved.

The different impact of deaths in the two case studies was likely due to the different mortality risk (Table 3.1 and 3.2).

Overall, the translational modeling framework resulted able to adequately predict tumor size dynamics and PFS in cancer patients undergoing anticancer treatments starting only from TGI data in PDX mice. Consequently, it could be a powerful tool to support the extrapolation of preclinical findings into the clinical settings. However, some limitations should be considered. First, a robust validation of the predicted tumor size dynamics is still missing due to the lack of adequate clinical data to use as benchmark. The TGI model adopted to describe tumor dynamics in humans relied on some relevant assumptions, such as an exponential tumor growth and an anticancer effect proportional to plasma drug concentration. These assumptions, here due to availability of data, was commonly adopted also in models directly developed on clinical data. Nevertheless, the presence of possible more complex dynamics, such as non-exponential tumor growth or resistance mechanisms to treatment, could not been exploded. Furthermore, PFS consider, by definition, both PD events and deaths. Accordingly, modeling of death events had a significant impact on the predicted PFS dynamics, especially for cancer type, such as pancreatic cancer, associated with a high mortality risk. In the present work, probability of death was not predicted from PDX studies but was described by a TTE model developed on clinical OS data from the literature. This represents a limitation of the current translational framework, as it requires the integration of clinical information to correctly predict PFS. Finally, although the proposed translational modeling framework intended to be a general approach applicable to different cancer type and anticancer treatment, it was evaluated only on two case studies. A further validation of the approach across a panel of cancer types and anticancer treatment is necessary to demonstrate generalizability of the obtained findings.

Due to the encouraging results, we decided to move to the next step and explore possible applications of the proposed translational strategy

Chapter 4

Dynamic borrowing of synthetic patients for hybrid control arm generation

In this chapter, we present the first application of the proposed translational framework. Specifically, we utilize this framework to create virtual cancer patients, which are then used, through frequentist dynamic borrowing techniques, to replace real patients in the control arms of clinical trials.
Section 4.1 introduces the concepts of external and synthetic control arms. Section 4.2 describes the available dynamic borrowing techniques to integrate external/synthetic control data into clinical trials. Section 4.3 describes the case studies, and the data used to evaluate the proposed application. Section 4.4 details the proposed pipeline for borrowing patients and describe the evaluation procedure used to assess the effectiveness of the approach. Section 4.5 presents the results, while Section 4.6 serves to wrap up and conclude the chapter.

4.1. Control arm in cancer trials

The control arm of a randomized clinical trial plays a fundamental role in estimating the efficacy and safety of an investigational therapy [163]. In oncology trials, patients in the control arm typically receive either a placebo or, more commonly, a reference treatment that represents the current standard of care [164]. Concurrently randomized control arms allow for an

understanding of temporally relevant factors associated with the natural history of the disease, particularly concerning contemporary clinical practices. This means that patients in both the experimental and control arms are randomized at the same time, ensuring that any differences in outcomes can be attributed to the treatment being tested, rather than changes in external factors over time [165]. Randomization also minimizes bias by balancing both measured and unmeasured prognostic factors across the treatment groups. However, for this study design to be effective, enough patients must be enrolled in the trial to ensure statistically meaningful results [166]. Unfortunately, cancer clinical trials often struggle with low enrollment, which can delay research progress and increase the cost of developing and disseminating effective cancer treatments [167]. Researchers have identified numerous barriers to patient participation in clinical trials. Factors affecting motivation to participate include patient attitudes, perceptions of clinical trials, limited awareness, and willingness. Complex trial designs with strict inclusion and exclusion criteria further reduce the number of eligible participants. Inconsistent trial implementation and inadequate recruitment strategies can also hinder enrollment. Additionally, a lack of familiarity with and access to clinical trials on the part of healthcare providers often limits patient referrals [167–169].

When a concurrently randomized arm is not feasible in an oncology trial, single-arm trials may be an appropriate alternative. In these trials, tumor response rates serve as the endpoint for assessing treatment effect, with each patient's baseline tumor measurement acting as an internal control [163]. This approach relies on the assumption that most tumors will not shrink without intervention.

4.1.1. External and synthetic control arms

The US FDA has accepted the use of external controls to support regulatory decisions when justified [170]. External controls refer to control groups that are not part of the same randomized study as the investigational therapy group. Instead, these controls are derived from data sources outside the trial, such as results from other clinical trials, case studies, clinical experience documented in the literature, patient registries, or real-world data [171]. For example, external controls have been successfully used to support the accelerated approvals of blinatumomab and avelumab [172, 173]. However, relying on external controls can introduce biases, such as those related to patient selection or changes in disease prognosis and supportive care over time. These biases are significant factors that can contribute to high failure

rates in subsequent trials, highlighting the limitations of using external controls alone [174].
To address some of the limitations associated with external controls, Synthetic Control Arms (SCAs) offer a more advanced approach. Unlike static external controls, SCAs create virtual control groups using advanced statistical techniques. By leveraging historical data and various covariates, SCAs simulate what the outcomes might be in the absence of treatment, aiming to reduce biases related to baseline differences and other factors. This innovative method helps to overcome the challenges of limited or unavailable historical control data and allows for more precise and dynamic comparisons in clinical trials. The use of SCAs has gained significant interest for its potential to streamline trial design, improve efficiency, and support more informed decision-making in cancer research.

In summary, while external controls offer valuable insights, SCAs enhance trial accuracy by integrating and adjusting for a range of variables, thus bridging the gap between real-world complexities and controlled trial settings.

4.2. Dynamic borrowing methods for SCA

Building on the discussion of external and SCAs, this section will investigate into methods for assessing and utilizing external data in clinical trials. Specifically, we will explore how external data borrowing [175–178], when combined with matching techniques, can be used to create more robust SCAs. We will review three widely used methods for dynamic data borrowing, focusing on how they help evaluate the similarity between external studies and current trials to determine the feasibility of integrating external data effectively.

Presenting the different techniques requires introducing three types of data: i) Data of current active treatment group: $\boldsymbol{Y_T} = Y_{T,1}, \dots, Y_{T,N_T}$ consists of N_T independent and identically distributes (iid) samples from a distribution with true mean μ_T and true variance σ_T^2. ii) Data of current control group: $\boldsymbol{Y_C} = \{Y_{C,1}, \dots, Y_{C,N_C}\}$ consists of N_C iid samples from a distribution with true mean μ_C and true variance σ_C^2. iii) Data of external control group: $\boldsymbol{Y_E} = \{Y_{E,1}, \dots, Y_{E,N_E}\}$ consists of N_E iid samples from a distribution with true mean μ_E and true variance σ_E^2. The null hypothesis under consideration is $H_0: \mu_T = \mu_C$.

The techniques presented in the following section are the most widely used and are supported by the most extensive literature. However, it is important to note that other techniques exist, but they will not be covered in this thesis.

4.2.1. Test then pool

This frequentist approach first performs a congruence test between $\boldsymbol{Y_E}$ and $\boldsymbol{Y_C}$ at a prespecified significance level. If there no significant difference between $\boldsymbol{Y_E}$ and $\boldsymbol{Y_C}$, then $\boldsymbol{Y_E}$ will be fully borrowed, that is $\boldsymbol{Y_E}$ and $\boldsymbol{Y_C}$ will be pooled as the control group for the treatment effect evaluation. The selection of the significance level for congruence test is subjective. Larger significance level means more chance for historical data to be borrowed.

4.2.2. Calibrated power prior

Bayesian power prior method [179, 180] uses the external data to create an informative prior for analyzing the current data. Let θ_c denotes the effect in the current control group. Bayesian power prior method starts with a non-informative initial prior $\pi_0(\theta_C)$, and assumes that historical data can be used to update the initial prior in the following way:

$$\theta_c \mid \boldsymbol{Y_E} \propto L(\theta_c \mid \boldsymbol{Y_E})^{\delta} \cdot \pi_0(\theta_C)$$

where $0 \leq \delta \leq 1$. The above distribution is then used as prior to analyze the current data. When $\delta = 0$, no historical data are borrowed and analysis will be done using only current data; when $\delta = 1$, historical data are fully borrowed to augment current control. Thus, larger value of δ means that more information from historical data is borrowed. It is generally difficult to select an appropriate value for δ [181]. To alleviate this issue, Pan et al. [182] proposed a dynamic borrowing method by defining a calibrated power prior (CPP) using δ defined as

$$\delta = (1 + \exp(a + b \cdot \log(S)))^{-1}$$

where $S = max(N_E, N_C)^{\frac{1}{4}} \cdot KS$ with KS is the Kolmogorov–Smirnov distance (maximum difference) between the empirical distributions of $\boldsymbol{Y_E}$ and $\boldsymbol{Y_C}$, and a and $b > 0$ are tuning parameters. When $\boldsymbol{Y_E}$ and $\boldsymbol{Y_C}$ distribute differently, δ tends to be small and less historical data are borrowed; otherwise, when $\boldsymbol{Y_E}$ and $\boldsymbol{Y_C}$ distribute similarly, δ tends to be large and more historical data are borrowed.

4.2.3. Robust mixture prior

Like the CPP method, the robust mixture prior (RMP) method [183] is also a Bayesian approach. Let $\pi_H(\theta_C)$ be the distribution proportional to the likelihood $L(\theta_c \mid \boldsymbol{Y_E})$ from historical data. The RMP method suggests using the following mixture distribution of the initial prior $\pi_0(\theta_C)$ and $\pi_H(\theta_C)$ as the prior to analyse current data:

$$w\pi_H(\theta_C) + (1 - w)\pi_0(\theta_C)$$

where $0 \leq w \leq 1$. It is shown that specifying a prior distribution of the weight w is equivalent to assigning w the expectation of that prior. Therefore, w can be prespecified with a value in [0, 1].

4.3. Application

The proposed application aims to use virtual patients, generated through the translational framework discussed earlier, as an external data source for generating SCAs in clinical trials. The process involves the following steps:

1. **Generation of virtual patients** The translational framework is used to create virtual patient treated with a specific drug, starting from TGI studies in PDX mice.
2. **External Data Integration** This virtual patient data is then used as an external data source for clinical trials, replacing the need for historical data.
3. **Application of Data Borrowing Techniques** The test-and-pool borrowing technique is employed to integrate the virtual patient data with the trial data to generate hybrid control arms.
4. **Case Study Application**: This approach has been tested in a case study to evaluate its effectiveness in a realistic setting.

4.3.1. Case study and data

The proposed application is tested using the case study of hepatocellular cancer treated with sorafenib. In this context, the sorafenib-treated group serves as the control arm for comparing various investigational treatments. Relevant clinical trials have been identified in the literature, specifically, three clinical trials (the FOHAIC-1 [157], SILIUS [156], and STAH [154] trials) were considered. In Table 4.1, some details of the analyzed studies are given. To derive clinical data, first PFS curves for both Sorafenib and

investigation arms were digitized. Then, TTE data on individual progression times were generated from the digitized curves using the approach outlined in the Supplementary Section, "*From digitized PFS to time-to-event data"*.

Table 4.1 Summary of the investigated hepatocellular cancer clinical trials.

Clinical trial	Investigational treatment studied	Number of patients in the Sorafenib arm	Number of patients in the investigational arm
FOHAIC -1	HAIC-FO (*)	132	130
SILIUS	HAIC + Sorafenib	103	102
STAH	cTACE + Sorafenib (**)	170	169

* HAIC-FO: hepatic arterial infusion chemotherapy + infusional fluorouracil, leucovorin, and oxaliplatin (FOLFOX) regimens, ** cTACE: conventional transarterial chemoembolization.

Since no precise information has been deduced about censoring, all the data has been treated as event data.

4.3.2. Testing environment

A hypothetical clinical trial is conducted to evaluate the impact of a given experimental drug for HCC cancer, with Sorafenib as the standard of care and reference. The primary endpoint of the study is PFS. The goal is to use the developed translational approach to generate virtual patients treated with Sorafenib, aiming to reduce the number of real patients needed for the control arm.

The trial protocol involves N_T patients receiving the investigational treatment ($\boldsymbol{Y_T}$), and N_C patients composing the hybrid control arm $\boldsymbol{Y_H}$. Specifically, $\boldsymbol{Y_T}$ data is derived from the digitized information of the three clinical studies listed in Table 4.1. $\boldsymbol{Y_H}$ consists of both real patients $\boldsymbol{Y'_C}$, and virtual patients $\boldsymbol{Y'_E}$. Here, $\boldsymbol{Y_C}$ included N_C real patient, with $\boldsymbol{Y'_C} \subseteq \boldsymbol{Y_C}$, while $\boldsymbol{Y_E}$ included $N_E = N_C$ virtual patient, with $\boldsymbol{Y'_E} \subseteq \boldsymbol{Y_E}$. $\boldsymbol{Y_C}$ are also sourced from the digitized data of the aforementioned studies, while $\boldsymbol{Y_E}$ consists of virtual patients generated using the translational approach.

Patients in the investigational arm $\boldsymbol{Y_T}$ are enrolled at the beginning of the trial. Instead, real patients in the control group are enrolled in cohorts, each consisting of n_c patients. Specifically, the control group is divided into 5 cohorts ($\boldsymbol{Y_C} = \bigcup_i^5 \boldsymbol{Y}_{C,i}$), each consisting of $n_c = \frac{N_C}{5}$ patients. Virtual patients are integrated according to the borrowing approach described below.

Of note, since the primary endpoint is PFS, all $\boldsymbol{Y_x}$ data will be understood as the pair time of event (T_{PFS}) and the event indicator (δ = 1 for each patient).

4.3.3. Dynamic borrowing strategy

Building on the test-and-pool method, a frequentist dynamic borrowing algorithm is applied in this scenario, as illustrated in the flowchart in Figure 4.1:

- **Step 0** At the outset, all the data from the experimental treatment arm are supposed to be available, while no real control patients have been already enrolled. Thus, the comparator arm, $\boldsymbol{Y_H}$, is initially composed entirely of virtual patients, i.e., $\boldsymbol{Y_{H,0} = Y_E}$.

- **Step i-th of control patient enrollment** At each enrollment stage i, a new cohort of n_c real control patients are enrolled in the study. Data from the real control patients, i.e., $\boldsymbol{Y_{C,i}} = \{Y_{C,1}, \dots, Y_{C,i \cdot n_c}\}$, and current comparator arm, $\boldsymbol{Y_{H,(i-1)}}$, are then compared.

    - A set of TTE parametric models (i.e., Lognormal, Log-logistic, Gompertz, Weibull, Exponential and Gamma) is fitted separately on $\boldsymbol{Y_{C,i}}$ and $\boldsymbol{Y_{H,(i-1)}}$. The best-performing models (i.e., the ones with the lowest AIC) are selected to describe data from the two groups ($\mathrm{S}_{\boldsymbol{C,i}}(t)$ and $\mathrm{S}_{\boldsymbol{H,(i-1)}}(t)$).

    - n_c virtual patients with the lowest likelihood of belonging to real patients progressing time distribution ($\boldsymbol{Y^{min}_{H,(i-1)}}$), i.e. those with the minimum $p\left(\boldsymbol{Y_{H,(i-1)}} \middle| \mathrm{S}_{\boldsymbol{C,i}}(t)\right)$, are discarded from $\boldsymbol{Y_{H,(i-1)}}$ (i.e. $\boldsymbol{Y'_{H,(i-1)} = Y_{H,(i-1)} - Y^{min}_{H,(i-1)}}$).

    - A new hybrid control arm is formed: $\boldsymbol{Y_{H,i} = Y_{C,i} \cup Y'_{H,(i-1)}}$ which consists of $N_H = N_T$ samples.

    - The maximum distance (D_{max}) between $\mathrm{S}_{C,i}$ and $\mathrm{S}_{H,(i-1)}$ is computed. If $D_{max} < D_{threshold}$, the algorithm stops and the hybrid control group $\boldsymbol{Y_{H,i}}$ is used as comparator arm for the study. Differently, the algorithm proceeds and triggers the inclusion of an additional cohort of real control patients in the clinical trial until the stop condition is met. To test the

algorithm, two $D_{threshold}$ has been used, a more conservative one (0.05) and a less conservative one (0.10).

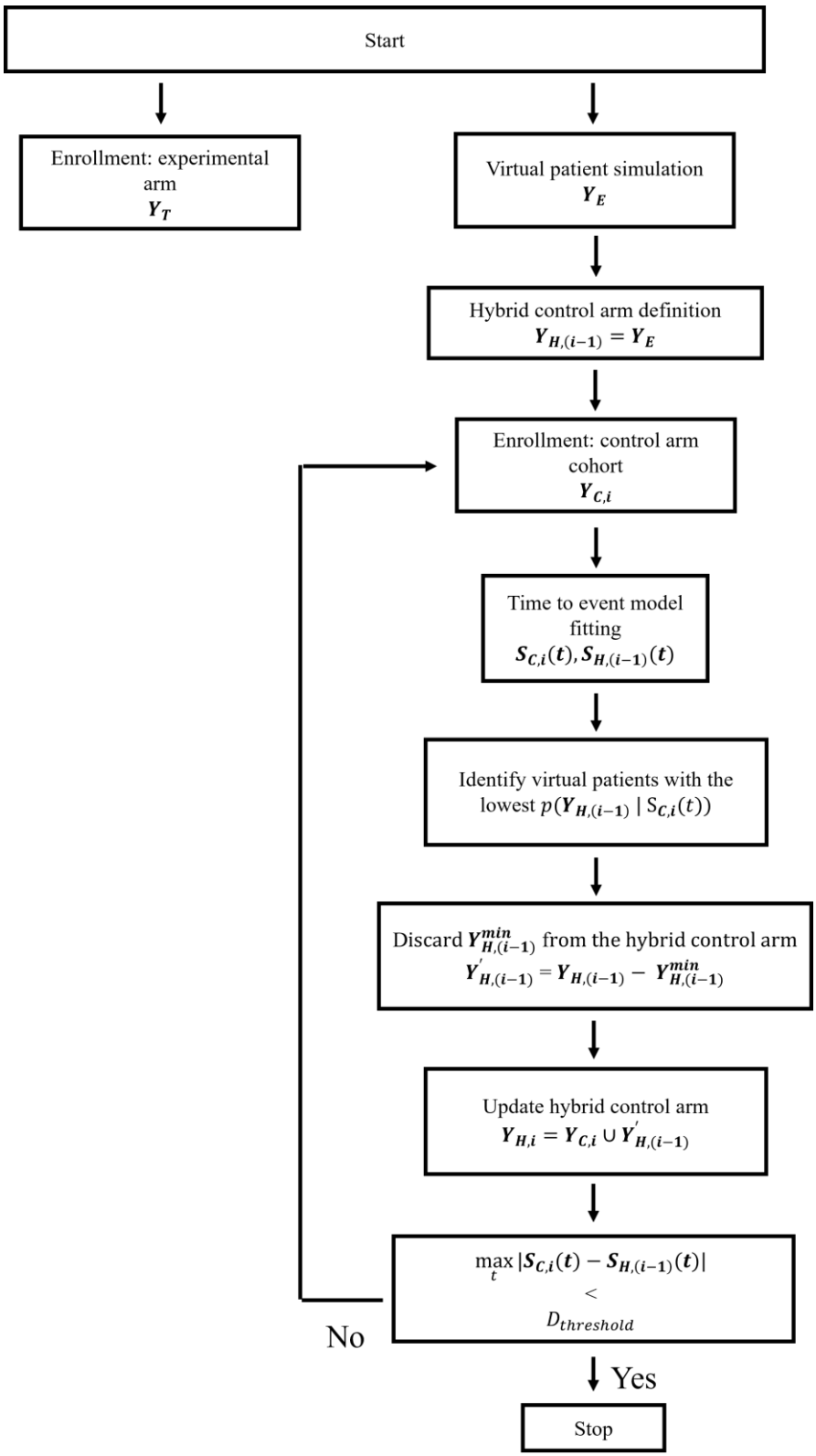

Figure 4.1 Flowchart of the implemented dynamic borrowing algorithm to build hybrid control arm.

4.3.4. Performance evaluation

The proposed algorithm was applied to the three clinical studies mentioned earlier. For each of these studies, the performance of the proposed algorithm is evaluated based on the number of real control patients that must be included in the hybrid control arm before the stopping criteria is met. Additionally, the hybrid control arm selected as competitor arm is compared to the investigational arm using the hazard ratio (HR) and log-rank test. Obtained results were compared to those obtained from the original control arm versus the investigational arm. Finally, a graphical comparison is conducted.

To account for the stochastic nature of $\boldsymbol{Y_E}$ generation and the cohort grouping of the observed control data, for each of the three clinical trials the procedure is repeated 500 times. KM-VPC curves for the hybrid control arm were generated following the strategy described in the Supplementary material B (*Predictive Intervals of KM curves).*

4.4. Results

4.4.1. Hybrid control arm diagnostics

First, the homogeneity of the generated hybrid control arm was assessed and the similarity between virtual and real control patients evaluated based on the number of cohorts included in the analysis.

In the most conservative scenario ($D_{max} < 0.05$), none of the 500 simulations for the FOHAIC-1 clinical trial resulted in a comparator arm composed entirely of real control patients, while only 4 out of 500 simulations did so for the STAH clinical trial. In contrast, 26.2% of the simulations for the SILIUS clinical trial produced a comparator arm composed entirely of real control patients. The median proportion of real patients included in the final $\boldsymbol{Y_H}$ was 40% for FOHAIC-1, 80% for SILIUS, and 60% for STAH.

In the less conservative scenario ($D_{max} < 0.10$), the inclusion of virtual control patients increased, resulting in fewer real patients enrolled in the trials. No simulations in this scenario produced a fully real comparator arm. Specifically, in the FOHAIC-1 trial, no iteration included more than 40% real control patients in the hybrid arm, with a median of just 20% real patients. In the SILIUS trial, the median number of included real control cohorts was 2, with only 1% of cases requiring 4 cohorts. Lastly, in the STAH trial, 96.1% of simulations included 1 or 2 cohorts.

The distribution of the number of patients included in the hybrid control arm for the two scenarios is depicted in Figure 4.2.

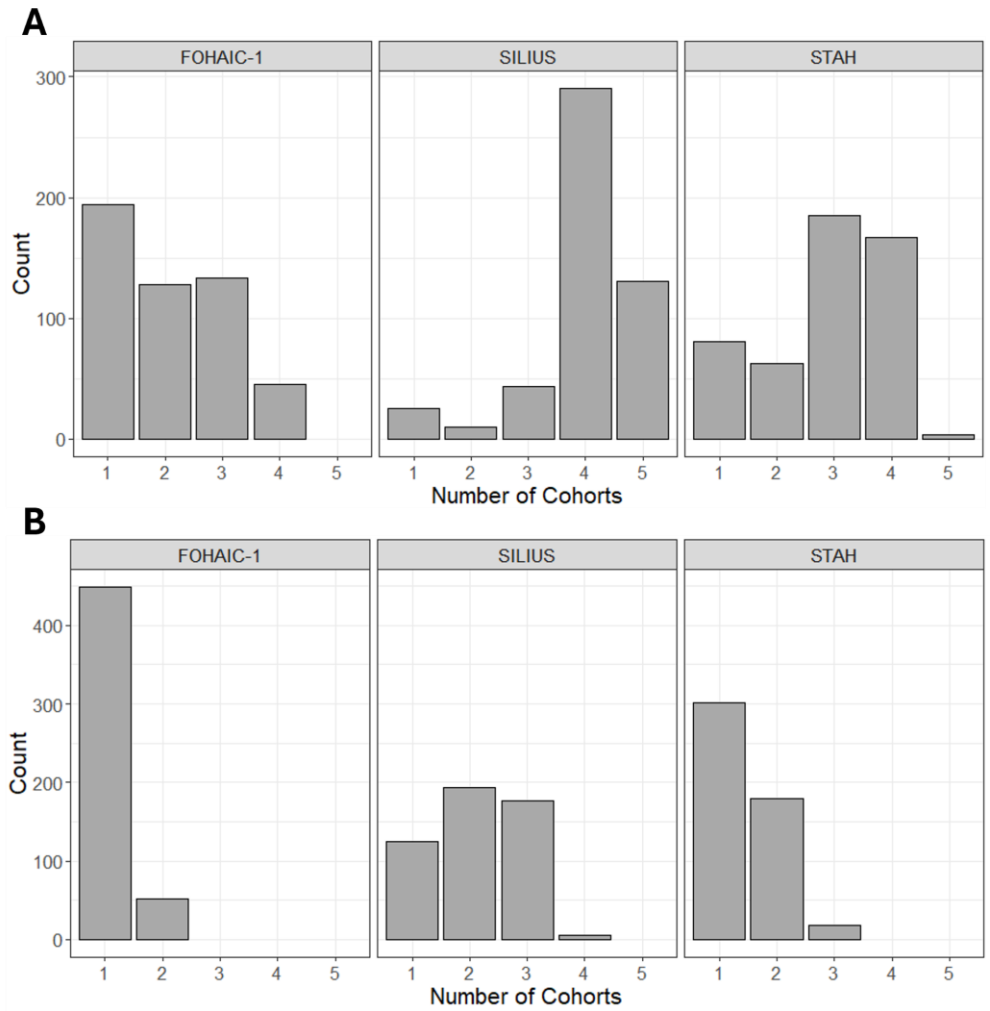

Figure 4.2 Bar plot showing the number of real patient cohorts included in the hybrid control arm. Panel A presents the results for the more conservative scenario (i.e., stricter stopping criteria, $D_{threshold} = 0.05$). Panel B presents the results for the less conservative scenario (i.e., more lenient stopping criteria, $D_{threshold} = 0.10$).

4.4.2. Hybrid control arm as comparator control arm

Second, the hybrid comparator arm, $\boldsymbol{Y_H}$, was compared with the experimental arm, $\boldsymbol{Y_H}$. For each clinical trial, the median of the 500 medians, along with the median of the 2.5th and 97.5th percentiles of the hazard ratios, was calculated. The results were then compared to those from the original comparator arm. Additionally, a bilateral log-rank test ($\alpha = 0.05$) was performed. The null hypothesis assumes that the two groups have identical hazard functions, $H_0: h_H(t) = h_T(t)$.

In the FOHAIC-1 clinical trial, with $D_{threshold} = 0.05$, the computed HR was 0.41 (95% CI: 0.31 – 0.53), closely matching the original HR of 0.45 (95% CI: 0.34 – 0.59). A similar outcome was observed when $D_{threshold} = 0.10$, with no substantial difference in HR (0.40, 95%CI: 0.31-0.52). The log-rank test rejected H_0 in 100% of the simulations, yielding a p-value below 0.002 for every simulated $\boldsymbol{Y_E}$ set for the $D_{threshold}$s values. This result aligns with the original analysis, which also resulted in a p-value smaller than 0.002.

In the SILIUS trial, with $D_{threshold} = 0.05$, the computed HR was 0.77 (95% CI: 0.58-1.03), closely matching the original HR also in this case (0.75, 95% CI: 0.57-1.00). A consistent result was observed with the less conservative threshold, where the computed HR was 0.72 (95% CI: 0.55-0.99). In the most conservative scenario, the log-rank test did not reject H_0 in 89.4% of cases, with a median p-value of 0.085, partially reflecting the original test results, where H_0 was not rejected with an associated p-value of 0.051. However, in the less conservative scenario, a greater difference was observed, with H_0 not rejected in only 59.6% of cases and a median p-value of 0.036.

For the STAH clinical trial, the results were consistent across both scenarios. The observed and original HR medians and 95% CIs closely matched ($D_{threshold} = 0.05$: 0.70, 95% CI: 0.56-0.87, $D_{threshold} = 0.10$: 0.66, 95% CI: 0.53-0.82, original STAH results: 0.73, 95% CI: 0.57-0.91). Similarly, the log-rank test rejected H_0 in 98.4% and 97.6% of simulations for $D_{threshold}$ = 0.05 and $D_{threshold}$ = 0.10, respectively. This is in line with the original analysis, which also rejected H_0 (p-value: 0.0086). A comprehensive comparison is then reported in Table 4.2.

Table 4.2 Comparison of the hybrid control arm versus the investigational arm, and the original control arm versus the investigational arm, in terms of HR and log-rank test results.

Clinical trial	**Group**	**Hazard Ratio (95% CI)**	**Log-rank test (1: H_0 is rejected, 0: H_0 is not rejected)**	**Log-rank test (p-value)**
FOHAIC-1	$D_{threshold}$ = 0.05	0.41 (0.31-0.53)	1 (100%)	< 0.002
	$D_{threshold}$ = 0.1	0.40 (0.31-0.52)	1 (100%)	< 0.002

Clinical trial	**Group**	**Hazard Ratio (95% CI)**	**Log-rank test (1: H_0 is rejected, 0: H_0 is not rejected)**	**Log-rank test (p-value)**
	Original	0.45 (0.34-0.59)	1	< 0.002
SILIUS	$D_{threshold}$ = 0.05	0.77 (0.58-1.03)	1 (10.6%) 0 (89.4%)	0.085
	$D_{threshold}$ = 0.1	0.72 (0.55-0.99)	1 (40.4%) 0 (59.6%)	0.036
	Original	0.75 (0.57-1.00)	0	0.051
STAH	$D_{threshold}$ = 0.05	0.70 (0.56-0.87)	1 (98.4%) 0 (1.6%)	< 0.002
	$D_{threshold}$ = 0.1	0.66 (0.53-0.82)	1 (97.6%) 0 (2.4%)	< 0.002
	Original	0.73 (0.57-0.91)	1	0.0086

For each clinical trial, the 500 simulated PFS curves in the control group were summarized by their median PFS profiles and their prediction intervals. As shown in Figure 4.3, PFS curves from the original control arm and the hybrid control arm closely match, with a notable overlap along the entire profile. This holds true for both thresholds ($D_{threshold} = 0.05$ in the first row, $D_{threshold} = 0.10$ in the second row) used as stopping criteria.

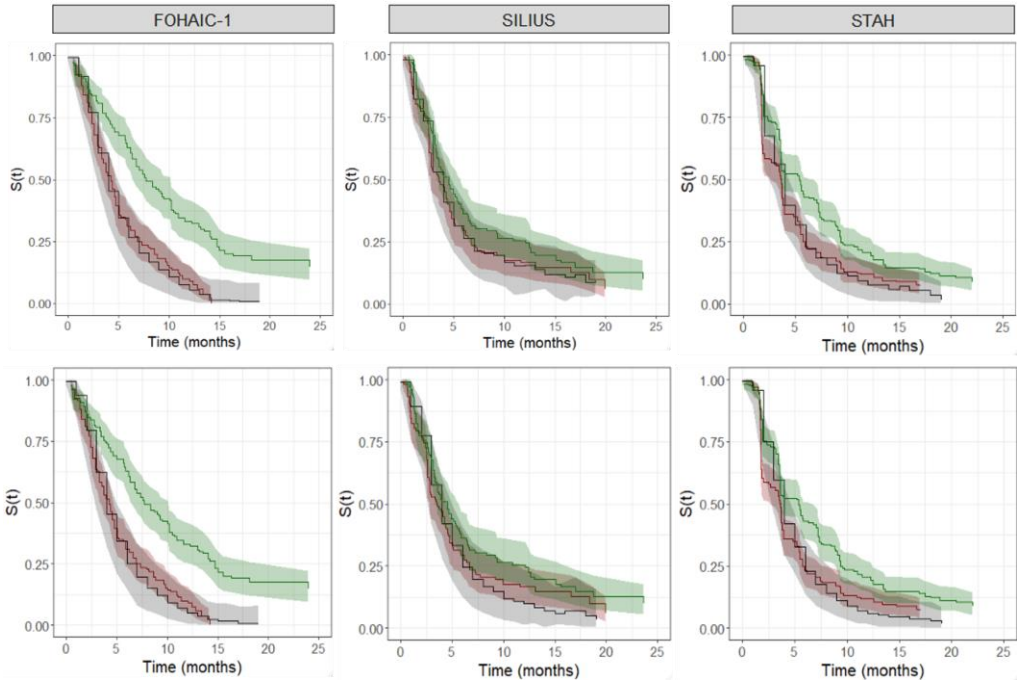

Figure 4.3 Median PFS profiles and prediction intervals for 500 simulated PFS curves. The green solid line represents the observed PFS for the investigational arm, with the shaded area indicating the 95% CI. In red, the original control arm while the hybrid control arm is shown in gray. The first row displays results for $D_{threshold}$ = 0.05, while the second row shows results for $D_{threshold}$ = 0.10.

4.5. Wrap up and future developments

This chapter presents the first proposed real-world application of the developed translational framework. The findings of this study demonstrate the potential of using hybrid control arms, composed of both real and PDX-generated virtual patients, to address the challenges posed by low enrollment in cancer clinical trials. The study explores the use of Control groups composed of PDX-generated virtual patients as an alternative to control groups composed of external patients derived from historical data/literature. Indeed, a BCG report [184] identified two main barriers limiting the adoption of external control arms in clinical practice. The first is the lack of historical data, stemming from both the actual absence of data and the reluctance of many pharmaceutical companies to share their data with other organizations. The second barrier is the lack of standardization across data sources. The approach proposed in this thesis for generating virtual patients could offer a solution to these limitations.

The results across three clinical trials (FOHAIC-1, SILIUS, and STAH) indicate that the proposed translational framework effectively integrates

virtual patients into control arms, providing comparable results to traditional methods while reducing the number of real patients required, at least in the case study under analysis.

One of the significant strengths of this approach is the close alignment between the hybrid control arms and the original control arms across all trials. The computed hazard ratios and log-rank tests consistently showed that the hybrid arms closely mirrored the outcomes of the original control groups. This similarity was particularly evident in the FOHAIC-1 and STAH trials, where the hybrid arm performed almost identically to the original control arm, with minimal deviations in HR and p-values (Table 4.2). In the SILIUS trial, while the hybrid arm performance was slightly more variable, the results remained within an acceptable range, especially in the more conservative scenario. The ability to achieve such alignment with the original control arms suggests that the virtual patient model used here captures the essential characteristics of the real patients in the control arms, at least within the constraints of PFS as the primary endpoint.

Despite these promising results, several limitations must be acknowledged. First, the study, due to translational constraints, focused solely on PFS as the primary endpoint. While PFS is a critical outcome in oncology trials, it does not capture other important aspects of treatment efficacy, such as OS, quality of life, or long-term treatment benefits. Second, the framework was validated using a single case study involving hepatocellular carcinoma treated with sorafenib. Although the results across the three clinical trials were encouraging, the generalizability of these findings to other cancer types and treatment regimens remains uncertain and additional case studies in different cancer settings are needed to confirm the broad applicability of the proposed method. Third, virtual patients were generated without accounting for individual patient characteristics, such as genetic profiles, comorbidities, or treatment histories. This lack of personalization could limit the accuracy of the virtual patients in reflecting the diversity of real-world populations. Incorporating patient-specific covariates in the translational framework, particularly genetic data, could enhance the realism of virtual patients and improve the reliability of hybrid control arms. Lastly, the study employed a single dynamic borrowing method based on the test-and-pool approach. While this method was effective in balancing the hybrid arms with the investigational arms, it may not be the optimal approach in all cases. Aware of the limitations, but strengthened by the success of this initial study, avenues for future research and development can be thought of. Future developments are oriented in two different but complementary directions, one involving the improvement and exploration of different dynamic borrowing techniques, and one the refinement and extension of the translational approach. Regarding the first one, future studies should explore different dynamic borrowing techniques, including Bayesian approaches like

the calibrated power prior and robust mixture prior. These methods may offer improved flexibility in balancing real and virtual patient data and could provide better control over the degree of borrowing based on the similarity between external and current data.

Chapter 5

Enhancing nonlinear joint modeling for tumor kinetics and survival through Bayesian integration of preclinical insights

In this chapter, we enhance nonlinear joint modeling techniques by integrating preclinical insights through Bayesian methods.
The goal is to improve the accuracy of joint models for longitudinal and TTE data in oncology using preclinical-derived prior information. Section 5.1 introduces the concept of joint models for these data types and contextualize nonlinear joint models and Bayesian inference. Section 5.2 describes the aim of the study, and the case study used to test the proposed approach. Section 5.3 outlines the mathematical model structures used in this study. We start by discussing the clinical longitudinal model, baseline TTE models, and association functions evaluated. Section 5.4 details the prior distribution used for this application and the analysis performed. We explain how preclinical information is translated into clinical contexts and describe the methods used to evaluate model performance and the impact of prior information on posterior estimates. Section 5.5 described how models are assessed. Finally, Section 5.6 presents the analysis results, and Section 5.7 wraps up with a discussion of the strengths and weaknesses of the approach.

5.1. Joint models for longitudinal and TTE data in oncology

Joint modeling of longitudinal and TTE data is a growing area of research that enables the simultaneous analysis of repeated measurements and survival outcomes. This approach involves two connected sub-models, a longitudinal model and a TTE model, which are linked through an association structure quantifying the relationship between the outcomes of interest [185].

In the context of advanced cancer, joint models have been developed to describe the relationship between the dynamics of some biomarkers, such as tumor size, and TTE outcomes, like survival. These models are particularly valuable because they increase the understanding of relation between changes in biomarkers over time and patient outcomes. By linking longitudinal tumor measurements with survival data, joint models can improve patient monitoring and inform decision-making in clinical trials [186, 187].

Historically, most joint models were designed with linear components in the longitudinal part to simplify calculations [188–190]. Linear models assume that changes in biomarkers over time follow a straight line or constant rate. This assumption simplifies computations but may not capture the true complexity of tumor growth and treatment response. To overcome these limitations, recent research has shifted towards developing nonlinear joint models. Nonlinear models can accommodate more complex patterns in tumor progression, such as exponential growth or decay, providing a more accurate and nuanced understanding of how treatments affect tumors and survival outcomes. The development of these models in specialized software tools, like Monolix and NONMEM, has facilitated their wider adoption within the statistical community [191, 192].

Most of the literature on joint models in oncology has used SLD as a biomarker, calculated according to RECIST criteria [193, 194]. However, in advanced cancer patients, where multiple target lesions may be present in different organs, using SLD significantly reduces the available information by combining all measured lesions into a single value.

Over the past decade, semi-mechanistic nonlinear joint models have gained attention for their ability to better characterize the response to cancer treatments. These models incorporate biological mechanisms into the statistical framework, offering parameters that have direct biological interpretations, such as growth rates or drug efficacy levels. By doing so, they help to understand not only the statistical relationship between tumor kinetics and survival but also the underlying biological processes driving

these outcomes. In this context, a significant area of research that has advanced the field involves joint models that account for the dynamics of individual lesions dynamics and link them with patient survival [195, 196].

5.1.1. Nonlinear joint models and Bayesian inference

The nonlinear nature of these models makes the calculation of the likelihood function and the estimation of the model parameters more difficult. These tasks become even more challenging when the model focuses on tumor dynamics at the individual lesion level. Bayesian inference offers a useful way to include prior information and manage uncertainty more effectively. In studies by Kerioui et al. [191, 195] ,the HMC-NUTS algorithm in Stan software was used for the SLD, OS, and lesion-level models. However, these studies only partially used Bayesian methods, relying on non-informative priors due to a lack of information. This limited the full potential of the Bayesian approach. Kerioui et al. [191] also showed that using non-informative or weakly informative priors can lead to inaccurate parameter estimates, highlighting the need for better prior characterization.

5.2. Aim and case study

The purpose of this application is to assess the developed translational approach as a tool to derive informative prior from preclinical PDX studies to inform the estimation of joint models for individual tumor lesions and OS in advanced oncology trials. To evaluate this application, the same case study used in the previous application, i.e., the HCC cancer treated with Sorafenib with PDX TGI model already analyzed and results presented in Section 3, was considered.

5.2.1. Clinical data

On December 1, 2022, data from the control arm of the Phase 3 clinical trial NCT00699374 were accessed through the online database Project Data Sphere [197]. NCT00699374 was an international, Phase 3, randomized, open-label study designed to compare the efficacy of Sunitinib malate versus Sorafenib in the treatment of advanced hepatocellular carcinoma. The control arm, which involved 544 patients diagnosed with inoperable liver cancer, received 400 mg of Sorafenib twice daily as specified by the study protocol.
The dataset included longitudinal measurements of individual lesion diameters for each patient, along with TTE data such as drop-out or death.

Tumor locations were recorded in various sites, including the liver, lungs, lymph nodes, adrenal glands, and peritoneum. Additionally, the data allowed for the derivation of each patient's specific administration schedule, including any dose adjustments based on changes in the patient's clinical condition. No specific PK data was available.
Data management and cleaning procedures were then applied to the dataset, with detailed documentation available in the supplementary section *Data management of NCT00699374 clinical trial* of Appendix D.

5.3. Joint model for longitudinal tumor measurements and OS data

The observations of individual lesion diameters in various organs were modeled using a non-linear mixed effect approach to better understand the distribution and characteristics of these lesions across different tissues.

5.3.1. Structure of the clinical TGI model

The Claret TGI model describing tumor volume dynamics, presented in Eq. 6, was considered. However, since the dataset under analysis provides tumor measurements in diameters rather than volumes, it was reformulated in terms of tumor diameter as detailed in the Supplementary material *Adapting the volumetric TGI model to describe tumor diameter data*:

$$\frac{dTS(t)}{dt} = \left(k'_{g,human} - k'_{d,human} \cdot c(t)\right) \cdot TS(t) \qquad (7)$$

where $TS(t)$ represents tumor diameter dynamics, $k'_{g,human} = {k_{g,human}}/{3}$ is the exponential tumor diameter growth rate and $k'_{d,human} = {k_{d,human}}/{3}$ the drug potency. Since no PK information was available, as already done in chapter 3, we used the two-compartment PK model developed by Choi et al. [158] to simulate individual Sorafenib concentration profiles, $c(t)$.

5.3.2. Nonlinear mixed-effect model

The following formalization of the nonlinear mixed-effects (NLME) model is adopted here.

Let $y_{i,j,k,l}$ represents the l^{th} measurement of the k^{th} target lesion in organ j for subject i. Let $K_{i,j}$ denotes the number of target lesions monitored over time in organ j of patient i, and let $K_i = \sum_{j=1}^{5} K_{i,j}$ be the total number of target lesions for patient i (up to 5, according to RECIST 1.1). Let L_i be the total number of organs affected by tumor for patient i. The NLME is described by:

$$y_{i,j,k,l} = TS\left(t_{i,j,k,l}, \boldsymbol{\psi_{i,j,k}}\right) + \left(\sigma_1 \cdot \nu_{i,j,k,l} + \sigma_2 \cdot \epsilon_{i,j,k,l} \cdot TS\left(t_{i,j,k,l}, \boldsymbol{\psi_{i,j,k}}\right)\right) \quad (8)$$

where:

- the first term, $TS\left(t_{i,j,k,l}, \boldsymbol{\psi_{i,j,k}}\right)$ is the structural model function at time $t_{i,j,k,l}$ with $\boldsymbol{\psi_{i,j,k}}$ the individual parameter vector for lesion k in organ j of patient i;
- the second term is a combined residual error model with $\nu_{i,j,k,l} \sim \mathcal{N}(0,1)$ and $\epsilon_{i,j,k,l} \sim \mathcal{N}(0,1)$ the standard Gaussian error terms. σ_1 and σ_2 are the additive and multiplicative components of the error term.

The individual parameters $\boldsymbol{\psi_{i,j,k}}$ are assumed to follow a log-normal distribution:

$$log\left(\boldsymbol{\psi_{i,j,k}}\right) = log(\boldsymbol{\theta}) + \boldsymbol{\xi_j} + g(\boldsymbol{\eta_i}) + \boldsymbol{\rho_{i,j,k}} \quad (9)$$

where:

- $\boldsymbol{\theta}$ is the vector of fixed-effect parameters;
- $\boldsymbol{\xi_j}$ is the fixed effect specific to organ j. To ensure identifiability of the parameters, the fixed organ-specific effect for the primary lesion was fixed to zero ($\boldsymbol{\xi_1}$=0);
- $g(\boldsymbol{\eta_i})$ represents subject-specific random effects. The g function is the identify function for all parameters except the initial tumor size TS_0, where g is a Box-Cox transformation characterized by the parameter λ [198];
- $\boldsymbol{\rho_{i,j,k}}$ captures the lesion-specific random effects.

Thus, for each biological parameter, i.e., each component of the vector $\boldsymbol{\psi_{i,j,k}}$, we assume that there are two random effects. The first one is specific to subject i: $\boldsymbol{\eta_i} \sim \mathcal{N}(0, \boldsymbol{\Omega_1})$ and $\boldsymbol{\Omega_1}$ diagonal matrix of standard deviations, in which each diagonal component corresponds to the inter-individual variability of the biological parameters. The second random effect is the lesion effect: $\boldsymbol{\rho_{i,j,k}} \sim \mathcal{N}(0, \boldsymbol{\Omega_2})$ and $\boldsymbol{\Omega_2}$ diagonal matrix of standard

deviations, with its diagonal components corresponding to the inter-lesion variability of the biological parameters. We assume independence between the two random effect sources.

5.3.3. TTE model for OS data

Let (T_i, δ_i) denote the vector of survival data for subject i, with T_i being the time to event for subject i, corresponding to the minimum between the time of death X_i and time of censoring C_i, and δ_i the death indicator. The individual hazard function $h_i(t)$ describing the survival data of subject i is given by:

$$h_i(t|\boldsymbol{\phi}, \boldsymbol{\beta}, \boldsymbol{\psi_i}) = h_0(t \cdot \alpha(\boldsymbol{\beta}, \boldsymbol{\psi_i})|\boldsymbol{\phi}) \times \alpha(\boldsymbol{\beta}, \boldsymbol{\psi_i}) \quad (10)$$

where:

- $h_0(t \cdot \alpha|\boldsymbol{\phi})$ represents a parametric baseline hazard function characterized by the vector of parameters $\boldsymbol{\phi}$;
- $\alpha(\boldsymbol{\beta}, \boldsymbol{\psi_i}) = exp\big(\boldsymbol{\beta} \times f(\boldsymbol{\psi_i}, t)\big)$ with $\boldsymbol{\beta}$ the vector of the associations between the longitudinal biomarker and the survival process, and $\boldsymbol{f}(\boldsymbol{\psi_i}, t)$ the vector of link functions, which depends on the vector of individual parameters specific to subject i, $\boldsymbol{\psi_i} = \big(\boldsymbol{\psi_{i,j,k}}\big)_{j\in\{1,\dots,L_i\},\, k\in\{1,\dots,K_{i,j}\}}$, and could be also a function of time.

Baseline hazard models

Investigation of the baseline OS hazard model involved a comparison of exponential, log-logistic, log-normal, gamma, generalized gamma, Gompertz, and Weibull distribution models. The same range of models was also used to examine the censoring process.

Association between tumor size and survival

Different association structures between the individual lesions and the instantaneous risk of death were considered. They can be divided into two groups, finite-time association structure, where $\boldsymbol{f} = \boldsymbol{f}(\boldsymbol{\psi}_i)$, and continuous-time association structure, where $\boldsymbol{f} = \boldsymbol{f}(\boldsymbol{\psi}_i, t)$. Two selected association structures, one per group, are described here, while further tested alternatives are described in the *Alternative association structure* section of the supplementary material for this chapter.

The finite-time link function assumes that: i) the lesion in each organ with the highest C_t value, and ii) the sum of the baseline tumor diameters,

stratified by organ, influence patient survival. The following equation characterizes this relationship:

$$\boldsymbol{\beta} \times f(\boldsymbol{\psi_i}) = \sum_{j=1}^{L_i} \left(\beta_{C_t,j} \times \max_k \left(C_{t,i,j,k}\right)^{\gamma}\right) + \sum_{j=1}^{4} \left(\beta_{TS_0,j} \times \sum_{k=1}^{K_{i,j}} TS_{0,i,j,k}\right) \quad (11)$$

where $C_{t,i,j,k} = \frac{k'_{g,i,j,k}}{k'_{d,i,j,k}}$ represents the concentration at steady state that, if exceed, enables lesion remission in patient i, organ j, lesion k.
The continuous-time link function considers that the sum of diameters, stratified by organ, impacts patient survival with different parameters for each organ:

$$\boldsymbol{\beta} \times f(\boldsymbol{\psi_i}, t) = \sum_{j=1}^{L_i} \left(\beta_{TS,j} \times log\left(\sum_{k=1}^{K_{i,j}} TS_{i,j,k}(t)\right)\right). \quad (12)$$

5.4. Prior definition and analysis

The prior distributions for $\theta_{k'_g}$ and $\theta_{k'_d}$, as well as for ω_{1,k'_g} and ω_{1,k'_d}, are derived using the translational approach outlined in chapter 3. Of note, since the volumetric parameters k_g and k_d, follow a lognormal distribution, their corresponding population values θ_{k_g} and θ_{k_d} were divided by 3 to adjust for tumor diameter dynamics ($\theta_{k'_g} = {}^{\theta_{k_g}}/_3$ and $\theta_{k'_d} = {}^{\theta_{k_d}}/_3$), while $\omega_{1,k'_g} = \omega_{1,k_g}$ and $\omega_{1,k'_d} = \omega_{1,k_d}$ (Supplementary section *Adapting the volumetric TGI model to describe tumor diameter data*). We decided to use a highly informative prior for tumor growth rate $\theta_{k'_g}$, an informative prior for drug effect $\theta_{k'_d}$, and a weakly informative prior for the inter-individual variability ω_{1,k'_g} and ω_{1,k'_d}. Specifically, from the estimated PDX parameters (Table 3.3), via Eq. 13, we derived the following prior distributions:

- $\theta_{k'_g} \sim Lognormal(2.3e-2, 0.1)$
- $\theta_{k'_d} \sim Lognormal(1.1e-4, 0.3)$
- $\omega_{1,k'_g} \sim Normal(5.4e-1, 0.5)$
- $\omega_{1,k'_d} \sim Normal(6.3e-1, 0.5)$

We set informative prior distribution for the remaining fixed-effect parameter $\theta_{TS_0} \sim LN(40, 0.5)$. All the rest of random effects standard

deviation priors were half-normal distributions. As it reasonable, from a biological point of view, to assume that the greater source of variability comes from the patient level, we chose $N \sim (1,1)$ for diagonal terms of Ω_1 (if different value not specified) and $N \sim (0.8, 0.8)$ for diagonal terms of Ω_2. $\lambda \sim N(-0.5,0.5)$ based on the observed left-skewed distribution of tumor size at the baseline. Other prior distributions were weakly informative, that is $\xi \sim N(0, I)$, with I the identity matrix. All the components of the link parameter vector β follow $N(0,1)$, $\gamma \sim Beta(2,2)$. We chose lognormal distribution for the error terms $\sigma_1 \sim LN(2,2)$ and $\sigma_2 \sim LN(0.1,2)$ to ensure a smooth positive constraint.

5.4.1. Prior sensitivity analysis

We performed a prior sensitivity analysis to test the robustness of our results and to evaluate the influence of PDX-derived priors. We selected two alternative models for the PDX-informed parameters. First, we compared a model using PDX-informative (PI) priors against one using literature-informed (LI) priors. In particular, information from [199] where used to specify prior for $\theta_{k_g'} \sim LN(0.0019,0.1)$. For k_d', as well as for and $\omega_{k_g'}$, due to a lack of specific information, we applied a weakly/uninformative prior: $\theta_{k_d'} \sim \Gamma(1,100)$, $\omega_{k_g'} \sim N(1,1)$, $\omega_{k_d'} \sim N(1,1)$.
Second, we compared the PI model against a model employing weakly/uninformative (UI) priors, where both $\theta_{k_g'}$ and $\theta_{k_d'}$ were assigned $\Gamma(1,100)$ priors, and random effects were modeled with half-normal $N(1,1)$ as the others random effects.

We adopt the framework described in [200] to present the results of the prior sensitivity analysis. Specifically, we compare alternative prior models by evaluating model convergence and the impact of prior variations on the posterior distributions of the parameters. Runtime was also considered.

5.4.2. Phase II trial emulation

In this retrospective analysis, we aimed to further emphasize how different prior sources (i.e., the PI, LI, and UI models) influence model outcomes through emulation of Phase II studies.
By adopting an approach inspired by Bruno et al. [60], we resampled data from the NCT00699374 Phase III HCC trial to simulate 100 distinct Phase II trials, each composed by 40 patients. For each simulated Phase II trial, we estimated the best joint model, which had been selected from the complete Phase III dataset. We ran four chains, each with 1000 warm-up iterations and

1000 sampling iterations, for each model with a different prior structure. We then compared the results by examining convergence, the consistency of parameter estimates, and the association functions included in the final models, evaluating these aspects across the simulated trials.
To evaluate convergence, we applied four criteria to determine whether each model run (i.e., one estimated for each simulated trial) had converged or not: i) R_{hat} < 1.05, ii) R_{hat} < 1.02, iii) ESS > 100, iv) ESS < 400 for each parameter [201]. For parameter consistency, we compared the distribution of the posterior median values from the Phase II simulations with the nominal median values from the full Phase III trial. Finally, we counted how many of the simulated Phase II trials produced a 95%CI for the $\boldsymbol{\beta}$ parameters that did not include zero.

5.5. Model assessment

This section provides details about how model is estimated using Bayesian inference, statistical criteria for the comparison of different model structures and different association functions that links longitudinal dynamics to patients' survival.

5.5.1. Model estimation

Conditional on all parameters, we assume independence among all longitudinal measurements of a single patient, as well as independence between the longitudinal and survival data of the same patient. Of note, lesion measurements below the quantification limit are treated as left-censored in the longitudinal density (see Supplementary Material *Accounting for the limit of quantification for more details*).

The likelihood was maximized using the Hamiltonian Monte Carlo (HMC) algorithm implemented in Stan via the R package *cmdstanr* (version 0.6.1.9000). For the longitudinal sub-model, we ran 4 chains with 1000 iterations each (500 warm-up and 500 sampling). For the baseline survival models, we also used 4 chains with 1000 iterations per chain (500 warm-up and 500 sampling). In the joint models, we ran 4 chains in parallel with 2000 iterations each, including 1000 warm-up iterations, resulting in a total of S = 4000 posterior samples. Convergence was assessed through Markov Chain Monte Carlo (MCMC) trace plots, inter-chain autocorrelation, and additional Stan diagnostic tools such as R_{hat} and effective sample sizes (ESS), were also used. To expedite Stan model execution, a within-chain parallelization routine was employed.

5.5.2. Statistical criteria for model comparison

The Bayesian criteria used for model comparison included the Watanabe-Akaike Information Criterion (WAIC) and the Leave-One-Out Information Criterion (LOOIC).
We defined WAIC as follows:

$$WAIC = -2 \times \sum_{i=1}^{N} \left(\log \left(\frac{1}{S} \sum_{s=1}^{S} L(y_i, T_i, \delta_i \mid \boldsymbol{\chi^s}, \psi_i^s) \right) \right) + 2 \times p_{\text{WAIC}}$$

$$p_{WAIC} = \sum_{i=1}^{N} \mathrm{V}_{s=1}^{S} \left(L(y_i, T_i, \delta_i \mid \boldsymbol{\chi}^s, \psi_i^s) \right)$$

where $\boldsymbol{y_i}$ denote the vector of all lesion measurements of patient i, $\chi = \{\boldsymbol{\phi}, \boldsymbol{\beta}, \boldsymbol{\theta}, \boldsymbol{\xi}, \boldsymbol{\Omega_1}, \boldsymbol{\Omega_2}, \sigma_1, \sigma_2\}$ the vector of population parameters, $L(y_i, T_i, \delta_i \mid \chi, \psi_i)$ the individual patient likelihood and $V_{(s=1)}^{S}$ the sample variance. S represents the number of posterior replicates.

Similarly, we defined LOOIC as:

$$LOOIC = -2 \times \sum_{i=1}^{N} \log \left(\frac{\sum_{s=1}^{S} w_i^s L(\boldsymbol{y_i}, T_i, \delta_i \mid \boldsymbol{\chi^s}, \boldsymbol{\psi_i^s})}{\sum_{s=1}^{S} w_i^s} \right)$$

where w_i^s are the truncated importance sampling weights [202].

5.5.3. Model selection and evaluation

The model in Eq. 7 was identified on longitudinal tumor measurements to evaluate its ability to accurately describe the data or the need of model adjustments.
Subsequently, survival data were modeled independently, and different baseline hazard models were compared. The model yielding the lowest WAIC/LOOIC values was selected to describe the baseline hazard process. The same procedure was applied to model the censoring process.
After finalizing the longitudinal structural model and baseline hazard model, we constructed the joint model. Several joint models, each utilizing different association structures, were fitted to the complete dataset. The model with the lowest WAIC/LOOIC was selected as the final model.
Posterior predictive checks (PPCs) were plotted to visually assess the model ability to replicate the original dataset (details provided in the Supplementary section *Posterior Predictive Checks*).

5.5.4. Association magnitude quantification

If ending up with the finite-time association function, a strategy was implemented to quantify the magnitude of different factors $f \in F$, where $F = F_{C_t} \cup F_{TS_0}$ with $F_{C_t} = \{\max_k(C_{t,i,j,k})^\gamma \mid j = 1, \dots, L_i\}$ and $F_{TS_0} = \left\{\sum_{k=1}^{K_{i,j}} TS_{0,i,j,k} \middle| \; j = , \dots, N_i\right\}$. This approach allows for a direct comparison of their impacts on patient survival. The effect of each factor was quantified as:

$$E_f^s = \log_2\left(\frac{(S^s)^{-1}\left(0.5\middle|\boldsymbol{\phi^s}, F_f^{-1}(0.975), F_{F_{-f}}^{-1}(0.5), \boldsymbol{\beta^s}\right)}{(S^s)^{-1}\left(0.5\middle|\boldsymbol{\phi^s}, F_f^{-1}(0.025), F_{F_{-f}}^{-1}(0.5), \boldsymbol{\beta^s}\right)}\right)$$

where $\boldsymbol{\beta^s}$ and $\boldsymbol{\phi^s}$ represents the s^{th} posterior replicate of parameter vector $\boldsymbol{\beta}$ and $\boldsymbol{\phi}$, respectively. F_{-f} denotes the set of factors excluding f and $F^{-1}(x)$ the inverse of the cumulative distribution computed in x. The $\log_2$ transformation helps make the effects symmetric around zero and easier to interpret. Factors were then ranked based on the median E_f values.
Additionally, to assess the overall impact of F_{C_t} and F_{TS_0}, the model was re-estimated including only a subset of these factors (i.e., F_{C_t} or F_{TS_0}) in the survival function. The performance of the model with these subsets was compared using the WAIC and LOOIC to determine how much model performance deteriorated when excluding certain factors.

5.6. Results

5.6.1. Data

128/544 patients were excluded from the analysis. A total of 923 individual target lesions were monitored over time, including 518 in the liver, 209 in the lung, 127 in the lymph nodes and 69 in other locations. Table 5.1 details the characteristics of these patients, summarizing the findings.

Table 5.1 Characteristics of the data used.

	Sorafenib group (N=416)
Mean age, years (STD)	56.5 (12.8)
Median age, years (IQR)	56 (48 – 66)
Sex	
Men	352 (84.6%)
Women	64 (15.4 %)
Number of target Lesions	

	Sorafenib group (N=416)
1	118 (28.4%)
2	176 (42.3%)
3	61 (14.7%)
4	41 (9.9%)
5	21 (5.0%)
Location	
Liver	518 (59.4%)
Lung	209 (23.2%)
Lymph node	127 (11.9%)
Other	69 (5.4%)

To relate to the previously introduced model formulation, the following index-organ map was used: j = 1: liver, j = 2: lung, j = 3: lymph node, j = 4: other.

5.6.2. Longitudinal model tuning

An analysis of the residuals revealed a trend during the later stages of tumor growth (more details in *Effects of drug resistance on longitudinal model performance* section in Appendix D). This trend was attributed to the model inability to account for resistance mechanisms. Consequently, the model was updated to include a decrease in drug effectiveness proportional to drug exposure.

$$\frac{dTS(t)}{dt} = \left(k'_g - k'_d e^{-R \cdot AUC_{0-t}} \cdot c(t)\right) \cdot TS(t) \qquad (13)$$

where R is the resistance parameter and AUC_{0-t} the cumulative exposure from $t = 0$ to t. A non-informative prior distribution was assigned to R, specifically following a gamma distribution, $\Gamma(1{,}100)$.

5.6.3. Baseline TTE submodel investigation

We selected the lognormal model for describing OS data and the Gompertz model for the censoring process, based on WAIC model ranking (Table 5.2).

Table 5.2 Baseline TTE model fitting.

Distribution	OS		Censoring	
	WAIC	Rank	WAIC	Rank
Gamma	4311.	4	1637.	5
Generalized gamma	4293.	3	1570.	2

Distribution	OS		Censoring	
	WAIC	Rank	WAIC	Rank
Gompertz	4334.	7	1542.	**1**
Exponential	4333.	6	1721.	6
Loglogistic	4293.	2	1633.	4
Lognormal	4291.	**1**	1721.	7
Weibull	4319.	5	1598.	3

Lognormal survival model is described as

$$S(t|\mu,\sigma) = 1 - \int_0^t \frac{1}{x\sigma\sqrt{2\pi}} \exp\left[-\frac{(logx-\mu)^2}{2\sigma^2}\right] dx.$$

A weakly-informative prior distribution was assigned to μ and σ : $\mu \sim LN(5,1)$ and $\sigma \sim LN(1,1)$.

Conversely, the censoring model was specifically developed to facilitate the replication of this process during the PPCs generation phase. Consequently, the results of this model are detailed in the supplementary section, where the process is explained.

5.6.4. Association between tumor size and survival

Values of WAIC and LOOIC criteria for each candidate model are reported in the following table.

Table 5.2 Comparison between the best finite-time and the best continuous-time association functions.

Association function	WAIC	LOOIC
Finite-time (Eq.11)	31459.1	32083.8
Continuous-time (Eq. 12)	34385.2	33199.1

As results were consistent across different finite-time candidate models (See *Alternative association structures* in Appendix D) and the association structure presented in Eq. 13 provided the best fit to the data, we mainly focus on the latter model in this and the following section.

5.6.5. Inter-lesions variability

In Table 5.3 model estimates (i.e, posterior median), along with their coefficient of variation (i.e. posterior standard deviation divided by posterior median) and the 95% posterior credibility interval (95%CI) are reported.

Table 5.3 Parameter estimated values.

Parameter	Median	CV (%)	95%CI
μ	6.8e+0	1.6e+0	[6.6e+0, 7.0e+0]
σ	7.2e-1	5.9e+0	[6.5e-1, 8.1e-1]
γ	3.7e-1	1.4e+1	[2.8e-1, 4.8e-1]
$\beta_{C_{t,1}}$	-1.5e-1	3.1e+1	[-2.6e-1, -7.3e-2]
$\beta_{C_{t,2}}$	-2.6e-1	3.0e+1	[-4.3e-1, -1.3e-1]
$\beta_{C_{t,3}}$	-3.7e-2	1.4e+2	[-1.6e-1, 5.3e-2]
$\beta_{C_{t,4}}$	2.9e-2	2.6e+2	[-1.2e-1, 1.9e-1]
$\beta_{TS_{0,1}}$	-4.3e-3	1.4e+1	[-5.4e-3, -3.0e-3]
$\beta_{TS_{0,2}}$	1.3e-4	1.7e+3	[-4.1e-3, 4.8e-3]
$\beta_{TS_{0,3}}$	-7.1e-3	2.6e+1	[-1.1e-2, -3.3e-3]
$\beta_{TS_{0,4}}$	-1.0e-2	2.9e+1	[-1.6e-2, -4.2e-3]
$\theta_{k'_g}$	1.7e-3	6.2e+0	[1.5e-3, 1.9e-3]
$\theta_{k'_d}$	1.3e-4	2.2e+1	[8.8e-5, 2.0e-4]
θ_{TS_0}	4.3e+1	4.0e+0	[3.9e+1, 4.6e+1]
θ_R	1.5e-3	4.9e+1	[6.4e-4, 3.5e-3]
$\xi_{k'_{g,2}}$	-2.9e-1	4.3e+1	[-5.4e-1, -4.0e-2]
$\xi_{k'_{g,3}}$	-8.0e-2	1.9e+2	[-3.6e-1, 2.1e-1]
$\xi_{k'_{g,4}}$	-2.9e-1	7.0e+1	[-7e-1, 1.1e-1]
$\xi_{k'_{d,2}}$	7.6e-1	4.0e+1	[1.6e-1, 1.3e+0]
$\xi_{k'_{d,3}}$	3.7e-1	9.0e+1	[-2.8e-1, 1.0e+0]
$\xi_{k'_{d,4}}$	3.4e-1	1.4e+2	[-5.9e-1, 1.3e+0]
$\xi_{TS_{0,2}}$	-9.2e-1	5.9e+0	[-1.0e+0, -8.1e-1]
$\xi_{TS_{0,3}}$	-4.9e-1	1.3e+1	[-6.1e-1, -3.5e-1]
$\xi_{TS_{0,4}}$	-2.6e-1	3.2e+1	[-4.3e-1, -9.7e-2]
ξ_{R_2}	9.7e-1	3.9e+1	[2.1e-1, 1.7e+0]
ξ_{R_3}	7.8e-1	5.8e+1	[-3.5e-1, 1.7e+0]
ξ_{R_4}	1.5e+0	4.7e+1	[4.2e-2, 2.8e+0]
ω_{1,k'_g}	8.3e-1	8.2e+0	[7.1e-1, 9.8e-1]
ω_{1,k'_d}	1.7e+0	9.9e+0	[1.4e+0, 2.1e+0]
ω_{1,TS_0}	3.9e-1	7.0e+0	[3.4e-1, 4.5e-1]
$\omega_{1,R}$	2.3e+0	1.6e+1	[1.7e+0, 3.1e+0]
ω_{2,k'_g}	5.5e-1	8.6e+0	[4.6e-1, 6.4e-1]
ω_{2,k'_d}	7.1e-1	1.3e+1	[5.3e-1, 9.1e-1]
ω_{2,TS_0}	5.3e-1	2.7e+0	[5.0e-1, 5.6e-1]
$\omega_{2,R}$	5.6e-1	4.2e+1	[1.2e-1, 1.0e+0]
λ	-3.4e-1	8.6e+1	[-1.0e+0, -1.6e-1]
σ_1	1.9e+0	5.4e+0	[1.7e+0, 2.1e+0]
σ_2	5.6e-2	4.3e+0	[5.0e-2, 6.2e-2]

Individual fits showed the good ability of the model to describe the data, despite the large diversity of longitudinal profiles (Figure 5.1). The model was able to capture different lesion kinetics between patients (i.e., liver lesions of patients A6181170 198 and A6181170 234) and within the same patient (i.e., patient A6181170 296), including lesions with heterogeneous responses to treatment, that is, some lesions growing and some others shrinking.

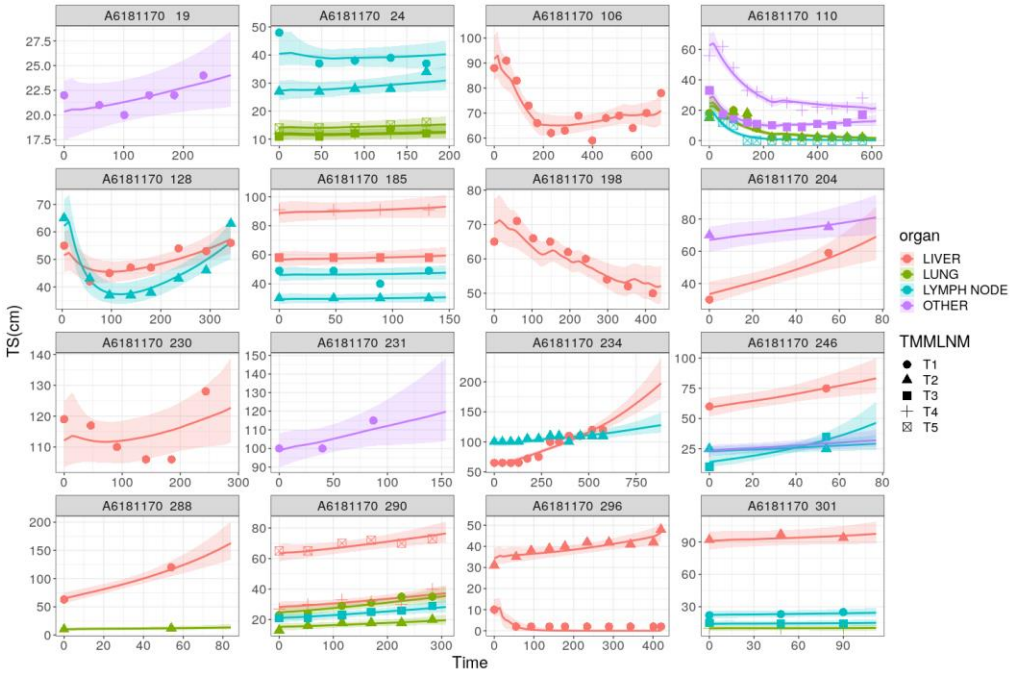

Figure 5.1 Individual fits for a subset of 25-patients. Different colors represent different organs while different point-shapes represent different lesions.

After accounting for IIV and the organ-effect the inter-lesion variability was not negligible. Notably, ω_{2,TS_0} was greater than ω_{1,TS_0}, meaning that the inter-lesions heterogeneity of baseline lesion sizes within a patient was greater than between inter-patient heterogeneity. IIV was particularly large for the tumor growth rate parameter (k'_g) and the treatment effect parameters (k'_d, R). For these parameters, the proportion of total variance explained by inter-lesion variability was 55%, 71% and 56%, respectively.

5.6.6. Organ-specific lesion kinetics

Table 5.4 presents the posterior mean estimates of the longitudinal population parameters, stratified by organ.

Table 5.4 posterior median estimates and 95% credibility interval of the longitudinal population parameters stratified by organ.

Parameter	k'_g		k'_d		TS_0		R	
	Median	95%CI	Median	95%CI	Median	95%CI	Median	95%CI
Liver	1.7e-3	[1.5e-3, 1.9e-3]	1.3e-4	[8.8e-5, 2.0e-4]	4.3e+1	[3.9e+1, 4.6e+1]	1.5e-3	[6.4e-4, 3.5e-3]
Lung	1.3e-3	[9.9e-4,1.7e-3]	2.9e-4	[1.4e-4, 5.8e-4]	1.7e+1	[1.5e+1, 1.9e+1]	3.8e-3	[1.1e-3, 1.2e-2]
Lymph Node	1.6e-3	[1.1e-3, 2.3e-3]	2.0e-4	[8.5e-5, 4.4e-4]	2.6e+1	[2.2e+1, 3.0e+1]	3.2e-3	[7.5e-4, 1.1e-2]
Other	1.3e-3	[8.3e-4, 1.9e-3]	1.9e-4	[7.4e-5, 5.0e-4]	2.7e+1	[2.7e+1, 3.9e+1]	7.1e-3	1.4e-3, 3.1e-2]

The baseline lesion size was found to be significantly smaller in secondary locations compared to the liver, with the liver baseline lesion size being approximately double that of the lung. Several other organ-specific fixed effects were notably different from zero. Specifically, the growth rate in the lung was significantly slower than in the liver, while no significant differences were observed for lymph nodes or other locations. A similar pattern was observed for the drug effect at baseline. Differently, resistance to treatment was significant across all the organs, with metastases showing greater resistance, indicated by a faster decline in the drug effect. For parameters that were not significantly different from zero, either there was insufficient information or the differences from the liver were not substantial. In Figure 5.2, longitudinal PPC stratified by organ are reported. It can be noticed that PPCs accurately describe data.

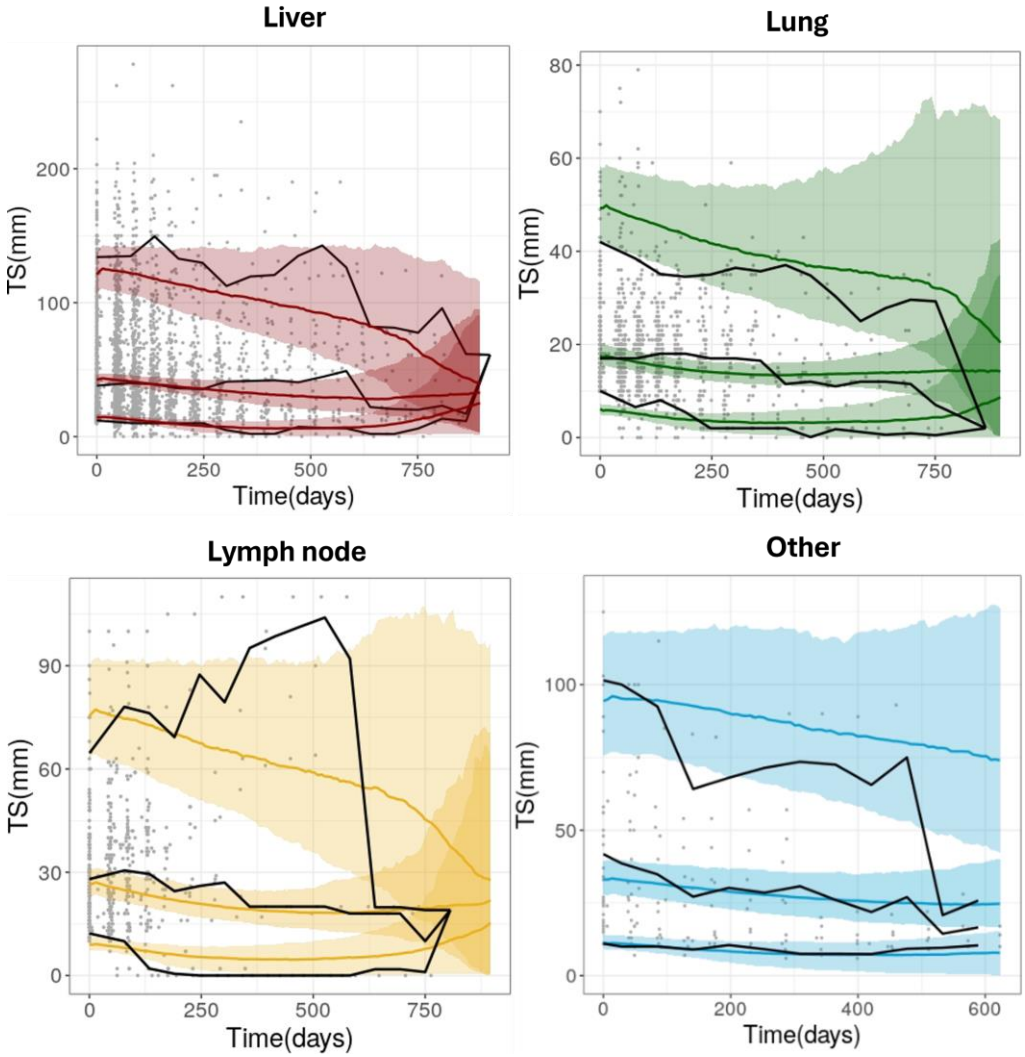

Figure 5.2 Longitudinal PPC stratified by organ. The black solid lines represent the observed median, 5th, and 95th percentiles. The solid-colored lines represent the predicted median, 5th, and 95th percentiles. The colored area depicts the 90%CI for each percentile.

5.6.7. Association between individual lesions and survival

Under the finite-time association structure, only the dynamics of liver and lung lesions, characterized by the parameter β_{C_t}, significantly impacted on patient survival (Table 5.3). In contrast, the presence of metastasis in the lymph nodes or other locations significantly decreased survival time, regardless of lesion dynamics. Liver tumor size at baseline was also a significant predictor of reduced survival, while lung tumor size did not show a similar effect. Clinically, this suggests that having a liver tumor is associated with a significant decrease in patient survival, particularly if the tumor is larger or more aggressive. On the other hand, while the presence of lung metastases negatively affects survival, the number or size of these

lesions does not appear to be critical factors. For metastases in the lymph nodes or other locations, the growth rate of the tumors does not influence survival. However, the mere presence of such metastases is associated with a faster decline in patient survival compared to those without these metastases.

Link factor magnitude E was then computed for each factor f. In Figure 5.3, panel A, median factors values and their 95%CI are shown, highlighting factor that were significantly different from zero. Therefore, Panel B shows that the most impacting factor is the C_t related to lung metastasis. Indeed, if metastasis have reached the lung in two patients, if the most aggressive/less sensible to treatment metastasis is growing fast (i.e. 97.5th) in patient 1 and slow (i.e. 2.5th) in patient 2, the median survival time of patient 1 is about one-sixteenth of patient 2 ($E_{C_{t,LUNG}} = -4.02$ [-7.15, -1.80]). Other significant longitudinal parameters that impacted patients' survival includes $f_{C_{t,1}}$, followed by $f_{TS_{0,4}}$ and $f_{TS_{0,1}}$.

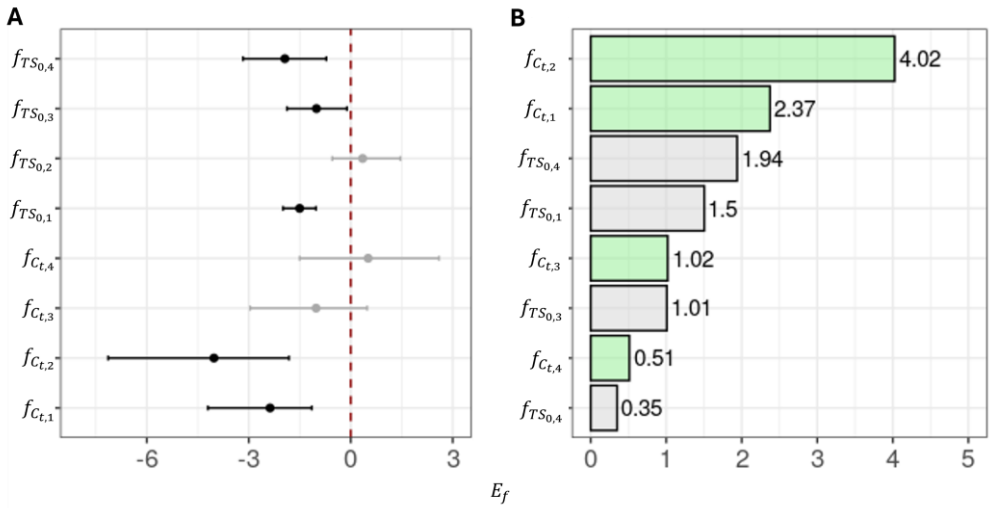

Figure 5.3 Covariate effect values E_C for the tested covariates. Black dots indicate the median values, vertical bars represent the 95%CI, and the dashed red line indicates $E_f = 0$.

Then, the following comparison involve the ablation of the tumor size effect and the concentration threshold effect C_t, accounting for all lesion altogether. Table 5.5 shows that, according to both evaluation metrics, C_t ablation impact is greater than not accounting for lesion size. Indeed, the drop in the evaluation metrics is higher for both WAIC (+140.0 vs 103.6) and LOOIC (+105.6 vs +37.4).

Table 5.5 Results of the ablation of factors in the association link function.

	No F_{TS_0}	No F_{C_t}
Δ_{WAIC}	+103.6	+140.0
Δ_{LOOIC}	+37.4	+105.6

5.6.8. Prior vs posterior

We analyzed the posterior distributions for the parameters $\theta_{k'_g}$, $\theta_{k'_d}$, $\omega_{k'_g}$ and $\omega_{k'_d}$ compared to the respective a priori distributions.

Figure 5.4 shows prior vs posterior graphical analysis. In Panel A, the posterior distribution of population parameters $\theta_{k'_g}$ and $\theta_{k'_d}$ for the main location (liver, $\xi = 0$) and other organs ($\theta_{k'_g} + \xi_{k'_g,j}$, $\theta_{k'_d} + \xi_{k'_d,j}$) are compared to the prior distribution obtained from the translational approach. The analysis indicates that the prior and posterior distributions closely match. However, for inter-individual parameters (Panel B), the prior and posterior distributions do not align as closely with the prior underestimating the observed variability in the data.

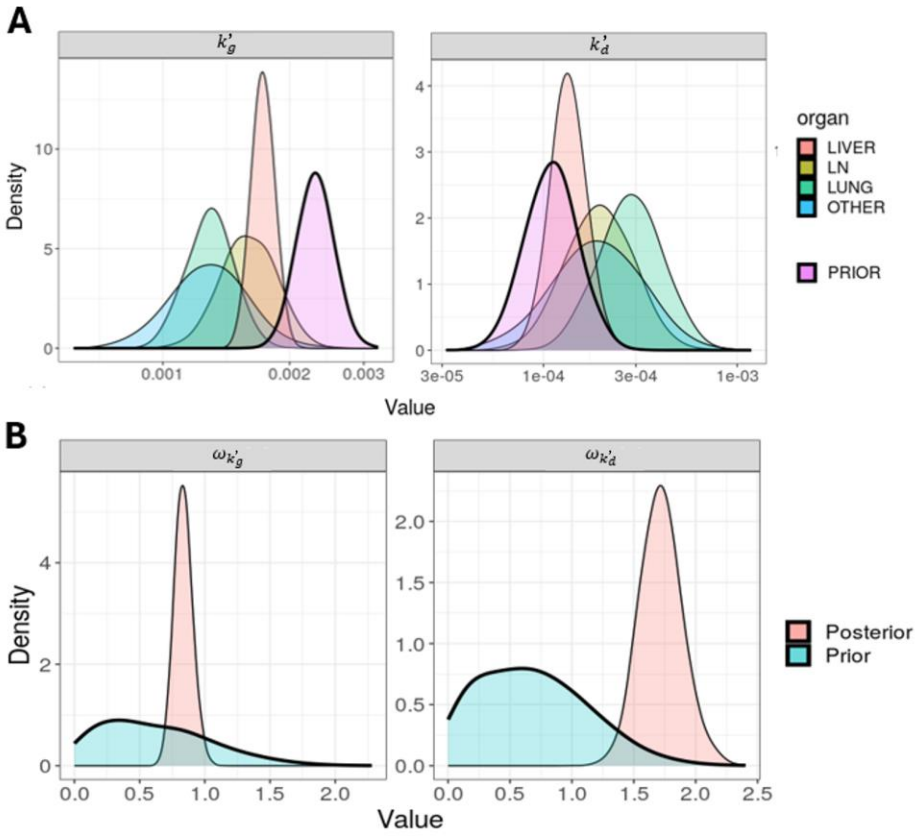

Figure 5.4 Prior vs Posterior. **(A)** shows prior distribution (violet area under the thick black line) and posterior distributions for $\theta_{k'_g}$ and $\theta_{k'_d}$ together with

$\theta_{k'_g} + \xi_{k'_g,j}$ and $\theta_{k'_d} + \xi_{k'_d,j}$ (colored areas under the thin black lines). **(B)** shows prior distribution (blue area under the thick black line) and posterior distribution for $\omega_{k'_g}$ and $\omega_{k'_d}$ (pink area under the thin black line).

5.6.9. Comparison using alternative prior models

A sensitivity analysis was conducted comparing the PI model with the LI and UI alternative prior models.
The results show that the PI model has better WAIC and LOOIC values, indicating its advantages. Additionally, the PI model has a shorter computational time (PI: ~10h, LI: ~12h, UI: ~13h). Table 5.6 provides a summary of these findings.

Table 5.6 Different prior model comparisons on the Phase III trial dataset

	PI	**LI**	**UI**
$WAIC$	31479.8	31587.0	31528.2
$LOOIC$	32083.8	32089.9	32101.0
Time (hrs)	10.1	11.8	11.6

5.6.10. Phase II trial simulation

Convegence. Two mild criteria ($R_{hat} < 1.05$ and $ESS > 100$) and two more strict criteria ($R_{hat} < 1.01$ and $ESS > 400$) where employed to test the convergence of the models. In Table 5.7 the percentage of simulated trial that reach convergence criteria are reported.

Table 5.7 Convergence results for the Phase II trial simulation

	PI model	LI model	UI model
$R_{hat} < 1.05$	86%	78%	75%
$R_{hat} < 1.01$	19%	11%	11%
$ESS > 100$	78%	68%	66%
$ESS > 400$	25%	10%	8%

As can be observed from the table, for every criterion, PDX-informed model reaches convergence in more simulated trials than the two alternative prior models, underlining the impact of having an informative prior on model's stability.

Parameter estimation. The three different prior models are then compared in terms of parameter estimation. Specifically, the three parameters that are more effected by alternative prior information are here compared and the results reported in Figure 5.5. Observing the prior distribution, it can be

observed that the posterior variability is way lower in PDX prior for parameter k_g, in comparison with UI, while PDX and LI distributions are almost overlapped. Otherwise, considering the k'_d parameters, only PI model manages to return a consistent parameter estimation across different simulated trials. For the R parameters, for which the prior distribution is shared along the three different models, a slightly different can be observed from this analysis.

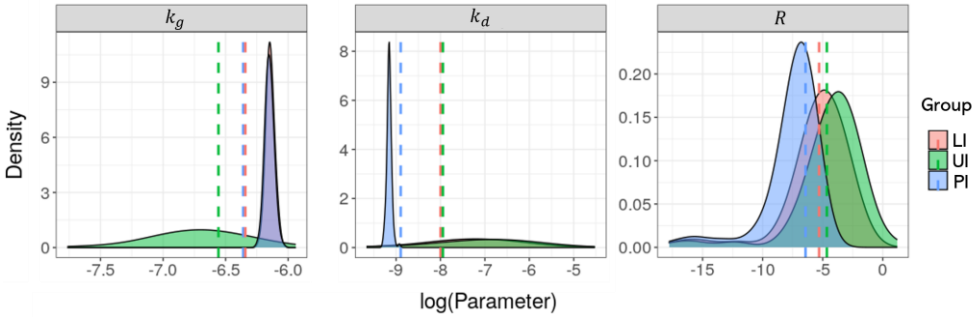

Figure 5.5 Comparison of parameter estimation for k'_g, k'_d and R parameters. Different colored-areas represent different prior model (PI blue, LI pink, UI green). Dashed vertical lines indicate the median parameter values estimated on the original Phase III trial.

Association link factors assessment. The three models are compared based on the number of simulations where factors are significant, as shown in the table below. It is important to note that the percentages are intended for model comparison rather than absolute interpretation. Indeed, the low percentages of simulations that include tumor size at the baseline for lymph node and other lesions might seem low. However, these percentages are influenced by the sampling procedure. Lymph node and other locations can be strongly underrepresented when sampling only 40 patients, making precise parameter estimation challenging.

Table 5.8 Covariate inclusion results for the Phase II trial simulation

Link parameter	Percentage of Simulated Phase II Trials that includes the covariate			Significance in Full Phase III Trial (Yes/No)
	PI	LI	UI	
$\beta_{C_{t,1}}$	63%	59%	52%	Yes
$\beta_{C_{t,2}}$	57%	54%	46%	Yes
$\beta_{C_{t,3}}$	5%	4%	7%	No
$\beta_{C_{t,4}}$	6%	3%	2%	No
$\beta_{TS_{0,1}}$	50%	50%	49%	Yes
$\beta_{TS_{0,2}}$	21%	23%	22%	No
$\beta_{TS_{0,3}}$	20%	17%	15%	Yes
$\beta_{TS_{0,4}}$	20%	19%	20%	Yes

5.7. Wrap up and future developments

This chapter describes the second application of the translational framework, specifically focused on advancing nonlinear joint modeling of tumor dynamics and survival outcomes using Bayesian methods enriched by preclinical insights.

Historically, joint models in oncology predominantly used linear components due to their simplicity. However, linear models often fail to capture the complex nature of tumor growth and treatment response. Nonlinear joint models, which can represent exponential growth or decay patterns, offer a more realistic depiction of tumor dynamics. The use of nonlinear joint models in advanced cancer is often limited to summary measures like the SLD of tumors, which can oversimplify analyses when multiple lesions are present in different organs. To achieve a more comprehensive and detailed understanding of treatments effect on tumors, it is important to employ more biologically sophisticated models that accounts for the dynamics of individual lesions rather than relying solely on aggregate measures.

However, one challenge in nonlinear joint modeling is the complexity of calculating the likelihood function and estimating parameters, especially when modeling tumor dynamics at the individual lesion level. Bayesian inference offers a solution by incorporating prior information and managing uncertainty effectively. However, the potential of Bayesian methods is often underutilized due to the reliance on non-informative priors, leading to less accurate parameter estimates.

By leveraging preclinical data and our model-based translational framework to inform prior distributions, we aimed to enhance the accuracy of joint models that integrate longitudinal tumor measurements with TTE data.

Two main achievements are reached in this application. The first one is to develop a non-linear joint model accounting for individual lesion variability in the context of hepatocellular cancer treated with Sorafenib, which clinical relevance is independent on the use of PDX-derived priors. Our analysis found that liver and lung lesions have a notable impact on patient survival, with dynamics of lung lesions being particularly influential. The analysis reveals that also lymph node or other location metastasis size has a significant influence on patient survival. Furthermore, the model successfully captured variability in tumor growth and treatment response across different lesions, revealing that inter-lesion variability is more significant than inter-patient variability.

The second key achievement involves the use of information from PDX models. The results show several important advancements. First, the analysis

revealed that the prior distributions for θ_{k_g} and θ_{k_d} closely matched the posterior distributions while the predicted clinical IIV is underestimated. Furthermore, integrating preclinical-derived priors improved model accuracy. Indeed, the use of highly informative priors for tumor growth and drug effects resulted in more precise parameter estimates and a better model fit (Table 5.6), as evidenced by the lower WAIC and LOOIC values for the PI model compared to other models. This point is important because having a prior closely aligned with the posterior can be beneficial. However, it is not always ideal if the prior is too restrictive. An overly constrained prior can limit the model flexibility, even when it does not accurately reflect the true values. The benefits of using informative priors were further confirmed in simulated Phase II trials, where they led to more successful model convergence and more consistent parameter estimates across trials.

Despite its many advantages, the proposed approach has some limitations. The benefits demonstrated are based on a single case study, and its generalizability remains uncertain. Additionally, while the method uses an existing preclinical analysis, creating a pipeline from scratch, such as generating PDX animal models and conducting TGI studies, would be costly and challenging to justify solely based on improvements in accuracy, convergence, and fit. However, since preclinical studies are common in drug development, the translational framework could be used to inform clinical data analysis without generating new preclinical models. Future research should focus on applying this approach to a broader range of case studies to further validate the use of joint models with priors from the proposed translational framework.

Chapter 6

Conclusions

This thesis presents the development and application of a translational modeling framework designed to predict tumor dynamics and PFS in cancer patients based on preclinical data from PDX mice. The work contributes to bridging the gap between preclinical research and clinical outcomes, offering a systematic approach to predicting cancer dynamics and aiding in the design of more efficient clinical trials.

The first part of the research focused on untreated cancer patients. A method was developed to predict TVDT distributions and PFS curves by analyzing tumor growth data in PDX mice. This approach relied on the assumption of exponential growth for human tumors and used allometric scaling to translate findings from mice to humans. The predictions closely matched clinical data, with the framework successfully capturing the median TVDT values across multiple cancer types. However, some limitations were noted, particularly in estimating inter-patient variability, which was partly attributed to the limited number of PDX models available for each cancer type. While these limitations suggest areas for improvement, the overall results demonstrated that the framework can effectively predict tumor growth dynamics in untreated patients.

Building on this foundation, the framework was extended to account for the effects of anticancer treatments. The methodology was applied to two case studies, i.e., Gemcitabine treatment for pancreatic cancer and Sorafenib treatment for hepatocellular carcinoma. The framework proved capable of predicting tumor size dynamics and PFS in treated patients, with results generally aligning with clinical outcomes. The addition of mortality risk models helped refine the PFS predictions, particularly in cases where deaths played a significant role. Although the framework performed well, there

were some discrepancies, particularly in predicting extreme tumor size percentiles and accounting for drug resistance mechanisms.

The following part of the thesis explored two practical applications of the developed translational framework in clinical trial design.
First, by integrating virtual patients generated from PDX data into hybrid control arms, the study addressed challenges related to single-arm and/or low enrollment in cancer trials. The study demonstrated that hybrid control arms, which combine real patients with virtual patients generated from PDX data, could closely replicate the outcomes of traditional control arms. In several clinical trials where Sorafenib is used as the standard-of-care treatment for patients with HCC, the hybrid approach produced hazard ratios and log-rank test results nearly identical to those observed in trials with only real patients. This suggests that hybrid control arms can effectively maintain the scientific rigor and validity of clinical trials while significantly reducing the reliance on large numbers of real patients. However, some limitations were identified. The approach primarily focused on PFS as the endpoint, which does not capture all aspects of treatment efficacy, such as overall survival. Additionally, the virtual patients did not account for individual characteristics like genetics or comorbidities, which could affect the accuracy of predictions. Future works should explore incorporating more personalized data into the virtual models and refining the integration of real and virtual patients to enhance the framework applicability across different cancer types and treatment scenarios.
The second application of the framework advanced the nonlinear joint modeling of tumor dynamics and survival outcomes using Bayesian methods enriched with preclinical insights. The control arm of NCT00699374 Phase III is used as a case study. Individual lesion dynamic data of 416 Asian patients with hepatocellular cancer treated with Sorafenib were analyzed. The study demonstrated that informative prior distributions derived from preclinical PDX data, via the proposed translational framework, could help complex joint model to converge and could lead to better and faster parameter estimations rather than when relying on less-informative priors derived from the literature. This evidence shown on the full Phase III trial was then further underlined by simulating Phase II trials. Applied to a single case study, it would be interesting to extend the methodology to a larger pool of tumor types and treatments.

To conclude, this thesis presents a translational modeling framework that predicts tumor growth and PFS in cancer patients using data from PDX models. The framework accurately forecasts tumor dynamics in both untreated and treated patients. Moreover, the practical applications of the framework in clinical trial design highlight its potential to innovate the field.

The integration of virtual patients into hybrid control arms offers a novel solution to challenges in cancer trials while the use of Bayesian methods and preclinical information to enhance the modeling of tumor dynamics and survival outcomes further emphasizes the framework's capability in improving clinical predictions.

Appendix A

Supplementary material for Chapter 2

A.1. Calculation of time of progression

Based on a simplified version of the RECIST, progressive disease (PD) events due to target lesions progression were defined as a 20% increase of the sum of longest diameters of target tumor lesions. To compute time of progression, t_{event}, tumors were assumed to be composed by a single spherical lesion. Let d be the tumor diameter. Thus, a PD event occurs in t_{event} if:

$$\boldsymbol{d(t_{event}) = 1.2 d_0} \qquad \text{(Eq. A.1)}$$

where $\boldsymbol{d_0}$ is the basal tumor diameter. Using the volume of a sphere, it followed that

$$\boldsymbol{V(t_{event}) = \frac{4}{3}\pi\left(\frac{d(t_{event})}{2}\right)^3 = \frac{4}{3}\pi\left(\frac{1.2 d_0}{2}\right)^3 = 1.2^3 V_0 = 1.728 V_0} \qquad \text{(Eq. A.2)}$$

where $V_0 = \frac{4}{3}\pi\left(\frac{d_0}{2}\right)^3$ was the basal tumor volume. Thus, the tumor volume change associated to a 20% increase in diameter corresponded to a 1.728-fold change. Let now suppose that tumor volume grows exponentially with a rate λ, thus:

$$\boldsymbol{V(t_{event}) = V_0 e^{\lambda t_{event}}}. \qquad \text{(Eq. A.3)}$$

Equaling the right expressions of Eq. A.2 and A.3, it followed:

$$\boldsymbol{V_0 e^{\lambda t_{event}} = 1.728\, V_0}$$

and applying the logarithm

$$\boldsymbol{t_{event} = \frac{ln(1.728)}{\lambda}}$$

For simplicity, in this work we assumed that tumor lesion is spherical in shape and grows accordingly. We demonstrated that, under this assumption, a disease progression event (i.e., 20% increase of longest diameter) can express as 1.728-fold increase in tumor volume. This relationship still holds also for not-spherical tumors under the hypothesis that tumor growth rate is the same in the three spatial dimensions (a condition that is intrinsically true for spherical mass).

For example, if we consider an ellipsoidal tumor (a common more realistic alternative to spherical shape assumption), its volume is given by:

$$\boldsymbol{V(t) = \frac{4}{3}\pi \cdot L(t) \cdot l_1(t) \cdot l_2(t)} \quad \text{(Eq. A.4)}$$

where $L(t)$ is the radius of the longest length, i.e., $\boldsymbol{L(t) = d(t)/2}$, and $l_1(t), l_2(t)$ the radius of the shorter ones. Under the hypothesis that tumor growth follows the same dynamics in all the three spatial dimensions, also the radius of shorter lengths can express as a function of $\boldsymbol{d(t)}$, i.e., $l_1(t) = \alpha_1 L(t)$ and $l_2(t) = \alpha_2 L(t)$ with α_1, α_2 constants ≤ 1. Thus, it followed that the tumor volume is given by:

$$\boldsymbol{V(t) = \left(\frac{4}{3}\pi \cdot \alpha_1\alpha_2 \cdot \left(\frac{d(t)}{2}\right)^3\right)} \quad \text{(Eq. A.5)}$$

Combining Eq. A.1 and Eq. A.5, it followed that when a progression event occurs, the tumor volume is:

$$\boldsymbol{V(t_{event}) = \left(\frac{4}{3}\pi \cdot \alpha_1\alpha_2 \cdot \left(\frac{1.2^3\, d_0}{2}\right)^3\right) = 1.2^3 V_0 = 1.728 V_0} \quad \text{(Eq. S2.6)}$$

where $V_0 = \frac{4}{3}\pi \cdot \alpha_1\alpha_2 \cdot \left(\frac{d_0}{2}\right)^3$. This is the same equation derived under the assumption that tumor is spherical.

A.2. Complete List of the analyzed PDX experiments

Table A1 Considered PDX mouse models.

BR	CC	CR	GA	HN	LI	LU ADC	LU SCC	ME	PA	SA
BR10014	CC6679	CR0004	GA0006	HN0366	LI0050	LU1147	LU0350	ME1154	PA0372	SA0639
BR10539	CC6639	CR0012	GA0023	HN0586	LI0348	LU11606	LU0357	ME11971	PA0692	SA10199
BR10582	CC6638	CR0150	GA0044	HN0696	LI0612	LU1235	LU0367	ME11972	PA1194	SA13127
BR1115	CC6279	CR0170	GA0046	HN1972	LI0801	LU1380	LU0395	ME12035	PA1198	SA13226
BR1282	CC6216	CR0193	GA0055	HN2174	LI1005	LU1452	LU0697	ME12047	PA1222	SA13389
BR1283	CC0449	CR0196	GA0080	HN2221	LI1025	LU2038	LU0741	ME12056	PA1233	SA3224
BR1458	CC11307	CR0205	GA0087	HN2574	LI1035	LU2049	LU0743	ME12057	PA1265	SA3283
BR1474	CC1470	CR1519	GA0095	HN2576	LI1037	LU2071	LU0884	ME12068	PA1280	SA3296
BR2014	CC6204	CR1801	GA0098	HN2581	LI1054	LU2505	LU1143	ME12070	PA1301	SA3829
BR3267	CC6205	CR2110	GA0119	HN2583	LI1055	LU2535	LU1155	ME12079	PA1306	SA3831
BR5009	CC6600	CR2161	GA0138	HN2586	LI1058	LU5165	LU1160	ME12080	PA1332	SA4062
BR5010	CC6604	CR2394	GA0151	HN2594	LI1069	LU5176	LU1204	ME12107	PA1338	SA4094
BR5011	CC6607	CR2517	GA0318	HN2606	LI1074	LU5187	LU1206	ME12120	PA1390	SA4097
BR5013	CC6609	CR2518	GA0429	HN3504	LI1078	LU5194	LU1423	ME12149	PA2410	SA4109
BR5015	CC6614	CR2519	GA2101	HN3508	LI1081	LU5209	LU1661	ME12172	PA3013	SA4128
BR6695	CC6625	CR2524	GA2278	HN3537	LI1097	LU5212	LU1690	ME12208	PA3029	SA4148
BR9456	CC6637	CR2814	GA3055	HN3642	LI1098	LU5240	LU1776	ME12212	PA3065	
BR9464	CC6645	CR3079	GA3121	HN3674	LI6206	LU5245	LU3075	ME12216	PA3126	
BR9465	CC6658	CR3150	GA3158	HN3690	LI6280	LU5247	LU6439	ME12217	PA3127	
BR9466	CC6680	CR3315	GA3839	HN3712	LI6281	LU5349	LU6440	ME12222	PA3136	
BR9469	CC6724	CR3496	GA6200	HN3792	LI6605	LU5371	LU6901	ME13996	PA3137	
BR9479	CC9326	CR3612	GA6212	HN3796	LI6610	LU5381	LU6905	ME2194	PA3139	
BR9480	CC9506	CR6219	GA6822	HN5111	LI6611	LU6412	LU6917	ME2319	PA6233	
BR9493		CR6227	GA6877	HN5125	LI6612	LU6414	LU9357	ME5285	PA6259	

Notes: (*) PDX codes from HuBase database (Crownbio Bioscience Inc., https://www.crownbio.com/).

A.3. TVDT data in untreated cancer patients

Clinical data indicated that the frequency distribution of TVDT obtained is positively skewed, with some very long TVDTs compared to the typical value. To mitigate the impact of these outliers, a range of TVDT variation was estimated for each study based on the following strategy:

- TVDT was supposed to be log-normally distributed, i.e., $TVDT = TVDT_{median} \cdot e^{\eta}$ *with* $\eta \sim \mathcal{N}(0, \sigma^2)$ and $TVDT_{median}$ fixed to the reported median;
- the observed $[TVDT_{minimum}, TVDT_{maximum}]$ range was supposed representative of the 95%CI of TVDT; consequently, the 95%CI of η was given by $\left[\ln\left(\frac{TVDT_{minimum}}{TVDT_{median}}\right), \ln\left(\frac{TVDT_{maximum}}{TVDT_{median}}\right)\right] = [-2\sigma, 2\sigma]$, as η is normally distributed with zero mean; thus, σ could be approximated as $\sigma = \ln\left(\frac{TVDT_{maximum}}{TVDT_{minimum}}\right)/4$;
- 10th and 90th percentiles (p10 and p90) of η were computed;
- the range of TVDT (80% CI) was approximated with $[TVDT_{median}e^{p10}, TVDT_{median}e^{p90}]$.

For cancer type for which multiple studies are available, the geometric means of the medians weighted by the corresponding number of patients, $\overline{\boldsymbol{TVDT_{median}}}$, were used to summarize the typical TVDT value. In addition, a unique lognormal distribution was reconstructed for each cancer type and parametrized as $\boldsymbol{TVDT = \overline{TVDT_{median}}\exp(\varphi)}$ with $\boldsymbol{\varphi \sim \mathcal{N}(0, \nu^2)}$ where the variance $\boldsymbol{\nu^2}$ was computed as the algebraic mean of the $\boldsymbol{\sigma^2}$ weighted by the number of patients. From the obtained distributions, a unique range, 80% CI, for each cancer type was derived considering $[\overline{\boldsymbol{TVDT_{median}}}\boldsymbol{e^{p10}}, \overline{\boldsymbol{TVDT_{median}}}\boldsymbol{e^{p90}}]$. The predicted TVDT ranges stratified by study and cancer type is reported in Table A2.

Table A2 Observed TVDT [month] in untreated cancer patients stratified by study and cancer type.

Cancer Type	Reference	N. pz	Individual TDVT data	Median TVDT [month]	Reported TVDT range [month]	Estimated 80%CI of TVDT [month]	Estimated median TVDT for cancer type [month]	Estimated sd*, v_{TVDT}, for cancer type [-]	Estimated 80%CI of TVDT by cancer type [month]
BR	Fournier	147	Y	7.97	[1.47, 62.3]	[2.4, 26.7]	5.66	0.84	[1.92, 16.55]
	Gershon-Cohen	18	Y	4	[0.77, 6.97]	[1.98, 8.12]			

Cancer Type	Reference	N. pz	Individual TDVT data	Median TVDT [month]	Reported TVDT range [month]	Estimated 80%CI of TVDT [month]	Estimated median TVDT for cancer type [month]	Estimated sd*, v_{TVDT}, for cancer type [-]	Estimated 80%CI of TVDT by cancer type [month]
	Ryu	66	N	4.7	[1.53, 27.5]	[1.87, 11.85]			
	Tabbane	75	N	3.83	[0.47, 25.73]	[1.06, 13.76]			
	Zhang	69	N	5.47	[2.2, 17.37]	[2.81, 10.66]			
CC	De Rose	79	N	2.33	[0.48, 17.07]	[0.75, 7.32]	-	0.89	-
CR	Bolin	27	N	4.33	[1.77, 52.33]	[1.46, 12.93]	6.12	0.59	[2.87, 13.02]
	Burke	43	N	7.03	[3.73, 13.47]	[4.66, 10.59]			
	Tada	12	Y	8.11	[3.08, 34.41]	[3.75, 17.44]			
GA	Haruma	12	Y	8.1	[2.2, 23.4]	[3.8, 17.22]	8.57	0.74	[3.33, 22.16]
	Seung-Young	97	N	8.63	[1, 21.1]	[3.27, 22.97]			
HN	Jensen	61	N	3.3	[0.5, 7.8]	[1.36, 7.96]	2.99	0.68	[1.26, 7.18]
	Waaijer	13	Y	1.9	[0.7, 8.53]	[0.85, 4.25]			
LI	Barbara	58	N	5.72	[0.91, 20.19]	[2.12, 15.28]	3.22	0.68	[1.35, 7.7]
	Kubota	22	N	2.77	[1.08, 16.55]	[1.16, 6.63]			
	Park	59	Y	2.03	[0.7, 6.97]	[0.98, 4.22]			
	Sheu	30	Y	3.9	[0.97, 13.27]	[1.69, 8.96]			
	Nakajima	34	Y	2.48	[0.57, 9.13]	[1.03, 6.02]			
LU ADC	Honda	34	Y	8.53	[2.3, 91.2]	[2.61, 27.63]	5.52	0.89	[1.77, 17.3]
	Kanashiki	140	N	4.47	[1.53, 49.77]	[1.47, 13.67]			
	Mackintosh	36	N	8.3	[1.8, 75.2]	[2.53, 27.44]			
LU SCC	Honda	11	Y	4.37	[1.3, 7.37]	[2.51, 7.55]	3.46	0.65	[1.5, 7.95]
	Kanashiki	44	N	3.3	[1.33, 23.73]	[1.31, 8.27]			
	Mackintosh	6	N	3.23	[2.2, 8.5]	[2.08, 4.98]			
ME	Carlson	5	Y	3.13	[1.67,11.23]	[1.69, 5.78]		0.48	-
PA	Furukawa	9	Y	4.8	[2.13, 8.5]	[3.07, 7.53]	3.74	0.36	[2.36, 5.94]
	Rezai	10	Y	2.99	[1.13, 5.03]	[1.87, 4.83]			
SA	Galante	44	Y	0.24	[0.05,4.23]	[0.06, 0.99]	0.27	1.07	[0.07, 1.06]
	Spratt	5	Y	0.83	[0.7,5.83]	[0.42, 1.63]			

Notes: (*)ω = standard deviation of the associated normal distribution.

A.4 PFS data in untreated cancer patients

Table A3 Published PFS curves.

Cancer Type	Reference	N. pz	Cohort/ Treatment	Median PFS [month]	Median OS [month]	Overall response rate
CC	Casak 2022	61	Placebo	1.4 [1.34, 1.85]	7.5 [4.8, 11.1]	-
	Zhu 2021 *	59	Placebo	1.6 [1.46,1.86]	7.5 [4.8, 11.1]	-
CR	Bendell 2011	18	Capecitabine	2.53 [1.65, 3.26]	7.6 [5, 16.3]	7%
	Cutsem 2007	232	Best supportive care	1.8 [1.77, 2.02]	6.5 [na]	-
	Dasari 2023	230	Placebo	1.8 [1.8, 1.93]	4.8 [4, 5.8]	-
	Hecht 2017	85	FOLFIRI + Simtuzumab	5.4 [3.4, 5.6]	10.5 [9.2, 12.6]	5.9%
GA	Bang 2015	62	Paclitaxel	3.55 [2.35, 5.12]	8.3 [na]	9%
	Boku 2009	234	FU	2.9 [1.7, 5.7]	10.8 [5.7, 17.8]	9%
	Ohtsu 2003	70	UFTM	2.4 [1.3, 3.2]	6 [4.6, 7.4]	9%
	Vanhoefer 2000	122	ELF	3.3 [2.9, 4.43]	7.2 [6, 8.3]	5.7%
HN	Burtness 2005	60	Cisplatin	2.7 [1.9, 4.01]	8 [6.1, 10.6]	10%
	Cohen 2019	248	Standard-of-care therapy (methotrexate, docetaxel, or cetuximab)	2.3 [1.79, 2.8]	6.9 [5.9, 8]	10%
	Ferris 2016	121	Standard-of-care therapy (methotrexate, docetaxel, or cetuximab)	2.3 [1.9, 3.14]	5.1 [4, 6]	5.1%
LI	Cheng 2009*	76	Placebo	1.4 [1, 1.55]	4.2 [3.75, 5.46]	-
	Llovet 2008	303	Placebo	2.8 [2.7, 4.11]	7.9 [6.8, 9.1]	-
	Zhu 2015	282	Placebo	2.1 [1.6, 2.83]	7.6 [6, 9.3]	-
ME	Chapman 2011	274	Dacarbazine	1.6 [1.55, 1.77]	64% alive after 6 months	5%
	Hauschild 2012	40	Dacarbazine	2.7 [1.51, 2.95]	na	7%
	Kim 2013	63	Dacarbazine	1.8 [1.78, 2.04]	14% of death	0%
PA	Conroy 2011	171	Gemcitabine	3.3 [2.2, 3.83]	6.8 [5.5, 7.6]	9.4%
	Girardi 2019	54	Gemcitabine	1.7 [0.98, 2.57]	6.8 [2.6, 11.0]	9.3%
	Kindler 2010	256	Gemcitabine	2.9 [2.4, 4.52]	5.9 [5.1, 6.9]	10%
	Moore 2007	284	Gemcitabine	3.6	5.91	8%

Cancer Type	Reference	N. pz	Cohort/ Treatment	Median PFS [month]	Median OS [month]	Overall response rate
				[3.29, 4.11]	[na]	
SA	Gounder 2022	97	Placebo	2.1 [1.51, 3.06]	12.9 [8.54, 15.90]	-
	Kawai 2016	16	Placebo	1.75 [0.93, 2.91]	14.9 [6.8, na]	-

*Notes: *Kaplan Meyer curve for PFS was not available, information about time to progression (TTP) was used.*

From each of the study reported in Table S1.3, the PFS curve was digitalized. Let $S(t)$ denote its value at time t and N the number of patients involved in the study. Thus, the 95%CI of $S(t)$ for any time t was reconstructed, assuming that there were not censored data, based on the following step:

- the standard error of $S(t)$ was approximated as $SE = \sqrt{S(t)(1-S(t))/N}$;
- the 2.5 and 97.5 percentiles were approximated respectively as:
- $L(t) = S(t)e^{\frac{z_{0.025}}{\ln(S(t))}\frac{SE}{S(t)}}$ and $U(t) = S(t)e^{\frac{-z_{0.025}}{\ln(S(t))}\frac{SE}{S(t)}}$

where $z_{0.025}$ was the 2.5th percentile of the normal distribution.

A.5. Model fitting of tumor growth studies in PDX mice

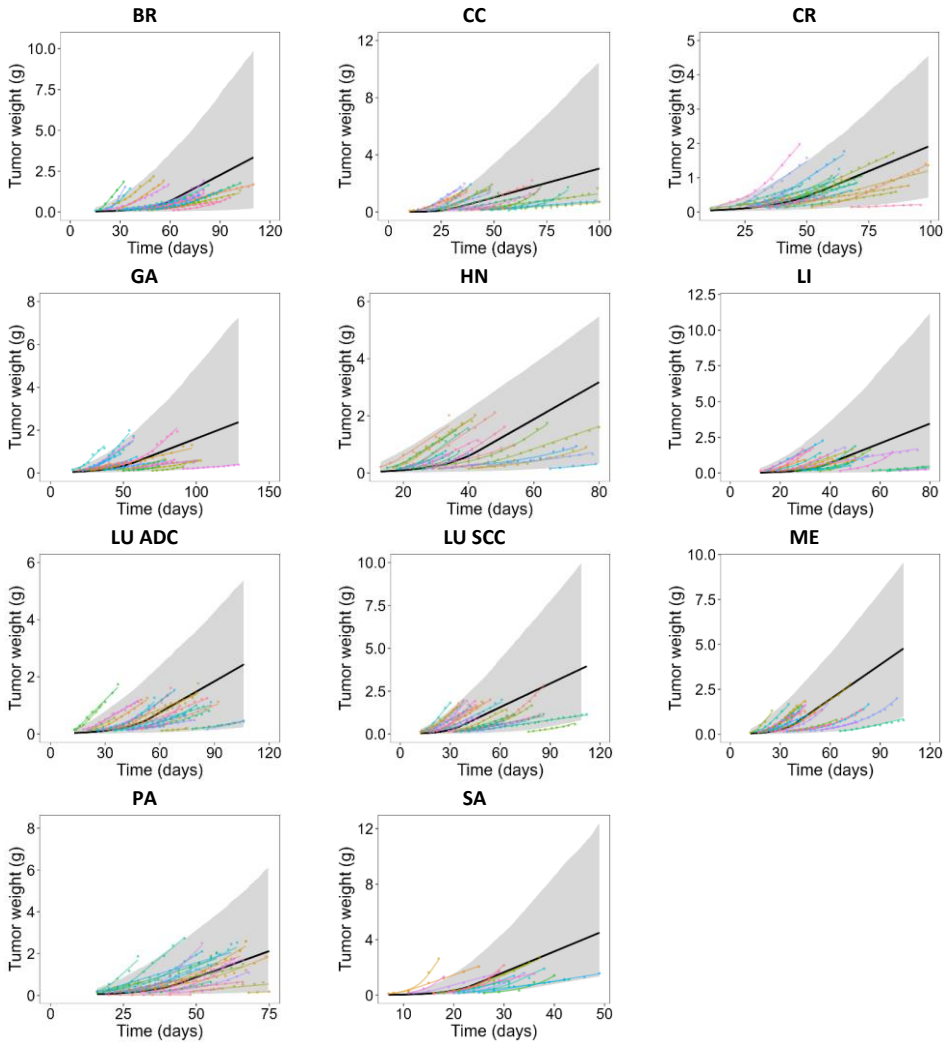

Figure A1 Fitting plots of the population Simeoni growth models in PDX mice. For each cancer type, colored dots and lines represent the individual observed and predicted tumor weight profiles stratified by PDX mouse model; black line marks the typical model prediction; grey area is the 90% CI of model predictions (2500 simulations).

Table A4 Individual parameter estimates of the Simeoni tumor growth model in PDX mice.

Cancer Type	PDX	λ_0 [1/day] Rate of exponential growth	λ_1 [cm³/day] Rate of linear growth	W_0 [g] Initial tumor weight
BR	BR10014	0.050	0.022	0.013
	BR10539	0.049	0.025	0.013
	BR10582	0.060	0.047	0.015
	BR1115	0.075	0.085	0.065
	BR1282	0.286	0.122	0.001
	BR1283	0.061	0.049	0.007
	BR1458	0.111	0.068	0.009

Cancer Type	PDX	λ_0 [1/day] Rate of exponential growth	λ_1 [cm^3/day] Rate of linear growth	W_0 [g] Initial tumor weight
	BR1474	0.049	0.024	0.024
	BR2014	0.059	0.040	0.008
	BR3267	0.043	0.034	0.040
	BR5009	0.042	0.054	0.029
	BR5010	0.040	0.057	0.027
	BR5011	0.040	0.052	0.060
	BR5013	0.049	0.106	0.037
	BR5015	0.136	0.133	0.012
	BR6695	0.057	0.053	0.019
	BR9456	0.078	0.049	0.030
	BR9464	0.058	0.059	0.014
	BR9465	0.049	0.048	0.029
	BR9466	0.061	0.034	0.011
	BR9469	0.060	0.059	0.003
	BR9479	0.062	0.071	0.009
	BR9480	0.077	0.015	0.002
	BR9493	0.061	0.040	0.008
	BR9494	0.222	0.174	0.001
CC	CC6679	0.135	0.044	0.004
	CC6639	0.256	0.051	0.004
	CC6638	0.160	0.065	0.018
	CC6279	0.153	0.058	0.006
	CC6216	0.158	0.083	0.003
	CC0449	0.088	0.010	0.002
	CC11307	0.097	0.018	0.004
	CC1470	0.088	0.151	0.003
	CC6204	0.118	0.034	0.003
	CC6205	0.138	0.042	0.004
	CC6600	0.078	0.132	0.002
	CC6604	0.162	0.127	0.006
	CC6607	0.083	0.032	0.002
	CC6609	0.155	0.061	0.005
	CC6614	0.092	0.011	0.003
	CC6625	0.205	0.091	0.007
	CC6637	0.166	0.046	0.004
	CC6645	0.140	0.020	0.003
	CC6658	0.216	0.091	0.005
	CC6680	0.135	0.012	0.004
	CC6724	0.095	0.046	0.004
	CC9326	0.130	0.007	0.003
	CC9506	0.207	0.072	0.003
CR	CR0004	0.077	0.047	0.024
	CR0012	0.063	0.019	0.012

Cancer Type	PDX	λ_0 [1/day] Rate of exponential growth	λ_1 [cm^3/day] Rate of linear growth	W_0 [g] Initial tumor weight
	CR0150	0.063	0.012	0.015
	CR0170	0.036	0.040	0.086
	CR0193	0.105	0.050	0.021
	CR0196	0.060	0.033	0.007
	CR0205	0.080	0.037	0.023
	CR1519	0.079	0.083	0.060
	CR1801	0.051	0.012	0.014
	CR2110	0.056	0.017	0.026
	CR2161	0.056	0.034	0.034
	CR2394	0.080	0.059	0.007
	CR2517	0.044	0.041	0.072
	CR2518	0.050	0.025	0.041
	CR2519	0.064	0.018	0.023
	CR2524	0.081	0.023	0.035
	CR2814	0.042	0.032	0.025
	CR3079	0.040	0.032	0.044
	CR3150	0.065	0.024	0.014
	CR3315	0.071	0.036	0.022
	CR3496	0.053	0.066	0.039
	CR3612	0.080	0.022	0.022
	CR6219	0.053	0.031	0.037
	CR6227	0.039	0.027	0.046
	CR6228	0.017	0.028	0.043
GA	GA0006	0.09	0.048	0.02
	GA0023	0.12	0.069	0.025
	GA0044	0.11	0.075	0.011
	GA0046	0.082	0.015	0.012
	GA0055	0.043	0.0088	0.02
	GA0080	0.12	0.046	0.0095
	GA0087	0.04	0.026	0.05
	GA0095	0.018	0.026	0.039
	GA0098	0.043	0.013	0.019
	GA0119	0.045	0.058	0.044
	GA0138	0.064	0.013	0.036
	GA0151	0.03	0.026	0.029
	GA0318	0.046	0.023	0.052
	GA0429	0.11	0.029	0.014
	GA2101	0.043	0.011	0.033
	GA2278	0.047	0.017	0.018
	GA3055	0.044	0.026	0.005
	GA3121	0.11	0.034	0.0099
	GA3158	0.037	0.026	0.06
	GA3839	0.046	0.026	0.0097

Cancer Type	PDX	λ_0 [1/day] Rate of exponential growth	λ_1 [cm^3/day] Rate of linear growth	W_0 [g] Initial tumor weight
	GA6200	0.048	0.026	0.023
	GA6212	0.048	0.02	0.046
	GA6822	0.03	0.026	0.028
	GA6877	0.051	0.026	0.054
	GA6898	0.042	0.026	0.029
HN	HN0366	0.17	0.075	0.011
	HN0586	0.047	0.065	0.024
	HN0696	0.06	0.039	0.023
	HN1972	0.072	0.065	0.009
	HN2174	0.061	0.074	0.036
	HN2221	0.048	0.065	0.007
	HN2574	0.11	0.07	0.011
	HN2576	0.13	0.057	0.010
	HN2581	0.15	0.071	0.02
	HN2583	0.12	0.074	0.007
	HN2586	0.14	0.082	0.012
	HN2594	0.05	0.065	0.07
	HN2606	0.039	0.065	0.054
	HN3504	0.031	0.065	0.067
	HN3508	0.13	0.063	0.014
	HN3537	0.15	0.081	0.016
	HN3642	0.067	0.065	0.017
	HN3674	0.11	0.066	0.016
	HN3690	0.12	0.061	0.008
	HN3712	0.1	0.064	0.026
	HN3792	0.14	0.076	0.034
	HN3796	0.08	0.065	0.043
	HN5111	0.14	0.051	0.04
	HN5125	0.14	0.075	0.011
	HN5126	0.052	0.065	0.036
LI	LI0050	0.15	0.071	0.008
	LI0348	0.089	0.028	0.024
	LI0612	0.25	0.065	0.002
	LI0801	0.097	0.058	0.024
	LI1005	0.1	0.079	0.013
	LI1025	0.13	0.059	0.01
	LI1035	0.13	0.054	0.004
	LI1037	0.14	0.11	0.001
	LI1054	0.084	0.055	0.014
	LI1055	0.044	0.069	0.014
	LI1058	0.053	0.066	0.006
	LI1069	0.11	0.14	0.008

Cancer Type	PDX	λ_0 [1/day] Rate of exponential growth	λ_1 [cm^3/day] Rate of linear growth	W_0 [g] Initial tumor weight
	LI1074	0.1	0.11	0.04
	LI1078	0.061	0.066	0.028
	LI1081	0.092	0.074	0.009
	LI1097	0.24	0.093	0.006
	LI1098	0.16	0.01	0.019
	LI6206	0.035	0.071	0.013
	LI6280	0.11	0.084	0.023
	LI6281	0.12	0.028	0.015
	LI6605	0.03	0.076	0.026
	LI6610	0.099	0.14	0.002
	LI6611	0.25	0.076	0.007
	LI6612	0.21	0.15	0.006
	LI6664	0.12	0.15	0.036
LU ADC	LU1147	0.064	0.023	0.007
	LU11606	0.077	0.057	0.012
	LU1235	0.093	0.042	0.017
	LU1380	0.092	0.026	0.009
	LU1452	0.033	0.036	0.014
	LU2038	0.039	0.027	0.029
	LU2049	0.043	0.040	0.032
	LU2071	0.053	0.018	0.025
	LU2505	0.053	0.034	0.031
	LU2535	0.029	0.036	0.047
	LU5165	0.064	0.072	0.029
	LU5176	0.076	0.045	0.016
	LU5187	0.055	0.022	0.015
	LU5194	0.042	0.032	0.005
	LU5209	0.028	0.037	0.057
	LU5212	0.090	0.039	0.032
	LU5240	0.033	0.037	0.040
	LU5245	0.070	0.050	0.022
	LU5247	0.069	0.058	0.007
	LU5349	0.145	0.037	0.009
	LU5371	0.035	0.036	0.014
	LU5381	0.135	0.032	0.008
	LU6412	0.048	0.025	0.034
	LU6414	0.183	0.068	0.012
	LU6425	0.205	0.064	0.011
LU SCC	LU0350	0.223	0.078	0.006
	LU0357	0.046	0.073	0.045
	LU0367	0.052	0.030	0.003
	LU0395	0.082	0.031	0.010

Cancer Type	PDX	λ_0 [1/day] Rate of exponential growth	λ_1 [cm^3/day] Rate of linear growth	W_0 [g] Initial tumor weight
	LU0697	0.086	0.018	0.007
	LU0741	0.041	0.014	0.034
	LU0743	0.150	0.095	0.018
	LU0884	0.074	0.051	0.019
	LU1143	0.137	0.058	0.010
	LU1155	0.141	0.019	0.012
	LU1160	0.058	0.096	0.023
	LU1204	0.190	0.115	0.015
	LU1206	0.077	0.048	0.042
	LU1423	0.063	0.030	0.018
	LU1661	0.185	0.054	0.007
	LU1690	0.222	0.044	0.009
	LU1776	0.086	0.024	0.005
	LU3075	0.061	0.023	0.011
	LU6439	0.160	0.087	0.013
	LU6440	0.123	0.106	0.022
	LU6901	0.139	0.036	0.009
	LU6905	0.154	0.048	0.002
	LU6917	0.043	0.023	0.041
	LU9357	0.136	0.092	0.010
	LU9358	0.171	0.061	0.005
ME	ME1154	0.085	0.064	0.022
	ME11971	0.144	0.089	0.009
	ME11972	0.139	0.087	0.009
	ME12047	0.260	0.109	0.004
	ME12056	0.052	0.050	0.030
	ME12057	0.109	0.082	0.023
	ME12068	0.113	0.105	0.014
	ME12070	0.048	0.023	0.008
	ME12079	0.147	0.092	0.018
	ME12080	0.100	0.053	0.032
	ME12107	0.088	0.032	0.025
	ME12120	0.050	0.077	0.027
	ME12149	0.157	0.052	0.006
	ME12172	0.105	0.055	0.009
	ME12208	0.136	0.073	0.011
	ME12212	0.090	0.037	0.030
	ME12216	0.045	0.073	0.023
	ME12217	0.071	0.104	0.027
	ME12222	0.047	0.061	0.019
	ME13996	0.155	0.059	0.007
	ME2194	0.134	0.101	0.006
	ME2319	0.044	0.065	0.042

Cancer Type	PDX	λ_0 [1/day] Rate of exponential growth	λ_1 [cm^3/day] Rate of linear growth	W_0 [g] Initial tumor weight
	ME5285	0.139	0.056	0.014
	ME9384	0.149	0.054	0.008
	MR12035	0.054	0.054	0.021
PA	PA0372	0.011	0.053	0.019
	PA0692	0.081	0.053	0.023
	PA1194	0.045	0.054	0.07
	PA1198	0.08	0.082	0.018
	PA1222	0.038	0.038	0.01
	PA1233	0.051	0.013	0.018
	PA1265	0.13	0.034	0.019
	PA1280	0.092	0.028	0.022
	PA1301	0.095	0.044	0.034
	PA1306	0.084	0.04	0.007
	PA1332	0.21	0.12	0.007
	PA1338	0.14	0.11	0.013
	PA1390	0.09	0.066	0.02
	PA2410	0.08	0.09	0.043
	PA3013	0.093	0.055	0.013
	PA3029	0.098	0.051	0.014
	PA3065	0.12	0.041	0.027
	PA3126	0.1	0.034	0.014
	PA3127	0.062	0.064	0.017
	PA3136	0.12	0.13	0.008
	PA3137	0.095	0.055	0.008
	PA3139	0.09	0.12	0.006
	PA6233	0.055	0.054	0.013
	PA6259	0.098	0.024	0.02
	PA6265	0.075	0.015	0.013
SA	SA0639	0.295	0.125	0.014
	SA10199	0.156	0.239	0.003
	SA13127	0.167	0.081	0.009
	SA13226	0.161	0.046	0.005
	SA13389	0.160	0.169	0.006
	SA3224	0.192	0.160	0.006
	SA3283	0.170	0.142	0.007
	SA3296	0.195	0.309	0.007
	SA3829	0.189	0.148	0.007
	SA3831	0.148	0.059	0.005
	SA4062	0.166	0.217	0.006
	SA4094	0.239	0.096	0.008
	SA4097	0.306	0.275	0.006
	SA4109	0.203	0.082	0.005
	SA4128	0.215	0.269	0.004

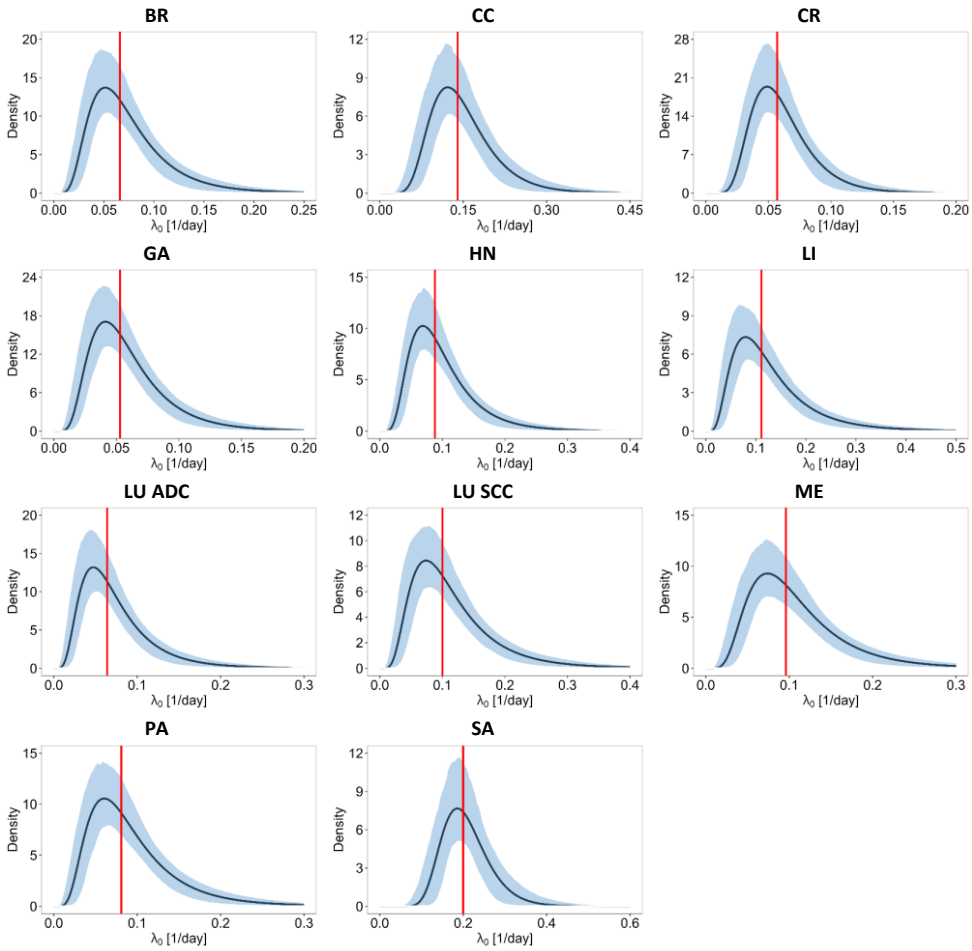

Figure A2 Log-normal distributions of the parameter λ0 of the Simeoni growth model in PDX mice. Black solid lines represent the nominal densities (corresponding to the $\lambda_{0,pop}$ and ω_{λ_0} values reported in Table S3.1). Red vertical line marks the typical (median) value. Blue bands are the 95%PIs of the densities obtained propagating uncertainty of parameter estimates (1000 values of $\lambda_{0,pop}$ and ω_{λ_0} were extracted assuming a normal distribution).

A.6. Scaling of the exponential tumor growth in untreated cancer patients

Table A5 Scaled exponential tumor growth rate in humans

Cancer Type	Log-normal distribution of $k_{g,human}{}^{*}$ [1/month]		Individual $k_{g,Human}$ [1/month] from PDX mouse models				
	$k_{g,human}$ (CV%)**	$\omega_{k_{g,human}}$ (CV%)**					
BR	0.140 (10%)	0.50 (15%)	BR10014 - 0.11	BR10539 - 0.10	BR10582 - 0.13	BR1115 - 0.16	BR1282 - 0.61
			BR1283 - 0.13	BR1458 - 0.24	BR1474 - 0.1	BR2014 - 0.13	BR3267 - 0.09
			BR5009 - 0.09	BR5010 - 0.09	BR5011 - 0.09	BR5013 - 0.1	BR5015 - 0.29
			BR6695 - 0.12	BR9456 - 0.17	BR9464 - 0.12	BR9465 - 0.11	BR9466 - 0.13
			BR9469 - 0.13	BR9479 - 0.13	BR9480 - 0.16	BR9493 - 0.13	BR9494 - 0.47
CC	0.298 (9%)	0.37 (17%)	CC6679 - 0.29	CC6639 - 0.54	CC6638 - 0.34	CC6279 – 0.33	CC6216 – 0.34
			CC0449 - 0.19	CC11307 - 0.21	CC1470 - 0.19	CC6204 - 0.25	CC6205 - 0.29
			CC6600 - 0.17	CC6604 - 0.34	CC6607 - 0.18	CC6609 - 0.33	CC6614 - 0.2
			CC6625 - 0.44	CC6637 - 0.35	CC6645 - 0.30	CC6658 - 0.46	CC6680 – 0.29
			CC6724 - 0.2	CC9326 - 0.28	CC9506 - 0.44	-	-
CR	0.121 (8%)	0.39 (16%)	CR0004 – 0.16	CR0012 – 0.13	CR0150 – 0.13	CR0170 – 0.0.08	CR0193 – 0.22
			CR0196 – 0.13	CR0205 – 0.17	CR1519 – 0.17	CR1801 – 0.11	CR2110 – 0.12
			CR2161 – 0.12	CR2394 – 0.17	CR2517 – 0.09	CR2518 – 0.11	CR2519 – 0.14
			CR2524 – 0.17	CR2814 – 0.09	CR3079 – 0.09	CR3150 – 0.14	CR3315 – 0.15
			CR3496 – 0.11	CR3612 – 0.17	CR6219 – 0.11	CR6227 – 0.08	CR6228 – 0.04
GA	0.113 (10%	0.50 (14%)	GA0006 – 0.19	GA0023 – 0.26	GA0044 – 0.23	GA0046 – 0.17	GA0055 – 0.09
			GA0080 – 0.26	GA0087 – 0.09	GA0095 – 0.04	GA0098 – 0.09	GA0119 – 0.1
			GA0138 – 0.14	GA0151 – 0.06	GA0318 – 0.1	GA0429 – 0.23	GA2101 – 0.09
			GA2278 – 0.1	GA3055 – 0.09	GA3121 - 0.23	GA3158 – 0.08	GA3839 – 0.1

Cancer Type	Log-normal distribution of $k_{g,human}{}^{*}$ [1/month]		Individual $k_{g,Human}$ [1/month] from PDX mouse models				
	$k_{g,human}$ (CV%)**	$\omega_{k_{g,human}}$ (CV%)**					
			GA6200 – 0.1	GA6212 – 0.1	GA6822 – 0.06	GA6877 – 0.11	GA6898 – 0.09
HN	0.188 (10%)	0.50 (15%)	HN0366 - 0.36	HN0586 - 0.1	HN0696 - 0.13	HN1972 - 0.15	HN2174 - 0.13
			HN2221 - 0.1	HN2574 - 0.23	HN2576 - 0.28	HN2581 - 0.32	HN2583 - 0.26
			HN2586 - 0.3	HN2594 - 0.11	HN2606 - 0.08	HN3504 - 0.07	HN3508 - 0.28
			HN2586 - 0.32	HN2594 - 0.14	HN2606 - 0.23	HN3504 - 0.26	HN3508 - 0.21
			HN3792 - 0.3	HN3796 - 0.17	HN5111 - 0.3	HN5125 - 0.3	HN5126 - 0.11
LI	0.236 (12%)	0.58 (15%)	LI0050 - 0.32	LI0348 - 0.19	LI0612 - 0.53	LI0801 - 0.21	LI1005 - 0.21
			LI1025 - 0.28	LI1035 - 0.28	LI1037- 0.3	LI1054 - 0.18	LI1055 - 0.09
			LI1058 - 0.11	LI1069 - 0.23	LI1074 - 0.21	LI1078 - 0.13	LI1081 - 0.2
			LI1097 - 0.51	LI1098 - 0.34	LI6206 - 0.07	LI6280 - 0.23	LI6281 - 0.26
			LI6605 - 0.06	LI6610 - 0.21	LI6611 - 0.53	LI6612 - 0.45	LI6664 - 0.26
LU ADC	0.136 (11%)	0.55 (14%)	LU1147 - 0.14	LU11606 - 0.16	LU1235 - 0.2	LU1380 - 0.2	LU1452 - 0.07
			LU2038 - 0.08	LU2049 - 0.09	LU2071 - 0.11	LU2505 - 0.11	LU2535 - 0.06
			LU5165 - 0.14	LU5176 - 0.16	LU5187 - 0.12	LU5194 - 0.09	LU5209 - 0.06
			LU5212 - 0.19	LU5240 - 0.07	LU5245 - 0.15	LU5247 - 0.15	LU5349 – 0.31
			LU5371 - 0.07	LU5381 - 0.29	LU6412 - 0.1	LU6414 - 0.39	LU6425 - 0.44
LU SCC	0.213 (11%)	0.55 (15%)	LU0350 - 0.47	LU0357-0.1	LU0367- 0.11	LU0395- 0.17	LU0697- 0.18
			LU0741- 0.09	LU0743- 0.32	LU0884- 0.16	LU1143- 0.29	LU1155-0.3
			LU1160- 0.12	LU1204-0.4	LU1206- 0.16	LU1423- 0.13	LU1661- 0.39
			LU1690- 0.47	LU1776- 0.18	LU3075- 0.13	LU6439- 0.34	LU6440- 0.26
			LU6901-0.3	LU6905- 0.33	LU6917- 0.09	LU9357- 0.29	LU9358- 0.36
ME	0.211 (10%)	0.46 (15%)	ME1154- 0.18	ME11971- 0.31	ME11972- 0.3	ME12047- 0.55	ME12056- 0.11

Cancer Type	Log-normal distribution of $k_{g,human}$* [1/month]		Individual $k_{g,Human}$ [1/month] from PDX mouse models				
	$k_{g,human}$ (CV%) **	$\omega_{k_{g,human}}$ (CV%)**					
			ME12057-0.23	ME12068-0.24	ME12070-0.1	ME12079-0.31	ME12080-0.21
			ME12107-0.19	ME12120-0.11	ME12149-0.34	ME12172-0.22	ME12208-0.29
			ME12212-0.19	ME12216-0.1	ME12217-0.15	ME12222-0.1	ME13996-0.33
			ME2194-0.29	ME2319-0.09	ME5285-0.29	ME9384-0.32	ME120350.11
PA	0.172 (11%)	0.54 (15%)	PA0372-0.02	PA0692-0.17	PA1194-0.1	PA1198-0.17	PA1222-0.08
			PA1233-0.11	PA1265-0.28	PA1280-0.2	PA1301-0.2	PA1306-0.18
			PA1332-0.45	PA1338-0.3	PA1390-0.19	PA2410-0.17	PA3013-0.2
			PA3029-0.21	PA3065-0.26	PA3126-0.21	PA3127-0.13	PA3136-0.26
			PA3137-0.2	PA3139-0.19	PA6233-0.12	PA6259-0.21	PA6265-0.16
SA	0.426 (8%)	0.27 (21%)	SA0639-0.63	SA10199-0.33	SA13127-0.36	SA13226-0.34	SA13389-0.34
			SA3224-0.41	SA3283-0.36	SA3296-0.42	SA3829-0.4	SA3831-0.32
			SA4062-0.35	SA4094-0.51	SA4097-0.65	SA4109-0.43	SA4128-0.46
			SA4148-0.71				

Notes: (*) Exponential tumor growth rate was parametrized as $k_{g,Human,i} = k_{g,Human,pop}\ exp(\ \eta_{k_{g,Human},i}\ )$ *where* $k_{g,Human,pop} = \lambda_{0,pop}(BW_{Human}/BW_{Mice})^{-\alpha}$ *was the typical value (median) and* $\eta_{k_{g,Human}}$ *a normally distributed variable with mean zero and standard deviation* $\omega_{k_{g,Human}} = \omega_{\lambda_0}$. *(**) Coefficient of variations (CV%) of the* $k_{g,Human,pop}$ *and* $\omega_{k_{g,Human}}$ *parameters were obtained propagating the estimation uncertainty of the mice-related parameters (i.e.,* $\lambda_{0,pop}$ *and* ω_{λ_0}*).*

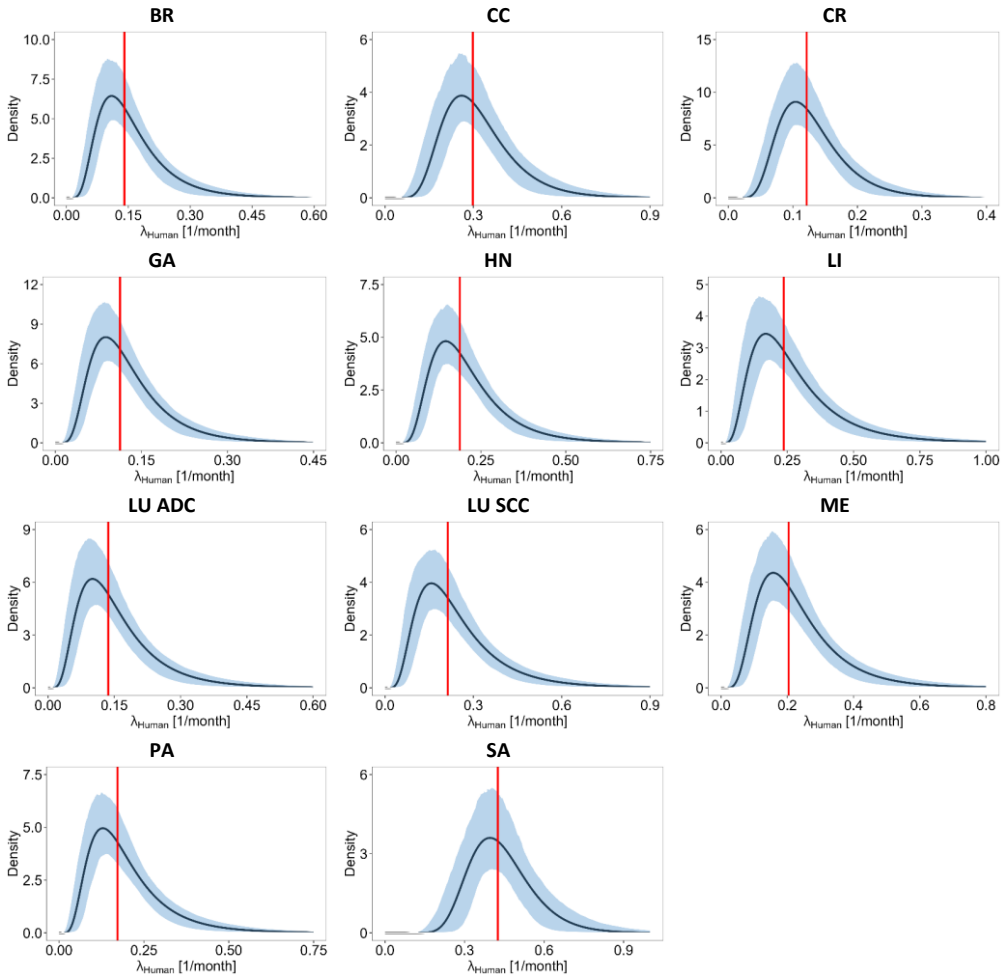

Figure A3 Log-normal distributions of the exponential tumor growth rate in humans, $k_{g,Human}$, scaled from PDX mice. Black solid lines represent the nomial densities (corresponding to the $k_{g,Human,pop}$ and $\omega_{\lambda_{Human}}$ values reported in Table A5). Red vertical lines mark the typical (median) values. Blue bands are the 95%PIs of the densities obtained propagating estimation uncertainty of parameters (1000 values of $k_{g,Human,pop}$ and $\omega_{\lambda_{Human}}$ were extracted assuming a normal distribution).

A.7. Predicting TVDTs and PFS in untreated cancer patients

For each cancer type, the 80%PI of predicted TVDTs and PFS in humans was computed following these steps:

- to account for estimation uncertainty, the parameters characterizing the log-normal distribution of exponential tumor growth rate $k_{g,Human}$ in

cancer patients, i.e., $k_{g,human,pop}$ and $\omega_{k_{g,human}}$, were supposed normally distributed with means equal to values reported in Table A5 and standard deviations derived from the corresponding CV% of estimates (see Table A5);

- from the normal distributions of $k_{g,human,pop}$ and $\omega_{k_{g,human}}$, 1000 samples, $\{k_{g,human,pop,i}\}_{i=1,\dots1000}$ and $\{\omega_{k_{g,human},i}\}_{i=1,\dots1000}$, were extracted, thus obtaining 1000 log-normal distributions of $k_{g,human}$ in cancer patients each characterized by a couple $(k_{g,human,pop,i}, \omega_{k_{g,human,i}})$;
- TVDTs:
    - from the 1000 log-normal distributions of $k_{g,human}$ the corresponding 1000 log-normal distributions of $TVDT_{human}$ were derived, applying Eq. 2;
    - for each of the 1000 log-normal distributions of $TVDT_{human}$, the 10th and 90th percentiles (p10 and p90) were computed;
    - the 80%PI of predicted TVDTs was defined as the 2.5th percentile of p10 and 97.5th percentile of p80 to include both the inter-patient variability and the parameter estimation uncertainty.
- PFS:
    - 200 growth rates (=patients) from each log-normal distribution were sampled and the corresponding t_{event} derived, applying Eq. 3;
    - 1000 KM curve for PFS were derived and KM – visual predictive checks (VPC) constructed.

Table A6 Predicted TVDTs in humans.

Cancer Type	Log-normal distribution of $TVDT_{human}$ [month]*		Individual $TVDT_{human}$ [month] from PDX mouse models				
	$TVDT_{human}$ (CV%)	$\omega_{TVDT_{Human}}$ (CV%)					
BR	4.93 (10%)	0.50 (15%)	BR10014 – 6.46	BR10539 – 6.6	BR10582 – 5.41	BR1115 – 4.32	BR1282 – 1.14
			BR1283 – 5.35	BR1458 – 2.93	BR1474 – 6.6	BR2014 – 5.48	BR3267 – 7.51

			BR5009 – 7.76	BR5010 – 8.09	BR5011 – 8.07	BR5013 – 6.67	BR5015 – 2.4
			BR6695 – 5.69	BR9456 – 4.18	BR9464 - 5.6	BR9465 – 6.59	BR9466 – 5.34
			BR9469 – 5.41	BR9479 – 5.23	BR9480 - 4.23	BR9493 – 5.36	BR9494 – 1.47
CC	2.33 (9%)	0.37 (17%)	CC6679 - 2.41	CC6639 - 1.27	CC6638 - 2.04	CC6279 - 2.13	CC6216 - 2.06
			CC0449 - 3.7	CC11307 - 3.36	CC1470 – 3.7	CC6204 – 2.76	CC6205 – 2.36
			CC6600 – 4.18	CC6604 – 2.01	CC6607 – 3.92	CC6609 – 2.1	CC6614 – 3.54
			CC6625 – 1.59	CC6637 – 1.96	CC6645 – 2.33	CC6658 – 1.51	CC6680 – 2.41
			CC6724 – 3.43	CC9326 – 2.51	CC9506 – 1.57	-	-
CR	5.71 (9%)	0.39 (16%)	CR0004 – 4.23	CR0012 – 5.17	CR0150 – 5.17	CR0170 – 9.05	CR0193 – 3.1
			CR0196 – 5.43	CR0205 – 4.07	CR1519 – 4.12	CR1801 – 6.39	CR2110 – 5.82
			CR2161 – 5.82	CR2394 – 4.07	CR2517 – 7.4	CR2518 – 6.51	CR2519 – 5.09
			CR2524 – 4.02	CR2814 – 7.75	CR3079 – 8.14	CR3150 – 5.01	CR3315 – 4.59
			CR3496 – 6.14	CR3612 – 4.07	CR621 – 6.14	CR6227 – 8.35	CR622 – 19.16
GA	6.14 (10%)	0.50 (14%)	GA0006 - 3.62	GA0023 - 2.71	GA0044 - 2.96	GA0046 - 3.97	GA0055 - 7.57
			GA0080 - 2.71	GA0087 - 8.14	GA0095 - 18.09	GA0098 - 7.57	GA0119 - 7.24
			GA0138 - 5.09	GA0151 - 10.86	GA0318 - 7.08	GA0429 - 2.96	GA2101 - 7.57
			GA2278 - 6.93	GA3055 - 7.4	GA3121 - 2.96	GA3158 - 8.8	GA3839 - 7.08
			GA6200 - 6.78	GA6212 - 6.78	GA6822 - 10.86	GA6877 - 6.39	GA6898 - 7.75
HN	3.69 (10%)	0.50 (15%)	HN0366 - 1.92	HN0586 - 6.93	HN0696 - 5.43	HN1972 - 4.52	HN2174 - 5.34
			HN2221 - 6.78	HN2574 - 2.96	HN2576 - 2.51	HN2581 - 2.17	HN2583 - 2.71
			HN2586 - 2.33	HN2594 - 6.51	HN2606 - 8.35	HN3504 - 10.5	HN3508 - 2.51
			HN2586 - 2.17	HN2594 - 4.86	HN2606 - 2.96	HN3504 - 2.71	HN3508 - 3.26
			HN3792 - 2.33	HN3796 - 4.07	HN5111 - 2.33	HN5125 - 2.33	HN5126 - 6.26
LI	2.93 (12%)	0.58 (15%)	LI0050 - 2.17	LI0348 - 3.66	LI0612 -. 1.3	LI0801 - 3.36	LI1005 - 3.26
			LI1025 - 2.51	LI1035 - 2.51	LI1037 - 2.33	LI1054 - 3.88	LI1055 - 7.4

			LI1058 - 6.14	LI1069 - 2.96	LI1074 - 3.26	LI1078 - 5.34	LI1081 - 3.54
			LI1097 - 1.36	LI1098 - 2.04	LI6206 - 9.3	LI6280 - 2.96	LI6281 - 2.71
			LI6605 - 10.86	LI6610 - 3.29	LI6611 - 1.3	LI6612 - 1.55	LI6664 - 2.71
LU ADC	5.09 (12%)	0.55 (14%)	LU1147 - 5.09	LU11606 - 4.23	LU1235 - 3.5	LU1380 - 3.54	LU1452 - 9.87
			LU2038 - 8.35	LU2049 - 7.57	LU2071 - 6.14	LU2505 - 6.14	LU2535 - 11.23
			LU5165 - 5.09	LU5176 - 4.28	LU5187 - 5.92	LU5194 - 7.75	LU5209 - 11.63
			LU5212 - 3.62	LU5240 - 9.87	LU5245 - 4.65	LU5247 - 4.72	LU5349 - 2.25
			LU5371 - 9.3	LU5381 - 2.41	LU6412 - 6.78	LU6414 - 1.78	LU6425 - 1.59
LU SCC	3.26 (12%)	0.55 (15%)	LU0350-1.46	LU0357-7.08	LU0367-6.26	LU0395-3.97	LU0697-3.79
			LU0741-7.94	LU0743-2.17	LU0884-4.4	LU1143-2.38	LU1155-2.31
			LU1160-5.61	LU1204-1.71	LU1206-4.23	LU1423-5.17	LU1661-1.76
			LU1690-1.47	LU1776-3.79	LU3075-5.34	LU6439-2.04	LU6440-2.65
			LU6901-2.34	LU6905-2.11	LU6917-7.57	LU9357-2.39	LU9358-1.9
ME	3.29 (10%)	0.46 (15%)	ME1154-3.85	ME11971-2.26	ME11972-2.34	ME12047-1.25	ME12056-6.22
			ME12057-2.98	ME12068-2.89	ME12070-6.85	ME12079-2.22	ME12080-3.26
			ME12107-3.69	ME12120-6.55	ME12149-2.07	ME12172-3.11	ME12208-2.4
			ME12212-3.61	ME12216-7.25	ME12217-4.6	ME12222-6.87	ME13996-2.11
			ME2194-2.42	ME2319-7.47	ME5285-2.35	ME9384-2.19	ME12035-6.04
PA	4.02 (11.3)	0.54 (15%)	PA0372-29.6	PA0692-4.02	PA1194-7.24	PA1198-4.07	PA1222-8.57
			PA1233-6.39	PA1265-2.51	PA1280-3.54	PA1301-3.43	PA1306-3.88
			PA1332-1.55	PA1338-2.33	PA1390-3.62	PA2410-4.07	PA3013-3.5
			PA3029-3.32	PA3065-2.71	PA3126-3.26	PA3127-5.25	PA3136-2.71
			PA3137-3.43	PA3139-3.62	PA6233-5.92	PA6259-3.32	PA6265-4.34
SA	1.63 (8%)	0.27 (21%)	SA0639-1.1	SA10199-2.09	SA13127-1.95	SA13226-2.02	SA13389-2.04
			SA3224-1.7	SA3283-1.92	SA3296-1.67	SA3829-1.72	SA3831-2.2
			SA4062-1.96	SA4094-1.36	SA4097-1.06	SA4109-1.6	SA4128-1.51

			SA4148-0.98				

Notes: (*) Distribution of TVDT was parametrized as $TVDT = TVDT_{human,pop}\, exp(\eta_{TVDT_{human},i})$ *where* $TVDT_{human,pop}$ *was the typical value (median) and* $\eta_{TVDT_{human}}$ *a normally distributed variable with mean zero and standard deviation* $\omega_{TVDT_{human}} = \omega_{\lambda_0}$. *(**) Coefficient of variations (CV%) of the* $TVDT_{human,pop}$ *and* $\omega_{TVDT_{human}}$ *parameters were obtained propagating the estimation uncertainty of the mice-related parameters (i.e.,* $\lambda_{0,pop}$ *and* ω_{λ_0}*).*

A.8. Predicting TVDTs and PFS in untreated cancer patients

Table A7 Estimates of the allometric scaling exponents α

Cancer type	α estimate	SE
All the 11 cancer types	0.3446	0.0074
BR	0.3506	-
CC	0.3335	-
CR	0.3420	-
GA	0.3753	-
HN	0.3068	-
LI	0.3451	-
LU ADC	0.3436	-
LU SCC	0.3410	-
ME	0.3232	-
PA	0.3242	-
SA	0.1070	-

Appendix B

Supplementary material for Chapter 3

B.1. Complete List of the analyzed PDX experiments

Table B1 Considered TGI studies in pancreatic cancer PDX mouse models. For each PDX mouse model, a single TGI study including one control arm, and one Gemcitabine arm was available.

PDX code*	Administration schedule	Route of administration	Dose	Patient ethnicity
PA0527	Q4D x 4	Intra-peritoneal	120	Asian
PA0692	Q3D x 21	Intra-peritoneal	60	Asian
PA1170	Day1,5/wk x 3.5wks	Intra-peritoneal	40	Asian
PA1178	Day1,4/wk x 3wks	Intra-peritoneal	40	Asian
PA1189	Day1,4/wk x 3.5wks	Intra-peritoneal	40	Asian
PA1194	Q3D x 7	Intra-peritoneal	60	Asian
PA1198	Q3D x 16	Intra-peritoneal	60	Asian
PA1266	Day1,4/wk x 3wks	Intra-peritoneal	40	Asian
PA1280	Q4D x 4	Intra-peritoneal	60	Asian
PA1301	Q3D x 14	Intra-peritoneal	120	Asian
PA1332	Q4D x 6	Intra-peritoneal	15	Asian
PA1338	Q3D x 21	Intra-peritoneal	60	Asian
PA1383	Day0,4,8,Day12,Day16,20,24,28	Intra-venous	60	Asian
PA1390	Day3,7,11,15	Intra-peritoneal	60	Asian
PA3029	Q3D x 9	Intra-peritoneal	120	Asian
PA3065	Q4D x 4	Intra-peritoneal	60	Asian
PA3137	Day1,4/wk x 3wks	Intra-peritoneal	40	Asian
PA3139	Day1,4/wk x 3wks	Intra-peritoneal	40	Asian
PA6259	Day1,4/wk x 3wks	Intra-peritoneal	60	Asian
PA6265	Day1,4/wk x 5wks	Intra-peritoneal	40	Asian
PA1168	Q3Dx6	Intra-peritoneal	100	Asian
PA1222	QW x 2wks	Intra-peritoneal	120	Asian

PA1233	Q4Dx4	Intra-peritoneal	60	Asian
PA1265	QW x 2wks	Intra-peritoneal	120	Asian
PA1644	Day1,4/wk x 2.5wks	Intra-peritoneal	40	Asian
PA3013	Day1,4/wk x 2wks	Intra-peritoneal	40	Asian
PA3126	Q4D x 6	Intra-peritoneal	15	Asian
PA3149	Day1,4/wk x 2wks	Intra-peritoneal	120	Asian
PA6233	QW x 2wks	Intra-peritoneal	120	Asian

Notes: PDX codes from HuBase database (Crownbio Bioscience Inc., https://www.crownbio.com/). List of abbreviations: QaD x b: dose administered once every a days for b times. Day X,Y/wk x Zwks: dose administered on days X and Y every week for Z weeks.

Table B2 Considered TGI studies in hepatocellular cancer PDX mouse models. For each PDX mouse model, a single TGI study including one control arm and one Sorafenib arm was available.

PDX code*	Administration schedule	Route of administration	Dose	Origin
LI0050	QDx12	Oral	50	Asian
LI0334	QDx50	Oral	50	Asian
LI0348	QDx21	Oral	50	Asian
LI0574	QDx14	Oral	50	Asian
LI0612	QDx12	Oral	60	Asian
LI0752	QDx17	Oral	50	Asian
LI0801	QDx22	Oral	50	Asian
LI0941	Day1-5/wk x 2wks	Oral	50	Asian
LI1005	QDx14	Oral	30	Asian
LI1025	QDx21	Oral	50	Asian
LI1035	QDx21	Oral	50	Asian
LI1054	QDx14	Oral	50	Asian
LI1057	QDx14	Oral	50	Asian
LI1068	QDx13	Oral	50	Asian
LI1069	QDx14	Oral	50	Asian
LI1074	QDx13	Oral	50	Asian
LI1078	QDx21	Oral	50	Asian
LI1081	QDx21	Oral	50	Asian
LI1088	QDx13	Oral	50	Asian
LI1097	QDx14	Oral	50	Asian
LI1098	QDx14	Oral	50	Asian
LI1646	QDx21	Oral	50	Asian
LI6206	QDx21	Oral	50	Asian
LI6664	QDx21	Oral	50	Asian

Notes: PDX codes from HuBase database (Crownbio Bioscience Inc., https://www.crownbio.com/). List of abbreviations: QaD x b: dose administered once every a days for b times. Day X,Y/wk x Zwks: dose administered on days X and Y every week for Z weeks.

B.2. Mice PK models

B.2.1 Pharmacokinetic compartment model of i.p. administration of Gemcitabine in mice.

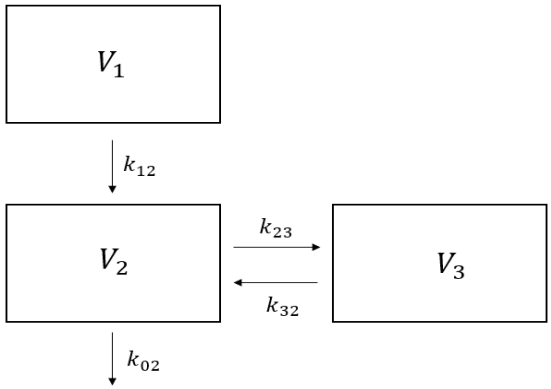

Figure B1 Mice PK 2-compartment model with absorption: diagram.

Table B3 Mice PK model: parameters.

Parameter	Value
$V_2[ml * kg^{-1}]$	887.2
$k_{12}[day^{-1}]$	92.272
$k_{32}[day^{-1}]$	20.376
$k_{23}[day^{-1}]$	45.192
$k_{02}[day^{-1}]$	177.12
$F[-]$	1

B.2.2. Pharmacokinetic compartment model of oral administration of Sorafenib in mice.

Table B4 Mice PK model: parameters.

Parameter	Value
$V_c[l]$	0.0112
$V_p[l]$	0.0120
$k_{12}[hour^{-1}]$	0.663

$k_{21}[hour^{-1}]$	0.620
$k_e[hour^{-1}]$	0.334
$k_a[hour^{-1}]$	0.640

B.3 Model fitting of preclinical TGI studies

B.3.1 Pancreatic cancer PDX treated with Gemcitabine

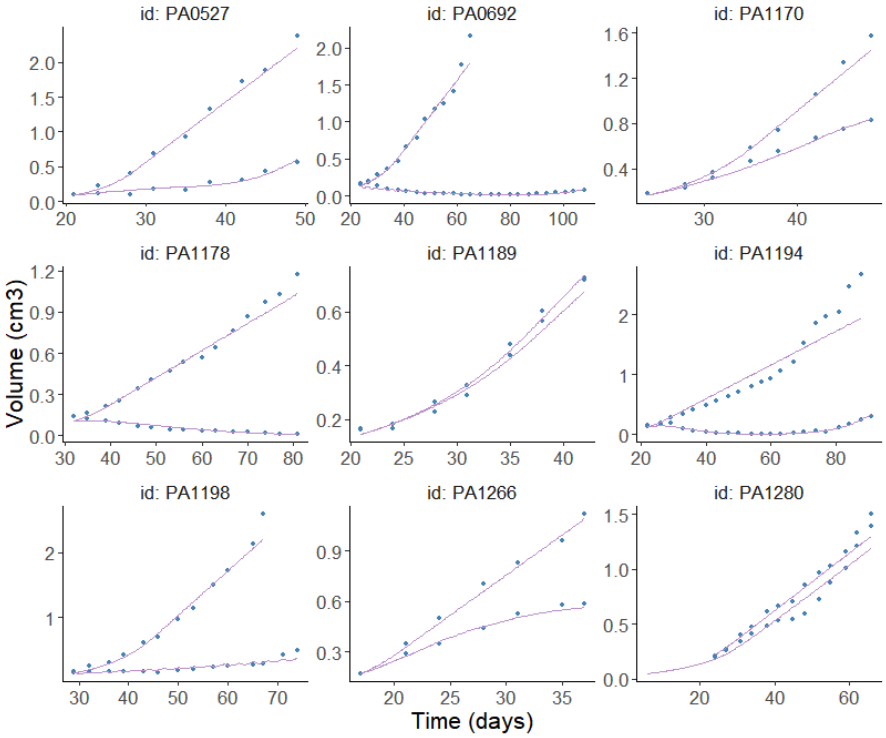

Figure B2 Individual fit plots for a subset of 9 TGI studies in 9 PDX mouse models of pancreatic cancer. In each panel, both the control arm and the Gemcitabine one is shown.

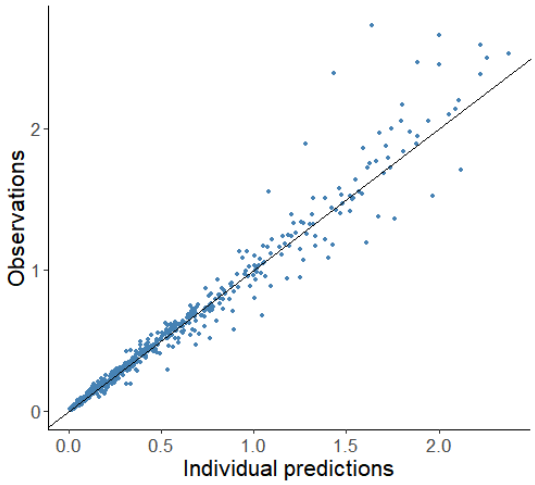

Figure B3 Individual Prediction vs Observations.

B.3.2 Hepatocellular cancer PDX treated with Sorafenib

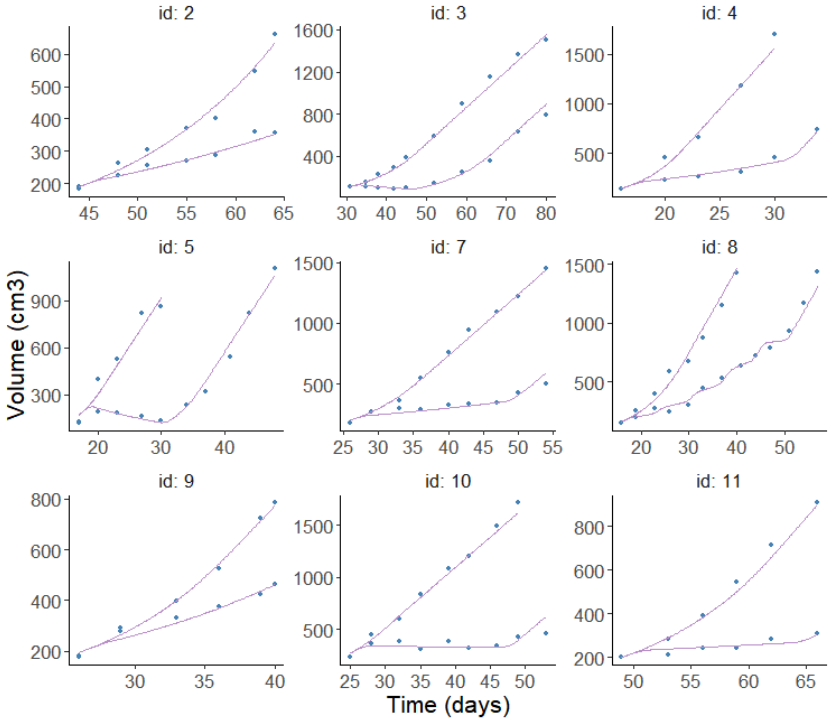

Figure B4 Individual fits for a subset of 9 PDX liver cancer model. In each panel, both the control arm and the Sorafenib one is shown.

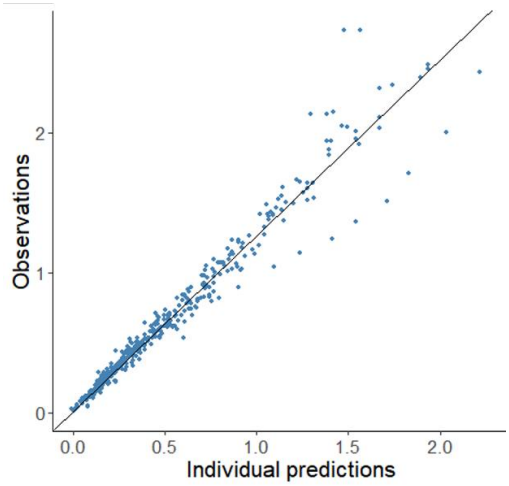

Figure B4 Individual Prediction vs Observations.

B.4. Time-to-event model building for OS

B.4.1. Gemcitabine treatment of pancreatic cancer

For the considered clinal studies (Table 3.1 of the main test), the times at which the OS probability is equal to 0.75, 0.5 and 0.25 are reported below.

Table B5 Summary statistics of the OS probability – Gemcitabine treatment of pancreatic cancer case study

Reference	Number of patients	Time at which OS=0.75 [months]	Median OS time [months]	Time at which OS=0.25 [months]
Hong	56	4.8	8.9	12.7
Kindler	316	4.5	8.3	11.2
Nakai	53	3.9	8.8	14.3
Ozaka	59	5.2	8.0	16.5

Seven different hazard functions have been fitted on the digitalized OS data from the study with the greatest number of patients [Kindler et al.]. Then, the best fitted model (in terms of AIC) has been selected to describe the OS curve.

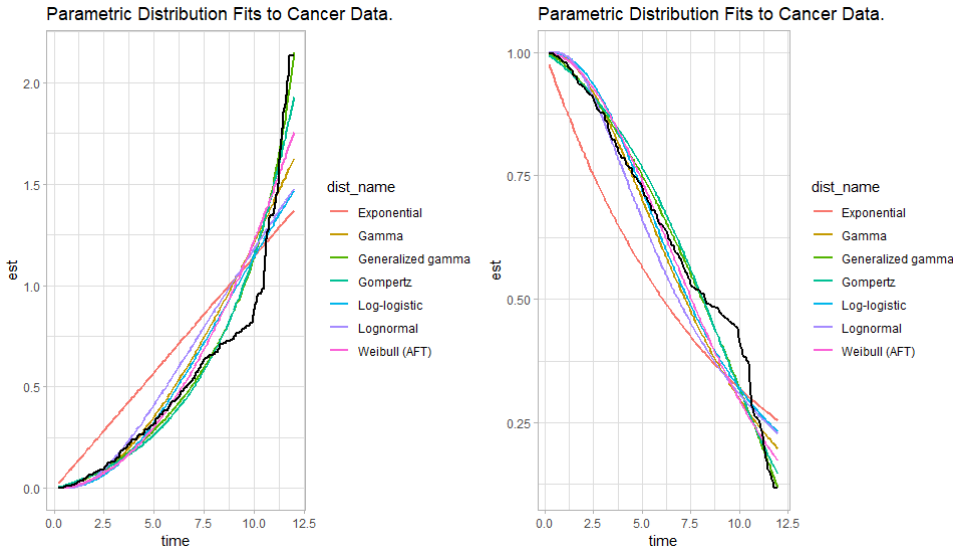

Figure B5 In the right panel, the cumulative observed hazard ratio (black) and the fitted cumulative hazard ratio (colored lines). In the left panel, the observed survival (black) and the fitted survival (colored lines).

Table B6 AIC of different TTE models for OS

Distribution	AIC
Generalized gamma	1587.415
Gompertz	1607.404
Weibull	1634.517
Gamma	1657.770
Log-logistic	1689.091
Lognormal	1710.036
Exponential	1770.423

The model selected to describe the hazard function is the generalized gamma function.

Table B7 Estimated parameters of the best-fitted time to event model.

Parameter	Estimate
mu	2.4918
sigma	0.1442
Q	4.7991

B.4.2. Sorafenib treatment of hepatocellular cancer

For the considered clinal studies (Table 3.2 of the main test), the times at which the OS probability is equal to 0.75, 0.5 and 0.25 are reported below.

Table B8 Summary statistics of the OS probability – Sorafenib treatment of hepatocellular cancer case study

Reference	Number of patients	0.25-quantile OS time [months]	Median OS time [months]	0.75-quantile OS time [months]
Park	169	6.1	10.8	21.2
Qin	331	5.6	10.3	19.8
Kudo	103	5.8	11.5	24.8
Lyu	132	4.8	8.2	12.9

Seven different hazard functions have been fitted on the digitalized OS data from the study with the greatest number of patients [Qin et al.]. Then, the best fitted model (in terms of AIC) has been selected to describe the OS curve.

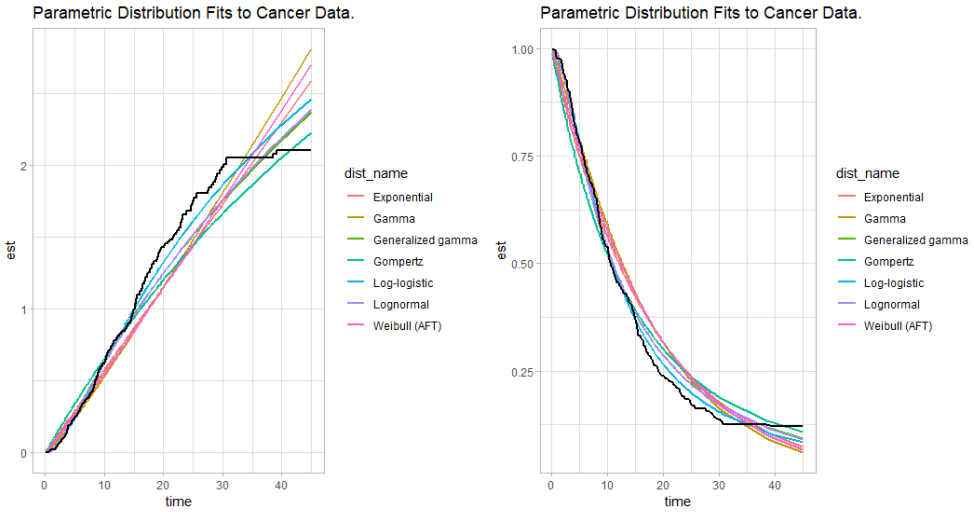

Figure B6 In the right panel, the cumulative observed hazard ratio (black) and the fitted cumulative hazard ratio (colored lines). In the left panel, the observed survival (black) and the fitted survival (colored lines).

Table B9 AIC of different TTE models for OS

Distributions	AIC
Log-logistic	2193.399
Lognormal	2202.742
Generalized gamma	2204.675
Gompertz	2237.239
Gamma	2240.992
Exponential	2245.322
Weibull	2246.040

The model selected to describe the hazard function is the log logistic function.

Table B10 Estimated parameters of the best-fitted time to event model.

Parameter	Estimates
shape	1.672
scale	10.851

B.5. Monte Carlo simulation procedure

For both the case studies, the following Monte Carlo simulation procedure was applied:

- to account for estimation uncertainty, parameters characterizing the $\lambda_0 - k_2$ log-normal distribution in mice, i.e., $(\lambda_{0,pop}, k_{2,pop}, \omega_{\lambda_0}, \omega_{k_2}, \omega_{\lambda_{0,}k_2})$, were assumed to follow a multivariate normal distribution, $N(\mu,\Sigma)$, where μ is the vector of parameter estimates obtained by identifying the Simeoni TGI model on PDX mice data and Σ the covariance matrix of the estimates;
- from the previous multivariate normal distribution, 1000 samples, $\{\lambda_{0,pop,j}, k_{2,pop,j}, \omega_{\lambda_{0,}j}, \omega_{k_2,j}, \omega_{\lambda_{0,}k_2,j}\}_{j=1\ldots1000}$ were extracted, thus obtaining 1000 $\lambda_0 - k_2$ log-normal distributions in mice;
- the 1000 $\lambda_0 - k_2$ log-normal distribution in mice were scaled to human according to Eq.5 of the main text, thus obtaining 1000 $k_{g,human} - k_{d,human}$ log-normal distributions;
- from each of the $k_{g,human} - k_{d,human}$ log-normal distributions a cohort of N=200 virtual cancer patients were generated.

Overall, 1000 cohorts each composed by 200 virtual patients were generated accounting for parameter estimation uncertainty.

B.5.1. Predictive Intervals of Tumor growth

For each patient cohort, individual trajectories of tumor volume were simulated on a dense grid of time points and then, converted in terms of tumor diameter using Eq.2. The median, the 5th and 95th percentiles $(p^{0.05}, p^{0.5}, p^{0.95})$ of tumor diameter trajectories among the 200 virtual patients were computed. Finally, the median and the 90% confidence interval (90%CI) of $p^{0.05}, p^{0.5}, p^{0.95}$ among the 1000 replicates in the 1000 virtual patients cohorts were considered.

B.5.2. Predictive Intervals of KM curves

For each virtual patient in each of the 1000 patient cohorts, the time to PFS events (i.e., PD or death which occurs first) was derived as detailed in the main text. Then, for each patient cohort, the KM estimator of PFS probability, $S(t)$, was computed together with its 90%CI, i.e., $\left(L(t),\ U(t)\right)$ which defined as:

$$L(t) = S(t)e^{\frac{z_{0.05}}{\ln(S(t))}\cdot\frac{SE(t)}{S(t)}} \quad \text{and} \quad U(t) = S(t)e^{\frac{-z_{0.05}}{\ln(S(t))}\cdot\frac{SE(t)}{S(t)}}$$

where $z_{0.05}$ was the 5th percentile of the normal distribution and $SE(t) = \sqrt{S(t)(1-S(t))/N}$ with N=200 the size of patient cohort, approximated the standard error of $S(t)$.

In this way, 1000 PFS curves, one for each patient cohort, were obtained. The median of $S(t)$, the 5th percentile of $L(t)$ and the 95th percentile of $U(t)$ among the 1000 patient cohorts, were finally considered.

B.6. PFS prediction ignoring death events

B.6.1. Gemcitabine treatment of pancreatic cancer

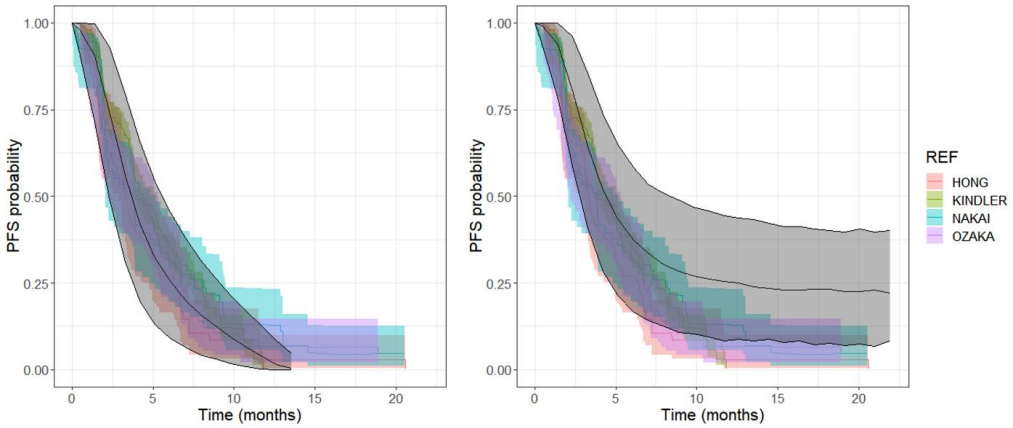

Figure B7 KM-VPC plots (grey areas) generated from 1000 virtual clinical trials composed of 200 pancreatic cancer patients treated the standard gemcitabine schedule for 24 months were superimposed to PFS curves taken from literature studies (colored areas). In the left panel, both the progression events and deaths were included. In the right panel PFS, curves were predicted including only progression events. Solid lines depict the 0.05-quantile, median, and 0.95-quantile of PFS.

B.6.2. Sorafenib treatment of hepatocellular cancer

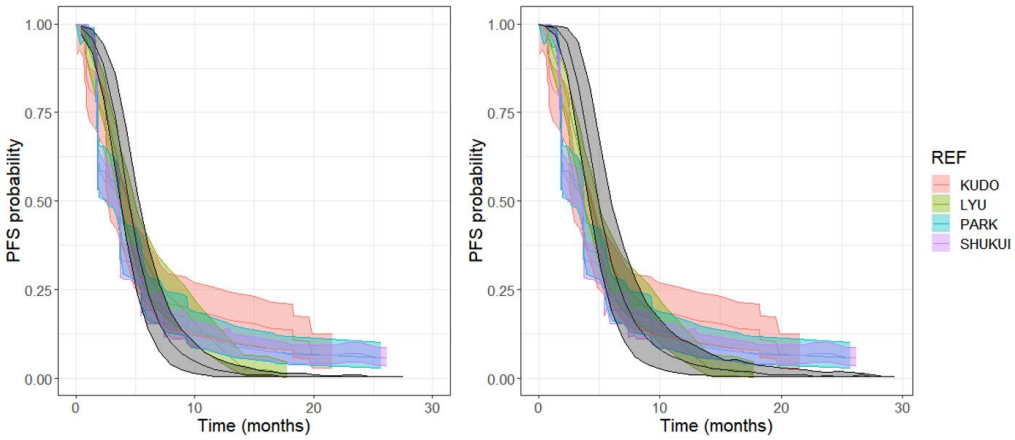

Figure B8 KM-VPC plots (grey areas) generated from 1000 virtual clinical trials composed of 200 hepatocellular cancer patients treated the standard sorafenib schedule for 24 months were superimposed to PFS curves taken from literature studies (colored areas). In the left panel, both the progression events and deaths were included. In the right panel PFS, curves were predicted including only progression events. Solid lines depict the 0.05-quantile, median, and 0.95-quantile of PFS.

Appendix C

Supplementary material for Chapter 4

C.1. From digitized PFS curves to TTE data

The process of converting digitized PFS curves into individual TTE data involves several key steps. The aim is to reconstruct the PFS times for individual patients based on the digitized curve data from published Kaplan-Meier curves.

Step 1: Digitization of Kaplan-Meier curves

The first step in the process is to digitize the Kaplan-Meier curves from the referenced papers. This involves extracting pairs of coordinates $\big(t, S(t)\big)$, where:

- t represents the time point on the x-axis (usually in months or years),
- $S(t)$ represents the estimated survival probability at time t, i.e., the proportion of patients who have not experienced the progression of the disease.

To achieve this, the curves are digitized using WebPlotDigitizer (https://apps.automeris.io/wpd4/) that allows for precise extraction of the $\big(t, S(t)\big)$ coordinates from the graphical representation of the curves. The digitization process is as precise as possible, capturing all relevant points on the curve, including the time points where there are drops in the survival probability $S(t)$.

Step 2: Determining the initial number of patients at risk

After digitizing the curve, the number of patients at risk at time $t = 0$ is extracted from the article. Let N_0 be the initial number of patients at risk.

Step 3: Estimating the number of events at each time point

The number of events between two consecutive time points t_i and t_{i+1} is estimated based on the change in the survival probability.

For each pair of consecutive time points $\big(t_i, S(t_i)\big)$ and $\big(t_{i+1}, S(t_{i+1})\big)$ the number of events d_i that occurred between t_i and t_{i+1} can be approximated using the following formula:

$$d_i = N_i \times \big(S(t_i) - S(t_{i+1})\big)$$

where N_i is the number of patients at risk just before time t_i.

Step 4: Updating the number of patients at risk

Once the number of events d_i is estimated for the interval $[t_i, t_{i+1}]$ the number of patients at risk for the next time point t_{i+1} can be updated:

$$N_{i+1} = N_i - d_i$$

Step 5: Reconstructing individual time-to-event data

With the estimated number of events d_i at each time point and the updated number of patients at risk N_i, the time-to-event data for individual patients can be reconstructed.

For each timepoint t_i, randomly assign the d_i events across the interval $[t_i, t_{i+1}]$.

Appendix D

Supplementary material for Chapter 5

D.1. Data management of NCT00699374 clinical trial

When downloading the .zip file from the Project Data Sphere website, the directory contained various .sas7bdat files. The four data files used in this analysis were: 'demog.sas7bdat,' which contains demographic information of the study population; 'tmm_p.sas7bdat,' which includes individual tumor lesion data; 'testdrug.sas7bdat,' which provides details on drug scheduling; and 'srv_p.sas7bdat,' which contains survival information.

First, the patient population was narrowed down to include only Asian patients (from 544 to 417). Next, tumor measurements labeled as 'TOO SMALL TO MEASURE' were categorized as 'under the limit of quantification.' If the measurement was labeled as 'INDEFINITE,' it was treated as missing data. After this, one patient with unrealistic tumor measurements (each lesion had a baseline size greater than 60 cm) was excluded from the study. Finally, underrepresented tumor locations were re-labeled as 'other' for modeling purposes.

The 'testdrug.sas7bdat' data file was then used to create a Simulx-compatible file for simulating individual Sorafenib plasma concentration profiles.

D.2. Adapting the Volumetric TGI Model to Describe Tumor Diameter Data

Assuming that the tumor grows uniformly in all dimensions, the tumor volume $TV(t)$ can be expressed as $a \times \mathrm{TS}^3(t)$, where $TS(t)$ represents tumor's diameter trajectory over time, and a is a proportionality constant. By substituting this expression into Equation 9, we obtain:

$$a \times \frac{d\left(TS^3(t)\right)}{dt} = \left(k_{g,human} - k_{d,human} \cdot c(t)\right) \times \left(a \times TS^3(t)\right) \quad \text{(D1)}$$

Applying the chain rule to the left side, we have:

$$3 \times TS^2(t) \times \frac{dTS(t)}{dt} = \left(k_{g,human} - k_{d,human} \cdot c(t)\right) \times TS^3(t) \quad \text{(D2)}$$

Dividing both sides by $3 \times TS^2(t)$, we simplify to find the relationship for the tumor's diameter over time:

$$\frac{dTS(t)}{dt} = \left(\frac{k_{g,human}}{3} - \frac{k_{d,human}}{3} \cdot c(t)\right) \cdot TS(t) \quad \text{(D3)}$$

Where:

$$\begin{aligned} k'_{g,human} &\sim Lognormal\left(\theta_{k'_{g,human}} = \frac{\theta_{k_{g,human}}}{3}, \omega_{k'_{g,human}} = \omega_{k_{g,human}}\right) \\ k'_{d,human} &\sim Lognormal\left(\theta_{k'_{d,human}} = \frac{\theta_{k_{d,human}}}{3}, \omega_{k'_{d,human}} = \omega_{k_{d,human}}\right) \end{aligned} \quad \text{(D4)}$$

D.3. Posterior Predictive Checks

Posterior predictive checks (PPCs) rely on the visual comparison of the original dataset with many replicated data generated under the selected model. We replicated B = 4000 datasets using the following procedure. For each replicated dataset b, we drew a vector of population parameters in the posterior distribution $\theta_b \sim p(\theta|y, T, \delta)$ and we sampled the random effects of each replicated lesion k from organ j of each replicated patient i in their distributions $\eta_i^b \sim N(0, \Omega_1^b)$ and $\rho_{i,j,k}^b \sim N(0, \Omega_2^b)$. The individual parameters vector of patient i ψ_i^b was then computed as function of θ^b, η_i^b and $\rho_{i,j,k}^b$ following definition of individual parameters in the main

manuscript. Following study protocol, for each theoretical measurement time t_l, we derived the simulated trajectory of the lesion, drawing $y^b_{i,j,k,l} \sim p^L(y_{i,j,k,l}|\boldsymbol{\theta_b}, \boldsymbol{\psi^b_{i,j,k}})$, and we sampled a time-to-death $T^b_i \sim p^S(T_i|\boldsymbol{\theta_b}, \boldsymbol{\psi^b_{i,j,k}})$. To be consistent with study protocol, we assumed that SLD was no longer measured in case of progression defined by an increase of more than 20% and more than 5 mm from nadir. We used the 2.5th and 97.5th percentiles of the medians over the B replicated datasets to provide 95% prediction intervals and we compared this prediction with the median of the lesion measurements in the original dataset.

D.4. Accounting for the limit of quantification

The lesion measurements below the limit of quantification loq were considered as left-censored in the longitudinal density, and we used the method developed by Jacqmin-Gadda et al. [203] to consider their contribution to the likelihood. Thus, we denoted $\Delta_{i,j,k,l}$ the left-censor indicator that is 1 if the l^{th} measurement of lesion k in location j in patient i is left-censored, 0 if it is not, and the density of longitudinal data p^L is defined as follows:

$$p^L(y_{i,j,k,l}|\boldsymbol{\theta}, \boldsymbol{\psi_{i,j,k}}) = g_{i,j,k,l}(y_{i,j,k,l}|\boldsymbol{\theta}, \boldsymbol{\psi_{i,j,k}})\,(1 - \Delta_{i,j,k,l}) + \Phi_{i,j,k,l}(loq|\boldsymbol{\theta}, \boldsymbol{\psi_{i,j,k}})\,)\Delta_{i,j,k,l}$$

where $g_{i,j,k,l}$ is the probability density and $\Phi_{i,j,k,l}$ the distribution function of a normal distribution with expectation $TS(t_{i,j,k,l}, \boldsymbol{\psi_{i,j,k}})$ and variance $\sigma_1 + \sigma_2 \times TS(t_{i,j,k,l}, \boldsymbol{\psi_{i,j,k}})$, evaluated in $y_{i,j,k,l}$.

D.5. Reference joint model for sum of the longest diameters and survival

Prior to the joint model for the individual lesion diameters, a reference joint model for sum of the longest diameters and survival has been developed. This simpler model helped informing and setting the more complicated one.

D.5.1. Definition

In this model, only the measurements of the SLD of the target lesions were fitted for the longitudinal part. Denoting $z_{i,l}$ the l-th measurement of SLD for patient i measured at time $t_{i,l}$:

$$z_{i,l} = TS(t_{i,l}, \boldsymbol{\psi_i}) + \left(\sigma_1 + \sigma_2 \times TS(t_{i,l}, \boldsymbol{\psi_i})\right) \times e_{i,l}$$

with $TS(.)$ the longitudinal model presented in Eq. 9. Formally, for each biological parameter $q \in \{TS_0, k_g, k_s\}$, individual parameters $\psi_{i,q}$ is a function of fixed-effect μ_q and a patient random effect normally distributed $\eta_{i,q} \sim N(0, \omega_{1,q}^2)$:

$$\log(\psi_{i,q}) = \log(\mu_q) + g_q(\eta_{i,q})$$

where g_q is the identity function for each parameter, except for TS_0 where g_q is a Box-Cox function characterized by λ parameter. We assumed an association between the values of the parameters characterizing SLD model and the instantaneous risk of death:

$$h_i(t|\phi, \boldsymbol{\psi_i}) = h_0(t \cdot \alpha|\boldsymbol{\phi}) \times \alpha$$

With $h_0(t \cdot \alpha|\boldsymbol{\phi})$ a lognormal baseline hazard function characterized by the parameters μ and σ, α = exp $(\beta_{k_g} \times k_{g,i} + \beta_{k_d} \times k_{d,i} + \beta_{TS_0} \times TS_{0,i})$.

D.5.2. Effects of drug resistance on longitudinal model performance

The model was estimated on clinical data, but the analysis of the individual fits and the residual plot showed a lack of descriptive ability in the model of advanced states of tumor dynamics. Indeed, as can be seen from Figure D1, there is a trend starting from day 500, when the model underestimates the tumor size.

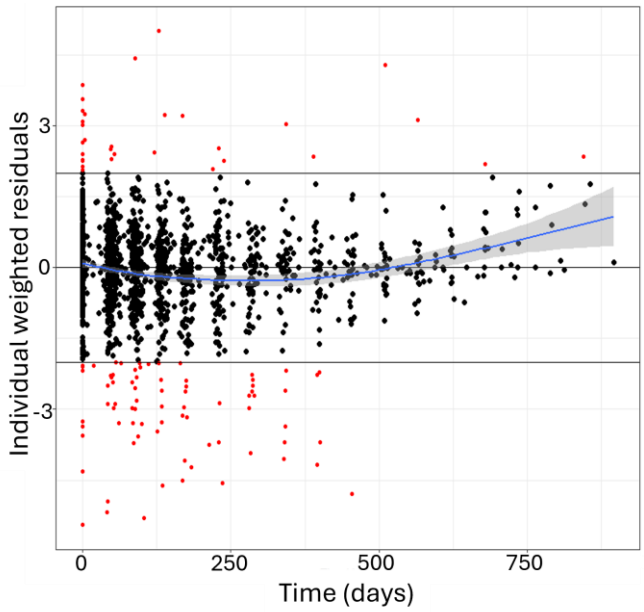

Figure D1 Residual analysis for TS structural model not accounting for drug resistance

After this consideration, the model was updated by introducing a resistance term. At this stage, the fitting diagnostics improved, and model described in Eq. 12 was chosen as the reference model (Figure D2).

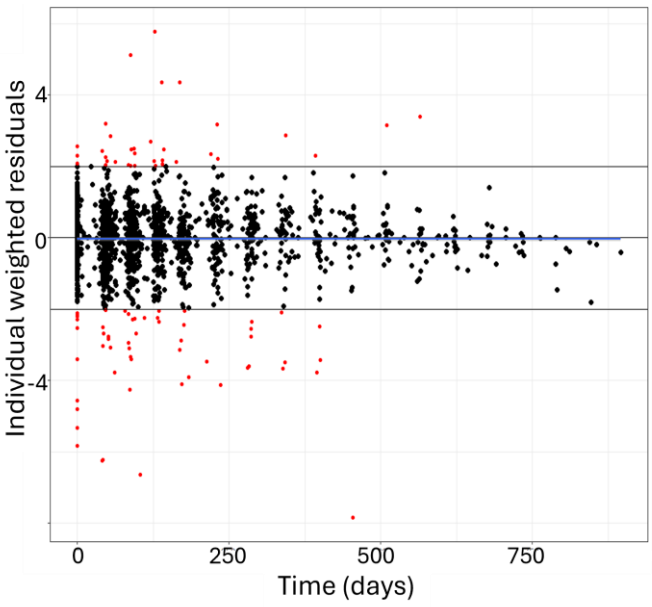

Figure D2 Residual analysis for TS structural model not accounting for drug resistance

The estimated parameters are reported in the following Table.

Table D1 Estimated parameters for the reference SLD model

Parameter	Median	CV (%)
μ	5.7e+0	1.2e+1
σ	9.9e-1	5.2e+0
β_{k_g}	-3.1e-1	2.2e+1
β_{k_d}	1.6e-1	3.0e+1
β_{TS_0}	-5.5e-3	1.4e+1
k_g	1.7e-3	6.2e+0
k_d	1.5e-4	2.4e+1
TS_0	9.6e+1	4.6e+0
R	1.4e-3	4.2e+1
ω_{k_g}	9.0e-1	7.6e+1
ω_{k_d}	1.6e+0	8.8e+0
ω_{TS_0}	7.9e-1	3.8e+1
ω_R	1.7e+0	1.9e+1
λ	-3.8e-1	1.3e+1
σ_1	5.4e-2	5.5e+0
σ_2	2.8e+0	6.7e+0

D.6. Alternative association functions

Alternative finite-time and continuous-time association functions were considered. Specifically, two alternative functions for each group.
The two alternatives finite-time association functions were:

$$\text{A) } \beta \times f(\boldsymbol{\psi_i}) = \sum_{j=1}^{4}\left(\beta_{C_t,j} \times \max_k\left(C_{t,i,j,k}\right)\right) + \sum_{j=1}^{4}\left(\beta_{TS_0,j} \times \sum_{k=1}^{K_{i,j}} TS_{0,i,j,k}\right)$$

$$\text{B) } \beta \times f(\boldsymbol{\psi_i}) = \sum_{j=1}^{4}\left(\beta_{C_t,j} \times \max_k\left(C_{t,i,j,k}\right)^{\Gamma}\right) + \sum_{j=1}^{4}\left(\beta_{TS_0,j} \times \sum_{k=1}^{K_{i,j}} TS_{0,i,j,k}\right)$$

The models differ from the one presented in the main text, for the transformation applied to the maximum $C_{t,i,j,k}$. Specifically, the simpler association structure A has no transformation applied, while association structure B, has an organ-specific transformation $\boldsymbol{\Gamma} = \{\gamma_j\}_{\boldsymbol{j=1}}^{\boldsymbol{4}}$.
The two alternatives continuous-time link function consider were:

$$\mathbf{C)}\ \boldsymbol{\beta} \times \boldsymbol{f}(\boldsymbol{\psi_i}, \boldsymbol{t}) = \sum_{\boldsymbol{j=1}}^{\boldsymbol{4}}\left(\boldsymbol{\beta_{TS,j}} \times \sum_{\boldsymbol{k=1}}^{\boldsymbol{K_{i,j}}} \boldsymbol{TS_{i,j,k}(t)}\right)$$

$$\mathbf{D)}\ \boldsymbol{\beta} \times \boldsymbol{f}(\boldsymbol{\psi_i}, \boldsymbol{t}) = \sum_{\boldsymbol{j=1}}^{\boldsymbol{4}}\left(\boldsymbol{\beta_{TS,j}} \times \sum_{\boldsymbol{k=1}}^{\boldsymbol{K_{i,j}}} log(\boldsymbol{TS_{i,j,k}(t)})\right)$$

These association functions differ from the transformation applied to the tumor size values. Namely, model C do not apply the logarithm

transformation of the tumor size, model D, applied the logarithm transformation before the sum of tumor sizes is applied.

Table D2 summarize the WAIC and LOOIC comparison between these alternative models.

Table D2 Comparison between alternative association structures

Criteria	Model A	Model B	Model C (*)	Model D
WAIC	31479.8	31463.2	-	33249.0
LOOIC	32114.6	31097.1	-	34865.8

Notes: (*) Model C has convergence issues, therefore, no reliable metrics can be provided.

Of note, several tries have been performed but model C never converged.

References

1. Bray, F., Laversanne, M., Weiderpass, E., Soerjomataram, I.: The ever-increasing importance of cancer as a leading cause of premature death worldwide. Cancer. 127, 3029–3030 (2021). https://doi.org/10.1002/cncr.33587.
2. Sung, H., Ferlay, J., Siegel, R.L., Laversanne, M., Soerjomataram, I., Jemal, A., Bray, F.: Global Cancer Statistics 2020: GLOBOCAN Estimates of Incidence and Mortality Worldwide for 36 Cancers in 185 Countries. CA. Cancer J. Clin. 71, 209–249 (2021). https://doi.org/10.3322/caac.21660.
3. Siegel, R.L., Miller, K.D., Wagle, N.S., Jemal, A.: Cancer statistics, 2023. CA. Cancer J. Clin. 73, 17–48 (2023). https://doi.org/10.3322/caac.21763.
4. Mohs, R.C., Greig, N.H.: Drug discovery and development: Role of basic biological research. Alzheimers Dement. N. Y. N. 3, 651–657 (2017). https://doi.org/10.1016/j.trci.2017.10.005.
5. https://www.fda.gov/patients/learn-about-drug-and-device-approvals/drug-development-process.
6. Kummar, S., Gutierrez, M., Doroshow, J.H., Murgo, A.J.: Drug development in oncology: classical cytotoxics and molecularly targeted agents. Br. J. Clin. Pharmacol. 62, 15–26 (2006). https://doi.org/10.1111/j.1365-2125.2006.02713.x.
7. Zhou, Y., Tao, L., Qiu, J., Xu, J., Yang, X., Zhang, Y., Tian, X., Guan, X., Cen, X., Zhao, Y.: Tumor biomarkers for diagnosis, prognosis and targeted therapy. Signal Transduct. Target. Ther. 9, 132 (2024). https://doi.org/10.1038/s41392-024-01823-2.
8. Huang, W., Percie du Sert, N., Vollert, J., Rice, A.S.C.: General Principles of Preclinical Study Design. Handb. Exp. Pharmacol. 257, 55–69 (2020). https://doi.org/10.1007/164_2019_277.
9. Brodniewicz, T., Grynkiewicz, G.: PRECLINICAL DRUG DEVELOPMENT.
10. https://www.iss.it/web/iss-en/phase-i-clinical-trial.
11. Iasonos, A., O'Quigley, J.: Randomised Phase 1 clinical trials in oncology. Br. J. Cancer. 125, 920–926 (2021). https://doi.org/10.1038/s41416-021-01412-y.
12. https://www.cancerresearchuk.org/about-cancer/find-a-clinical-trial/what-clinical-trials-are/phases-of-clinical-trials.
13. NCI Dictionary of Cancer Terms: phase III clinical trial.

14. https://www.allucent.com/resources/blog/what-are-regulatory-differences-between-nda-and-bla.
15. Henry, B.M., Lippi, G., Nasser, A., Ostrowski, P.: Characteristics of Phase IV Clinical Trials in Oncology: An Analysis Using the ClinicalTrials.gov Registry Data. Curr. Oncol. 30, 5932–5945 (2023). https://doi.org/10.3390/curroncol30060443.
16. Prasad, V., Mailankody, S.: Research and Development Spending to Bring a Single Cancer Drug to Market and Revenues After Approval. JAMA Intern. Med. 177, 1569–1575 (2017). https://doi.org/10.1001/jamainternmed.2017.3601.
17. Wouters, O.J., McKee, M., Luyten, J.: Estimated Research and Development Investment Needed to Bring a New Medicine to Market, 2009-2018. JAMA. 323, 844–853 (2020). https://doi.org/10.1001/jama.2020.1166.
18. de Las Heras, B., Bouyoucef-Cherchalli, D., Reeve, L., Reichl, A., Mandarino, D., Flach, S., Vidal, L., van Brummelen, E.M.J., Steeghs, N.: Healthy volunteers in first-in-human oncology drug development for small molecules. Br. J. Clin. Pharmacol. 88, 1773–1784 (2022). https://doi.org/10.1111/bcp.15092.
19. Basak, D., Arrighi, S., Darwiche, Y., Deb, S.: Comparison of Anticancer Drug Toxicities: Paradigm Shift in Adverse Effect Profile. Life Basel Switz. 12, 48 (2021). https://doi.org/10.3390/life12010048.
20. Kola, I., Landis, J.: Can the pharmaceutical industry reduce attrition rates? Nat. Rev. Drug Discov. 3, 711–715 (2004). https://doi.org/10.1038/nrd1470.
21. Gutierrez, M.E., Kummar, S., Giaccone, G.: Next generation oncology drug development: opportunities and challenges. Nat. Rev. Clin. Oncol. 6, 259–265 (2009). https://doi.org/10.1038/nrclinonc.2009.38.
22. Dhingra, K.: Oncology 2020: a drug development and approval paradigm. Ann. Oncol. Off. J. Eur. Soc. Med. Oncol. 26, 2347–2350 (2015). https://doi.org/10.1093/annonc/mdv353.
23. Jaki, T., Burdon, A., Chen, X., Mozgunov, P., Zheng, H., Baird, R.: Early phase clinical trials in oncology: Realising the potential of seamless designs. Eur. J. Cancer Oxf. Engl. 1990. 189, 112916 (2023). https://doi.org/10.1016/j.ejca.2023.05.005.
24. Hutchinson, L., Kirk, R.: High drug attrition rates--where are we going wrong? Nat. Rev. Clin. Oncol. 8, 189–190 (2011). https://doi.org/10.1038/nrclinonc.2011.34.
25. Yates, J.W.T., Byrne, H., Chapman, S.C., Chen, T., Cucurull-Sanchez, L., Delgado-SanMartin, J., Di Veroli, G., Dovedi, S.J., Dunlop, C., Jena, R., Jodrell, D., Martin, E., Mercier, F., Ramos-Montoya, A., Struemper, H., Vicini, P.: Opportunities for Quantitative Translational Modeling in Oncology. Clin. Pharmacol. Ther. 108, 447–457 (2020). https://doi.org/10.1002/cpt.1963.
26. Sajjad, H., Imtiaz, S., Noor, T., Siddiqui, Y.H., Sajjad, A., Zia, M.: Cancer models in preclinical research: A chronicle review of advancement in effective cancer research. Anim. Models Exp. Med. 4, 87–103 (2021). https://doi.org/10.1002/ame2.12165.

27. Dhandapani, M., Goldman, A.: Preclinical Cancer Models and Biomarkers for Drug Development: New Technologies and Emerging Tools. J. Mol. Biomark. Diagn. 8, 356 (2017). https://doi.org/10.4172/2155-9929.1000356.
28. Goodspeed, A., Heiser, L.M., Gray, J.W., Costello, J.C.: Tumor-Derived Cell Lines as Molecular Models of Cancer Pharmacogenomics. Mol. Cancer Res. MCR. 14, 3–13 (2016). https://doi.org/10.1158/1541-7786.MCR-15-0189.
29. Domcke, S., Sinha, R., Levine, D.A., Sander, C., Schultz, N.: Evaluating cell lines as tumour models by comparison of genomic profiles. Nat. Commun. 4, 2126 (2013). https://doi.org/10.1038/ncomms3126.
30. Tosca, E.M., Ronchi, D., Facciolo, D., Magni, P.: Replacement, Reduction, and Refinement of Animal Experiments in Anticancer Drug Development: The Contribution of 3D In Vitro Cancer Models in the Drug Efficacy Assessment. Biomedicines. 11, 1058 (2023). https://doi.org/10.3390/biomedicines11041058.
31. Cacciamali, A., Villa, R., Dotti, S.: 3D Cell Cultures: Evolution of an Ancient Tool for New Applications. Front. Physiol. 13, 836480 (2022). https://doi.org/10.3389/fphys.2022.836480.
32. Astell, K.R., Sieger, D.: Zebrafish In Vivo Models of Cancer and Metastasis. Cold Spring Harb. Perspect. Med. 10, a037077 (2020). https://doi.org/10.1101/cshperspect.a037077.
33. Hason, M., Bartůněk, P.: Zebrafish Models of Cancer-New Insights on Modeling Human Cancer in a Non-Mammalian Vertebrate. Genes. 10, 935 (2019). https://doi.org/10.3390/genes10110935.
34. White, R., Rose, K., Zon, L.: Zebrafish cancer: the state of the art and the path forward. Nat. Rev. Cancer. 13, 624–636 (2013). https://doi.org/10.1038/nrc3589.
35. Jacqueline Plowman PhD, Donald J. Dykes BS, Melinda Hollingshead PhD, Linda Simpson-Herren BS & Michael C. Alley PhD: Human Tumor Xenograft Models in NCI Drug Development (Part of the book: Cancer Drug Discovery and Development).
36. Jung, J.: Human tumor xenograft models for preclinical assessment of anticancer drug development. Toxicol. Res. 30, 1–5 (2014). https://doi.org/10.5487/TR.2014.30.1.001.
37. Abdolahi, S., Ghazvinian, Z., Muhammadnejad, S., Saleh, M., Asadzadeh Aghdaei, H., Baghaei, K.: Patient-derived xenograft (PDX) models, applications and challenges in cancer research. J. Transl. Med. 20, 206 (2022). https://doi.org/10.1186/s12967-022-03405-8.
38. Liu, Y., Wu, W., Cai, C., Zhang, H., Shen, H., Han, Y.: Patient-derived xenograft models in cancer therapy: technologies and applications. Signal Transduct. Target. Ther. 8, 160 (2023). https://doi.org/10.1038/s41392-023-01419-2.
39. He, J., Zhang, C., Ozkan, A., Feng, T., Duan, P., Wang, S., Yang, X., Xie, J., Liu, X.: Patient-derived tumor models and their distinctive applications in personalized drug therapy. Mechanobiol. Med. 1, 100014 (2023). https://doi.org/10.1016/j.mbm.2023.100014.

40. Jin, J., Yoshimura, K., Sewastjanow-Silva, M., Song, S., Ajani, J.A.: Challenges and Prospects of Patient-Derived Xenografts for Cancer Research. Cancers. 15, 4352 (2023). https://doi.org/10.3390/cancers15174352.
41. Kersten, K., de Visser, K.E., van Miltenburg, M.H., Jonkers, J.: Genetically engineered mouse models in oncology research and cancer medicine. EMBO Mol. Med. 9, 137–153 (2017). https://doi.org/10.15252/emmm.201606857.
42. Sharpless, N.E., Depinho, R.A.: The mighty mouse: genetically engineered mouse models in cancer drug development. Nat. Rev. Drug Discov. 5, 741–754 (2006). https://doi.org/10.1038/nrd2110.
43. Delgado, A., Guddati, A.K.: Clinical endpoints in oncology - a primer. Am. J. Cancer Res. 11, 1121–1131 (2021).
44. Clinical Trial Endpoints for the Approval of Cancer Drugs and Biologics. (2018).
45. Purna Singh, A., Shahapur, P.R., Vadakedath, S., Bharadwaj, V.G., Kumar, D.P., Pinnelli, V.B., Godishala, V., Kandi, V.: Research Question, Objectives, and Endpoints in Clinical and Oncological Research: A Comprehensive Review. Cureus. 14, e29575 (2022). https://doi.org/10.7759/cureus.29575.
46. FDA, Clinical Trial Endpoints for the Approval of Cancer Drug and Biologics, https://www.fda.gov/media/71195/download.
47. Fallowfield, L.J., Fleissig, A.: The value of progression-free survival to patients with advanced-stage cancer. Nat. Rev. Clin. Oncol. 9, 41–47 (2011). https://doi.org/10.1038/nrclinonc.2011.156.
48. Belin, L., Tan, A., De Rycke, Y., Dechartres, A.: Progression-free survival as a surrogate for overall survival in oncology trials: a methodological systematic review. Br. J. Cancer. 122, 1707–1714 (2020). https://doi.org/10.1038/s41416-020-0805-y.
49. Booth, C.M., Eisenhauer, E.A., Gyawali, B., Tannock, I.F.: Progression-Free Survival Should Not Be Used as a Primary End Point for Registration of Anticancer Drugs. J. Clin. Oncol. Off. J. Am. Soc. Clin. Oncol. 41, 4968–4972 (2023). https://doi.org/10.1200/JCO.23.01423.
50. Eisenhauer, E.A., Therasse, P., Bogaerts, J., Schwartz, L.H., Sargent, D., Ford, R., Dancey, J., Arbuck, S., Gwyther, S., Mooney, M., Rubinstein, L., Shankar, L., Dodd, L., Kaplan, R., Lacombe, D., Verweij, J.: New response evaluation criteria in solid tumours: revised RECIST guideline (version 1.1). Eur. J. Cancer Oxf. Engl. 1990. 45, 228–247 (2009). https://doi.org/10.1016/j.ejca.2008.10.026.
51. https://www.allucent.com/resources/blog/what-model-informed-drug-development.
52. Zhu, H., Huang, S.M., Madabushi, R., Strauss, D.G., Wang, Y., Zineh, I.: Model-Informed Drug Development: A Regulatory Perspective on Progress. Clin. Pharmacol. Ther. 106, 91–93 (2019). https://doi.org/10.1002/cpt.1475.
53. Mayawala, K., de Alwis, D.P., Sachs, J.R.: Model Informed Drug Development: Novel Oncology Agents are Lost in Translation. Clin.

Cancer Res. Off. J. Am. Assoc. Cancer Res. 25, 6564–6566 (2019). https://doi.org/10.1158/1078-0432.CCR-19-2482.
54. Certara: The model-informed drug development imperative in oncology R&D.
55. Tosca, E.M., Terranova, N., Stuyckens, K., Dosne, A.G., Perera, T., Vialard, J., King, P., Verhulst, T., Perez-Ruixo, J.J., Magni, P., Poggesi, I.: A translational model-based approach to inform the choice of the dose in phase 1 oncology trials: the case study of erdafitinib. Cancer Chemother. Pharmacol. 89, 117–128 (2022). https://doi.org/10.1007/s00280-021-04370-7.
56. Yates, J.W.T., Fairman, D.A.: How translational modeling in oncology needs to get the mechanism just right. Clin. Transl. Sci. 15, 588–600 (2022). https://doi.org/10.1111/cts.13183.
57. Gross, A.S., Harry, A.C., Clifton, C.S., Della Pasqua, O.: Clinical trial diversity: An opportunity for improved insight into the determinants of variability in drug response. Br. J. Clin. Pharmacol. 88, 2700–2717 (2022). https://doi.org/10.1111/bcp.15242.
58. Bayat Mokhtari, R., Homayouni, T.S., Baluch, N., Morgatskaya, E., Kumar, S., Das, B., Yeger, H.: Combination therapy in combating cancer. Oncotarget. 8, 38022–38043 (2017). https://doi.org/10.18632/oncotarget.16723.
59. Baaz, M., Cardilin, T., Lignet, F., Zimmermann, A., El Bawab, S., Gabrielsson, J., Jirstrand, M.: Model-based assessment of combination therapies - ranking of radiosensitizing agents in oncology. BMC Cancer. 23, 409 (2023). https://doi.org/10.1186/s12885-023-10899-y.
60. Bruno, R., Marchand, M., Yoshida, K., Chan, P., Li, H., Zou, W., Mercier, F., Chanu, P., Wu, B., Lee, A., Li, C., Jin, J.Y., Maitland, M.L., Reck, M., Socinski, M.A.: Tumor Dynamic Model-Based Decision Support for Phase Ib/II Combination Studies: A Retrospective Assessment Based on Resampling of the Phase III Study IMpower150. Clin. Cancer Res. Off. J. Am. Assoc. Cancer Res. 29, 1047–1055 (2023). https://doi.org/10.1158/1078-0432.CCR-22-2323.
61. Skrundevskiy, A.N., Omar, O.S., Kim, J., Soliman, A.S., Korolchuk, T.A., Wilson, F.A.: Return on Investment Analysis of Breast Cancer Screening and Downstaging in Egypt: Implications for Developing Countries. Value Health Reg. Issues. 16, 22–27 (2018). https://doi.org/10.1016/j.vhri.2018.01.006.
62. Yin, A., Moes, D.J.A.R., van Hasselt, J.G.C., Swen, J.J., Guchelaar, H.-J.: A Review of Mathematical Models for Tumor Dynamics and Treatment Resistance Evolution of Solid Tumors. CPT Pharmacomet. Syst. Pharmacol. 8, 720–737 (2019). https://doi.org/10.1002/psp4.12450.
63. Stein, A., Wang, W., Carter, A.A., Chiparus, O., Hollaender, N., Kim, H., Motzer, R.J., Sarr, C.: Dynamic tumor modeling of the dose-response relationship for everolimus in metastatic renal cell carcinoma using data from the phase 3 RECORD-1 trial. BMC Cancer. 12, 311 (2012). https://doi.org/10.1186/1471-2407-12-311.
64. Claret, L., Girard, P., Hoff, P.M., Van Cutsem, E., Zuideveld, K.P., Jorga, K., Fagerberg, J., Bruno, R.: Model-based prediction of phase III

overall survival in colorectal cancer on the basis of phase II tumor dynamics. J. Clin. Oncol. Off. J. Am. Soc. Clin. Oncol. 27, 4103–4108 (2009). https://doi.org/10.1200/JCO.2008.21.0807.
65. Ollier, E., Mazzocco, P., Ricard, D., Kaloshi, G., Idbaih, A., Alentorn, A., Psimaras, D., Honnorat, J., Delattre, J.-Y., Grenier, E., Ducray, F., Samson, A.: Analysis of temozolomide resistance in low-grade gliomas using a mechanistic mathematical model. Fundam. Clin. Pharmacol. 31, 347–358 (2017). https://doi.org/10.1111/fcp.12259.
66. Belfatto, A., Riboldi, M., Ciardo, D., Cecconi, A., Lazzari, R., Jereczek-Fossa, B.A., Orecchia, R., Baroni, G., Cerveri, P.: Adaptive Mathematical Model of Tumor Response to Radiotherapy Based on CBCT Data. IEEE J. Biomed. Health Inform. 20, 802–809 (2016). https://doi.org/10.1109/JBHI.2015.2453437.
67. Simeoni, M., Magni, P., Cammia, C., De Nicolao, G., Croci, V., Pesenti, E., Germani, M., Poggesi, I., Rocchetti, M.: Predictive pharmacokinetic-pharmacodynamic modeling of tumor growth kinetics in xenograft models after administration of anticancer agents. Cancer Res. 64, 1094–1101 (2004). https://doi.org/10.1158/0008-5472.can-03-2524.
68. Panetta, J.C., Schaiquevich, P., Santana, V.M., Stewart, C.F.: Using pharmacokinetic and pharmacodynamic modeling and simulation to evaluate importance of schedule in topotecan therapy for pediatric neuroblastoma. Clin. Cancer Res. Off. J. Am. Assoc. Cancer Res. 14, 318–325 (2008). https://doi.org/10.1158/1078-0432.CCR-07-1243.
69. Majid, O., Gupta, A., Reyderman, L., Olivo, M., Hussein, Z.: Population pharmacometric analyses of eribulin in patients with locally advanced or metastatic breast cancer previously treated with anthracyclines and taxanes. J. Clin. Pharmacol. 54, 1134–1143 (2014). https://doi.org/10.1002/jcph.315.
70. Ribba, B., Kaloshi, G., Peyre, M., Ricard, D., Calvez, V., Tod, M., Cajavec-Bernard, B., Idbaih, A., Psimaras, D., Dainese, L., Pallud, J., Cartalat-Carel, S., Delattre, J.-Y., Honnorat, J., Grenier, E., Ducray, F.: A tumor growth inhibition model for low-grade glioma treated with chemotherapy or radiotherapy. Clin. Cancer Res. Off. J. Am. Assoc. Cancer Res. 18, 5071–5080 (2012). https://doi.org/10.1158/1078-0432.CCR-12-0084.
71. De Buck, S.S., Jakab, A., Boehm, M., Bootle, D., Juric, D., Quadt, C., Goggin, T.K.: Population pharmacokinetics and pharmacodynamics of BYL719, a phosphoinositide 3-kinase antagonist, in adult patients with advanced solid malignancies. Br. J. Clin. Pharmacol. 78, 543–555 (2014). https://doi.org/10.1111/bcp.12378.
72. Bruno, R., Chanu, P., Kågedal, M., Mercier, F., Yoshida, K., Guedj, J., Li, C., Beyer, U., Jin, J.Y.: Support to early clinical decisions in drug development and personalised medicine with checkpoint inhibitors using dynamic biomarker-overall survival models. Br. J. Cancer. (2023). https://doi.org/10.1038/s41416-023-02190-5.
73. Keramaris, N.C., Kanakaris, N.K., Tzioupis, C., Kontakis, G., Giannoudis, P.V.: Translational research: from benchside to bedside.

Injury. 39, 643–650 (2008). https://doi.org/10.1016/j.injury.2008.01.051.
74. Wong, H., Choo, E.F., Alicke, B., Ding, X., La, H., McNamara, E., Theil, F.-P., Tibbitts, J., Friedman, L.S., Hop, C.E.C.A., Gould, S.E.: Antitumor activity of targeted and cytotoxic agents in murine subcutaneous tumor models correlates with clinical response. Clin. Cancer Res. Off. J. Am. Assoc. Cancer Res. 18, 3846–3855 (2012). https://doi.org/10.1158/1078-0432.CCR-12-0738.
75. Rocchetti, M., Simeoni, M., Pesenti, E., De Nicolao, G., Poggesi, I.: Predicting the active doses in humans from animal studies: a novel approach in oncology. Eur. J. Cancer Oxf. Engl. 1990. 43, 1862–1868 (2007). https://doi.org/10.1016/j.ejca.2007.05.011.
76. Inaba, M., Kobayashi, T., Tashiro, T., Sakurai, Y.: Pharmacokinetic approach to rational therapeutic doses for human tumor-bearing nude mice. Jpn. J. Cancer Res. Gann. 79, 509–516 (1988). https://doi.org/10.1111/j.1349-7006.1988.tb01620.x.
77. Inaba, M., Tashiro, T., Kobayashi, T., Sakurai, Y., Maruo, K., Ohnishi, Y., Ueyama, Y., Nomura, T.: Responsiveness of human gastric tumors implanted in nude mice to clinically equivalent doses of various antitumor agents. Jpn. J. Cancer Res. Gann. 79, 517–522 (1988). https://doi.org/10.1111/j.1349-7006.1988.tb01621.x.
78. Johnson, J.I., Decker, S., Zaharevitz, D., Rubinstein, L.V., Venditti, J.M., Schepartz, S., Kalyandrug, S., Christian, M., Arbuck, S., Hollingshead, M., Sausville, E.A.: Relationships between drug activity in NCI preclinical in vitro and in vivo models and early clinical trials. Br. J. Cancer. 84, 1424–1431 (2001). https://doi.org/10.1054/bjoc.2001.1796.
79. Spilker, M.E., Chen, X., Visswanathan, R., Vage, C., Yamazaki, S., Li, G., Lucas, J., Bradshaw-Pierce, E.L., Vicini, P.: Found in Translation: Maximizing the Clinical Relevance of Nonclinical Oncology Studies. Clin. Cancer Res. Off. J. Am. Assoc. Cancer Res. 23, 1080–1090 (2017). https://doi.org/10.1158/1078-0432.CCR-16-1164.
80. Garcia-Cremades, M., Pitou, C., Iversen, P.W., Troconiz, I.F.: Translational Framework Predicting Tumour Response in Gemcitabine-Treated Patients with Advanced Pancreatic and Ovarian Cancer from Xenograft Studies. AAPS J. 21, 23 (2019). https://doi.org/10.1208/s12248-018-0291-9.
81. Baaz, M., Cardilin, T., Lignet, F., Jirstrand, M.: Optimized scaling of translational factors in oncology: from xenografts to RECIST. Cancer Chemother. Pharmacol. 90, 239–250 (2022). https://doi.org/10.1007/s00280-022-04458-8.
82. Cardilin, T., Almquist, J., Jirstrand, M., Gabrielsson, J.: Evaluation and translation of combination therapies in oncology - A quantitative approach. Eur. J. Pharmacol. 834, 327–336 (2018). https://doi.org/10.1016/j.ejphar.2018.07.041.
83. Yates, J.W.T., Dudley, P., Cheng, J., D'Cruz, C., Davies, B.R.: Validation of a predictive modeling approach to demonstrate the relative efficacy of three different schedules of the AKT inhibitor AZD5363. Cancer

Chemother. Pharmacol. 76, 343–356 (2015). https://doi.org/10.1007/s00280-015-2795-7.
84. Shrimali, R.K., Ahmad, S., Verma, V., Zeng, P., Ananth, S., Gaur, P., Gittelman, R.M., Yusko, E., Sanders, C., Robins, H., Hammond, S.A., Janik, J.E., Mkrtichyan, M., Gupta, S., Khleif, S.N.: Concurrent PD-1 Blockade Negates the Effects of OX40 Agonist Antibody in Combination Immunotherapy through Inducing T-cell Apoptosis. Cancer Immunol. Res. 5, 755–766 (2017). https://doi.org/10.1158/2326-6066.CIR-17-0292.
85. Netterberg, I., Li, C.-C., Molinero, L., Budha, N., Sukumaran, S., Stroh, M., Jonsson, E.N., Friberg, L.E.: A PK/PD Analysis of Circulating Biomarkers and Their Relationship to Tumor Response in Atezolizumab-Treated non-small Cell Lung Cancer Patients. Clin. Pharmacol. Ther. 105, 486–495 (2019). https://doi.org/10.1002/cpt.1198.
86. Ouerdani, A., Struemper, H., Suttle, A.B., Ouellet, D., Ribba, B.: Preclinical Modeling of Tumor Growth and Angiogenesis Inhibition to Describe Pazopanib Clinical Effects in Renal Cell Carcinoma. CPT Pharmacomet. Syst. Pharmacol. 4, 660–668 (2015). https://doi.org/10.1002/psp4.12001.
87. Kilkenny, C., Parsons, N., Kadyszewski, E., Festing, M.F.W., Cuthill, I.C., Fry, D., Hutton, J., Altman, D.G.: Survey of the quality of experimental design, statistical analysis and reporting of research using animals. PloS One. 4, e7824 (2009). https://doi.org/10.1371/journal.pone.0007824.
88. Dahan, M., Hequet, D., Bonneau, C., Paoletti, X., Rouzier, R.: Has tumor doubling time in breast cancer changed over the past 80 years? A systematic review. Cancer Med. 10, 5203–5217 (2021). https://doi.org/10.1002/cam4.3939.
89. Mehrara, E., Forssell-Aronsson, E., Bernhardt, P.: Objective assessment of tumour response to therapy based on tumour growth kinetics. Br. J. Cancer. 105, 682–686 (2011). https://doi.org/10.1038/bjc.2011.276.
90. Ollila, D.W., Stern, S.L., Morton, D.L.: Tumor doubling time: a selection factor for pulmonary resection of metastatic melanoma. J. Surg. Oncol. 69, 206–211 (1998). https://doi.org/10.1002/(sici)1096-9098(199812)69:4<206::aid-jso3>3.0.co;2-n.
91. Okazaki, N., Yoshino, M., Yoshida, T., Suzuki, M., Moriyama, N., Takayasu, K., Makuuchi, M., Yamazaki, S., Hasegawa, H., Noguchi, M.: Evaluation of the prognosis for small hepatocellular carcinoma based on tumor volume doubling time. A preliminary report. Cancer. 63, 2207–2210 (1989). https://doi.org/10.1002/1097-0142(19890601)63:11<2207::aid-cncr2820631124>3.0.co;2-c.
92. Furukawa, H., Iwata, R., Moriyama, N.: Growth rate of pancreatic adenocarcinoma: Initial clinical experience. Pancreas. 22, 366–369 (2001). https://doi.org/10.1097/00006676-200105000-00005.

93. White, C.R., Seymour, R.S.: Mammalian basal metabolic rate is proportional to body mass2/3. Proc. Natl. Acad. Sci. U. S. A. 100, 4046–4049 (2003). https://doi.org/10.1073/pnas.0436428100.
94. Kay, K., Dolcy, K., Bies, R., Shah, D.K.: Estimation of Solid Tumor Doubling Times from Progression-Free Survival Plots Using a Novel Statistical Approach. AAPS J. 21, 27 (2019). https://doi.org/10.1208/s12248-019-0302-5.
95. Eisenhauer, E.A., Therasse, P., Bogaerts, J., Schwartz, L.H., Sargent, D., Ford, R., Dancey, J., Arbuck, S., Gwyther, S., Mooney, M., Rubinstein, L., Shankar, L., Dodd, L., Kaplan, R., Lacombe, D., Verweij, J.: New response evaluation criteria in solid tumours: Revised RECIST guideline (version 1.1). Eur. J. Cancer. 45, (2009). https://doi.org/10.1016/j.ejca.2008.10.026.
96. von Fournier, D., Weber, E., Hoeffken, W., Bauer, M., Kubli, F., Barth, V.: Growth rate of 147 mammary carcinomas. Cancer. 45, 2198–2207 (1980). https://doi.org/10.1002/1097-0142(19800415)45:8<2198::aid-cncr2820450832>3.0.co;2-7.
97. Gershon-Cohen, J., Berger, S.M., Klickstein, H.S.: ROENTGENOGRAPHY OF BREAST CANCER MODERATING CONCEPT OF "BIOLOGIC PREDETERMINISM." Cancer. 16, 961–964 (1963). https://doi.org/10.1002/1097-0142(196308)16:8<961::aid-cncr2820160802>3.0.co;2-b.
98. Ryu, E.B., Chang, J.M., Seo, M., Kim, S.A., Lim, J.H., Moon, W.K.: Tumour volume doubling time of molecular breast cancer subtypes assessed by serial breast ultrasound. Eur. Radiol. 24, 2227–2235 (2014). https://doi.org/10.1007/s00330-014-3256-0.
99. Tabbane, F., Bahi, J., Rahal, K., el May, A., Riahi, M., Cammoun, M., Hechiche, M., Jaziri, M., Mourali, N.: Inflammatory symptoms in breast cancer. Correlations with growth rate, clinicopathologic variables, and evolution. Cancer. 64, 2081–2089 (1989). https://doi.org/10.1002/1097-0142(19891115)64:10<2081::aid-cncr2820641019>3.0.co;2-7.
100. Zhang, S., Ding, Y., Zhou, Q., Wang, C., Wu, P., Dong, J.: Correlation Factors Analysis of Breast Cancer Tumor Volume Doubling Time Measured by 3D-Ultrasound. Med. Sci. Monit. Int. Med. J. Exp. Clin. Res. 23, 3147–3153 (2017). https://doi.org/10.12659/msm.901566.
101. De Rose, A.M., Cucchetti, A., Clemente, G., Ardito, F., Giovannini, I., Ercolani, G., Giuliante, F., Pinna, A.D., Nuzzo, G.: Prognostic significance of tumor doubling time in mass-forming type cholangiocarcinoma. J. Gastrointest. Surg. Off. J. Soc. Surg. Aliment. Tract. 17, 739–747 (2013). https://doi.org/10.1007/s11605-012-2129-6.
102. Bolin, S., Nilsson, E., Sjödahl, R.: Carcinoma of the colon and rectum--growth rate. Ann. Surg. 198, 151–158 (1983). https://doi.org/10.1097/00000658-198308000-00007.
103. Burke, J.R., Brown, P., Quyn, A., Lambie, H., Tolan, D., Sagar, P.: Tumour growth rate of carcinoma of the colon and rectum: retrospective cohort study. BJS Open. 4, 1200–1207 (2020). https://doi.org/10.1002/bjs5.50355.

104. Tada, M., Misaki, F., Kawai, K.: Growth rates of colorectal carcinoma and adenoma by roentgenologic follow-up observations. Gastroenterol. Jpn. 19, 550–555 (1984). https://doi.org/10.1007/BF02793869.
105. Haruma, K., Suzuki, T., Tsuda, T., Yoshihara, M., Sumii, K., Kajiyama, G.: Evaluation of tumor growth rate in patients with early gastric carcinoma of the elevated type. Gastrointest. Radiol. 16, 289–292 (1991). https://doi.org/10.1007/BF01887370.
106. Choi, S.J., Kim, H.-S., Ahn, S.-J., Jeong, Y.M., Choi, H.-Y.: Evaluation of the growth pattern of carcinoma of colon and rectum by MDCT. Acta Radiol. Stockh. Swed. 1987. 54, 487–492 (2013). https://doi.org/10.1177/0284185113475923.
107. Jensen, A.R., Nellemann, H.M., Overgaard, J.: Tumor progression in waiting time for radiotherapy in head and neck cancer. Radiother. Oncol. J. Eur. Soc. Ther. Radiol. Oncol. 84, 5–10 (2007). https://doi.org/10.1016/j.radonc.2007.04.001.
108. Waaijer, A., Terhaard, C.H.J., Dehnad, H., Hordijk, G.-J., van Leeuwen, M.S., Raaymakers, C.P.J., Lagendijk, J.J.W.: Waiting times for radiotherapy: consequences of volume increase for the TCP in oropharyngeal carcinoma. Radiother. Oncol. J. Eur. Soc. Ther. Radiol. Oncol. 66, 271–276 (2003). https://doi.org/10.1016/s0167-8140(03)00036-7.
109. Barbara, L., Benzi, G., Gaiani, S., Fusconi, F., Zironi, G., Siringo, S., Rigamonti, A., Barbara, C., Grigioni, W., Mazziotti, A.: Natural history of small untreated hepatocellular carcinoma in cirrhosis: a multivariate analysis of prognostic factors of tumor growth rate and patient survival. Hepatol. Baltim. Md. 16, 132–137 (1992). https://doi.org/10.1002/hep.1840160122.
110. Kubota, K., Ina, H., Okada, Y., Irie, T.: Growth rate of primary single hepatocellular carcinoma: determining optimal screening interval with contrast enhanced computed tomography. Dig. Dis. Sci. 48, 581–586 (2003). https://doi.org/10.1023/a:1022505203786.
111. Park, Y., Choi, D., Lim, H.K., Rhim, H., Kim, Y.-S., Kim, S.H., Lee, W.J.: Growth rate of new hepatocellular carcinoma after percutaneous radiofrequency ablation: evaluation with multiphase CT. AJR Am. J. Roentgenol. 191, 215–220 (2008). https://doi.org/10.2214/AJR.07.3297.
112. Sheu, J.-C., Sung, J.-L., Chen, D.-S., Yang, P.-M., Lai, M.-Y., Lee, C.-S., Hsu, H.-C., Chuang, C.-N., Yang, P.-C., Wang, T.-H., Lin, J.-T., Lee, C.-Z.: Growth rate of asymptomatic hepatocellular carcinoma and its clinical implications. Gastroenterology. 89, 259–266 (1985). https://doi.org/10.1016/0016-5085(85)90324-5.
113. Nakajima, T., Moriguchi, M., Mitsumoto, Y., Katagishi, T., Kimura, H., Shintani, H., Deguchi, T., Okanoue, T., Kagawa, K., Ashihara, T.: Simple tumor profile chart based on cell kinetic parameters and histologic grade is useful for estimating the natural growth rate of hepatocellular carcinoma. Hum. Pathol. 33, 92–99 (2002). https://doi.org/10.1053/hupa.2002.30194.

114. Honda, O., Johkoh, T., Sekiguchi, J., Tomiyama, N., Mihara, N., Sumikawa, H., Inoue, A., Yanagawa, M., Daimon, T., Okumura, M., Nakamura, H.: Doubling time of lung cancer determined using three-dimensional volumetric software: comparison of squamous cell carcinoma and adenocarcinoma. Lung Cancer Amst. Neth. 66, 211–217 (2009). https://doi.org/10.1016/j.lungcan.2009.01.018.
115. Kanashiki, M., Tomizawa, T., Yamaguchi, I., Kurishima, K., Hizawa, N., Ishikawa, H., Kagohashi, K., Satoh, H.: Volume doubling time of lung cancers detected in a chest radiograph mass screening program: Comparison with CT screening. Oncol. Lett. 4, 513–516 (2012). https://doi.org/10.3892/ol.2012.780.
116. Mackintosh, J.A., Marshall, H.M., Yang, I.A., Bowman, R.V., Fong, K.M.: A retrospective study of volume doubling time in surgically resected non-small cell lung cancer. Respirol. Carlton Vic. 19, 755–762 (2014). https://doi.org/10.1111/resp.12311.
117. Carlson, J.A.: Tumor doubling time of cutaneous melanoma and its metastasis. Am. J. Dermatopathol. 25, 291–299 (2003). https://doi.org/10.1097/00000372-200308000-00003.
118. Furukawa, H., Iwata, R., Moriyama, N.: Growth rate of pancreatic adenocarcinoma: initial clinical experience. Pancreas. 22, 366–369 (2001). https://doi.org/10.1097/00006676-200105000-00005.
119. Rezai, P., Yaghmai, V., Tochetto, S.M., Galizia, M.S., Miller, F.H., Mulcahy, M.F., Small, W.: Change in the growth rate of localized pancreatic adenocarcinoma in response to gemcitabine, bevacizumab, and radiation therapy on MDCT. Int. J. Radiat. Oncol. Biol. Phys. 81, 452–459 (2011). https://doi.org/10.1016/j.ijrobp.2010.05.060.
120. Galante, E., Milani, A., Attili, A.: Growth rate of soft tissue sarcomas: a quantitative study of 44 local recurrences. Tumori. 66, 215–222 (1980). https://doi.org/10.1177/030089168006600210.
121. Spratt, J.S., Meyer, J.S., Spratt, J.A.: Rates of growth of human neoplasms: Part II. J. Surg. Oncol. 61, 68–83 (1996). https://doi.org/10.1002/1096-9098(199601)61:1<68::aid-jso2930610102>3.0.co;2-e.
122. Casak, S.J., Pradhan, S., Fashoyin-Aje, L.A., Ren, Y., Shen, Y.-L., Xu, Y., Chow, E.C.Y., Xiong, Y., Zirklelbach, J.F., Liu, J., Charlab, R., Pierce, W.F., Fesenko, N., Beaver, J.A., Pazdur, R., Kluetz, P.G., Lemery, S.J.: FDA Approval Summary: Ivosidenib for the Treatment of Patients with Advanced Unresectable or Metastatic, Chemotherapy Refractory Cholangiocarcinoma with an IDH1 Mutation. Clin. Cancer Res. Off. J. Am. Assoc. Cancer Res. 28, 2733–2737 (2022). https://doi.org/10.1158/1078-0432.CCR-21-4462.
123. Zhu, A.X., Macarulla, T., Javle, M.M., Kelley, R.K., Lubner, S.J., Adeva, J., Cleary, J.M., Catenacci, D.V.T., Borad, M.J., Bridgewater, J.A., Harris, W.P., Murphy, A.G., Oh, D.-Y., Whisenant, J.R., Lowery, M.A., Goyal, L., Shroff, R.T., El-Khoueiry, A.B., Chamberlain, C.X., Aguado-Fraile, E., Choe, S., Wu, B., Liu, H., Gliser, C., Pandya, S.S., Valle, J.W., Abou-Alfa, G.K.: Final Overall Survival Efficacy Results of Ivosidenib for Patients With Advanced Cholangiocarcinoma With IDH1 Mutation: The Phase 3

Randomized Clinical ClarIDHy Trial. JAMA Oncol. 7, 1669–1677 (2021). https://doi.org/10.1001/jamaoncol.2021.3836.
124. Bendell, J.C., Nemunaitis, J., Vukelja, S.J., Hagenstad, C., Campos, L.T., Hermann, R.C., Sportelli, P., Gardner, L., Richards, D.A.: Randomized placebo-controlled phase II trial of perifosine plus capecitabine as second- or third-line therapy in patients with metastatic colorectal cancer. J. Clin. Oncol. Off. J. Am. Soc. Clin. Oncol. 29, 4394–4400 (2011). https://doi.org/10.1200/JCO.2011.36.1980.
125. Van Cutsem, E., Peeters, M., Siena, S., Humblet, Y., Hendlisz, A., Neyns, B., Canon, J.-L., Van Laethem, J.-L., Maurel, J., Richardson, G., Wolf, M., Amado, R.G.: Open-label phase III trial of panitumumab plus best supportive care compared with best supportive care alone in patients with chemotherapy-refractory metastatic colorectal cancer. J. Clin. Oncol. Off. J. Am. Soc. Clin. Oncol. 25, 1658–1664 (2007). https://doi.org/10.1200/JCO.2006.08.1620.
126. Dasari, A., Lonardi, S., Garcia-Carbonero, R., Elez, E., Yoshino, T., Sobrero, A., Yao, J., García-Alfonso, P., Kocsis, J., Cubillo Gracian, A., Sartore-Bianchi, A., Satoh, T., Randrian, V., Tomasek, J., Chong, G., Paulson, A.S., Masuishi, T., Jones, J., Csőszi, T., Cremolini, C., Ghiringhelli, F., Shergill, A., Hochster, H.S., Krauss, J., Bassam, A., Ducreux, M., Elme, A., Faugeras, L., Kasper, S., Van Cutsem, E., Arnold, D., Nanda, S., Yang, Z., Schelman, W.R., Kania, M., Tabernero, J., Eng, C., FRESCO-2 Study Investigators: Fruquintinib versus placebo in patients with refractory metastatic colorectal cancer (FRESCO-2): an international, multicentre, randomised, double-blind, phase 3 study. Lancet Lond. Engl. 402, 41–53 (2023). https://doi.org/10.1016/S0140-6736(23)00772-9.
127. Hecht, J.R., Benson, A.B., Vyushkov, D., Yang, Y., Bendell, J., Verma, U.: A Phase II, Randomized, Double-Blind, Placebo-Controlled Study of Simtuzumab in Combination with FOLFIRI for the Second-Line Treatment of Metastatic KRAS Mutant Colorectal Adenocarcinoma. The Oncologist. 22, 243-e23 (2017). https://doi.org/10.1634/theoncologist.2016-0479.
128. Bang, Y.-J., Im, S.-A., Lee, K.-W., Cho, J.Y., Song, E.-K., Lee, K.H., Kim, Y.H., Park, J.O., Chun, H.G., Zang, D.Y., Fielding, A., Rowbottom, J., Hodgson, D., O'Connor, M.J., Yin, X., Kim, W.H.: Randomized, Double-Blind Phase II Trial With Prospective Classification by ATM Protein Level to Evaluate the Efficacy and Tolerability of Olaparib Plus Paclitaxel in Patients With Recurrent or Metastatic Gastric Cancer. J. Clin. Oncol. Off. J. Am. Soc. Clin. Oncol. 33, 3858–3865 (2015). https://doi.org/10.1200/JCO.2014.60.0320.
129. Boku, N., Yamamoto, S., Fukuda, H., Shirao, K., Doi, T., Sawaki, A., Koizumi, W., Saito, H., Yamaguchi, K., Takiuchi, H., Nasu, J., Ohtsu, A., Gastrointestinal Oncology Study Group of the Japan Clinical Oncology Group: Fluorouracil versus combination of irinotecan plus cisplatin versus S-1 in metastatic gastric cancer: a randomised phase 3 study. Lancet Oncol. 10, 1063–1069 (2009). https://doi.org/10.1016/S1470-2045(09)70259-1.

130. Ohtsu, A., Shimada, Y., Shirao, K., Boku, N., Hyodo, I., Saito, H., Yamamichi, N., Miyata, Y., Ikeda, N., Yamamoto, S., Fukuda, H., Yoshida, S., Japan Clinical Oncology Group Study (JCOG9205): Randomized phase III trial of fluorouracil alone versus fluorouracil plus cisplatin versus uracil and tegafur plus mitomycin in patients with unresectable, advanced gastric cancer: The Japan Clinical Oncology Group Study (JCOG9205). J. Clin. Oncol. Off. J. Am. Soc. Clin. Oncol. 21, 54–59 (2003). https://doi.org/10.1200/JCO.2003.04.130.
131. Vanhoefer, U., Rougier, P., Wilke, H., Ducreux, M.P., Lacave, A.J., Van Cutsem, E., Planker, M., Santos, J.G., Piedbois, P., Paillot, B., Bodenstein, H., Schmoll, H.J., Bleiberg, H., Nordlinger, B., Couvreur, M.L., Baron, B., Wils, J.A.: Final results of a randomized phase III trial of sequential high-dose methotrexate, fluorouracil, and doxorubicin versus etoposide, leucovorin, and fluorouracil versus infusional fluorouracil and cisplatin in advanced gastric cancer: A trial of the European Organization for Research and Treatment of Cancer Gastrointestinal Tract Cancer Cooperative Group. J. Clin. Oncol. Off. J. Am. Soc. Clin. Oncol. 18, 2648–2657 (2000). https://doi.org/10.1200/JCO.2000.18.14.2648.
132. Burtness, B., Goldwasser, M.A., Flood, W., Mattar, B., Forastiere, A.A., Eastern Cooperative Oncology Group: Phase III randomized trial of cisplatin plus placebo compared with cisplatin plus cetuximab in metastatic/recurrent head and neck cancer: an Eastern Cooperative Oncology Group study. J. Clin. Oncol. Off. J. Am. Soc. Clin. Oncol. 23, 8646–8654 (2005). https://doi.org/10.1200/JCO.2005.02.4646.
133. Cohen, E.E.W., Soulières, D., Le Tourneau, C., Dinis, J., Licitra, L., Ahn, M.-J., Soria, A., Machiels, J.-P., Mach, N., Mehra, R., Burtness, B., Zhang, P., Cheng, J., Swaby, R.F., Harrington, K.J., KEYNOTE-040 investigators: Pembrolizumab versus methotrexate, docetaxel, or cetuximab for recurrent or metastatic head-and-neck squamous cell carcinoma (KEYNOTE-040): a randomised, open-label, phase 3 study. Lancet Lond. Engl. 393, 156–167 (2019). https://doi.org/10.1016/S0140-6736(18)31999-8.
134. Ferris, R.L., Blumenschein, G., Fayette, J., Guigay, J., Colevas, A.D., Licitra, L., Harrington, K., Kasper, S., Vokes, E.E., Even, C., Worden, F., Saba, N.F., Iglesias Docampo, L.C., Haddad, R., Rordorf, T., Kiyota, N., Tahara, M., Monga, M., Lynch, M., Geese, W.J., Kopit, J., Shaw, J.W., Gillison, M.L.: Nivolumab for Recurrent Squamous-Cell Carcinoma of the Head and Neck. N. Engl. J. Med. 375, 1856–1867 (2016). https://doi.org/10.1056/NEJMoa1602252.
135. Cheng, A.-L., Kang, Y.-K., Chen, Z., Tsao, C.-J., Qin, S., Kim, J.S., Luo, R., Feng, J., Ye, S., Yang, T.-S., Xu, J., Sun, Y., Liang, H., Liu, J., Wang, J., Tak, W.Y., Pan, H., Burock, K., Zou, J., Voliotis, D., Guan, Z.: Efficacy and safety of sorafenib in patients in the Asia-Pacific region with advanced hepatocellular carcinoma: a phase III randomised, double-blind, placebo-controlled trial. Lancet Oncol. 10, 25–34 (2009). https://doi.org/10.1016/S1470-2045(08)70285-7.

136. Llovet, J.M., Ricci, S., Mazzaferro, V., Hilgard, P., Gane, E., Blanc, J.-F., de Oliveira, A.C., Santoro, A., Raoul, J.-L., Forner, A., Schwartz, M., Porta, C., Zeuzem, S., Bolondi, L., Greten, T.F., Galle, P.R., Seitz, J.-F., Borbath, I., Häussinger, D., Giannaris, T., Shan, M., Moscovici, M., Voliotis, D., Bruix, J., SHARP Investigators Study Group: Sorafenib in advanced hepatocellular carcinoma. N. Engl. J. Med. 359, 378–390 (2008). https://doi.org/10.1056/NEJMoa0708857.
137. Zhu, A.X., Park, J.O., Ryoo, B.-Y., Yen, C.-J., Poon, R., Pastorelli, D., Blanc, J.-F., Chung, H.C., Baron, A.D., Pfiffer, T.E.F., Okusaka, T., Kubackova, K., Trojan, J., Sastre, J., Chau, I., Chang, S.-C., Abada, P.B., Yang, L., Schwartz, J.D., Kudo, M., REACH Trial Investigators: Ramucirumab versus placebo as second-line treatment in patients with advanced hepatocellular carcinoma following first-line therapy with sorafenib (REACH): a randomised, double-blind, multicentre, phase 3 trial. Lancet Oncol. 16, 859–870 (2015). https://doi.org/10.1016/S1470-2045(15)00050-9.
138. Chapman, P.B., Hauschild, A., Robert, C., Haanen, J.B., Ascierto, P., Larkin, J., Dummer, R., Garbe, C., Testori, A., Maio, M., Hogg, D., Lorigan, P., Lebbe, C., Jouary, T., Schadendorf, D., Ribas, A., O'Day, S.J., Sosman, J.A., Kirkwood, J.M., Eggermont, A.M.M., Dreno, B., Nolop, K., Li, J., Nelson, B., Hou, J., Lee, R.J., Flaherty, K.T., McArthur, G.A., BRIM-3 Study Group: Improved survival with vemurafenib in melanoma with BRAF V600E mutation. N. Engl. J. Med. 364, 2507–2516 (2011). https://doi.org/10.1056/NEJMoa1103782.
139. Hauschild, A., Grob, J.-J., Demidov, L.V., Jouary, T., Gutzmer, R., Millward, M., Rutkowski, P., Blank, C.U., Miller, W.H., Kaempgen, E., Martín-Algarra, S., Karaszewska, B., Mauch, C., Chiarion-Sileni, V., Martin, A.-M., Swann, S., Haney, P., Mirakhur, B., Guckert, M.E., Goodman, V., Chapman, P.B.: Dabrafenib in BRAF-mutated metastatic melanoma: a multicentre, open-label, phase 3 randomised controlled trial. Lancet Lond. Engl. 380, 358–365 (2012). https://doi.org/10.1016/S0140-6736(12)60868-X.
140. Kim, K.B., Kefford, R., Pavlick, A.C., Infante, J.R., Ribas, A., Sosman, J.A., Fecher, L.A., Millward, M., McArthur, G.A., Hwu, P., Gonzalez, R., Ott, P.A., Long, G.V., Gardner, O.S., Ouellet, D., Xu, Y., DeMarini, D.J., Le, N.T., Patel, K., Lewis, K.D.: Phase II study of the MEK1/MEK2 inhibitor Trametinib in patients with metastatic BRAF-mutant cutaneous melanoma previously treated with or without a BRAF inhibitor. J. Clin. Oncol. Off. J. Am. Soc. Clin. Oncol. 31, 482–489 (2013). https://doi.org/10.1200/JCO.2012.43.5966.
141. Conroy, T., Desseigne, F., Ychou, M., Bouché, O., Guimbaud, R., Bécouarn, Y., Adenis, A., Raoul, J.-L., Gourgou-Bourgade, S., de la Fouchardière, C., Bennouna, J., Bachet, J.-B., Khemissa-Akouz, F., Péré-Vergé, D., Delbaldo, C., Assenat, E., Chauffert, B., Michel, P., Montoto-Grillot, C., Ducreux, M., Groupe Tumeurs Digestives of Unicancer, PRODIGE Intergroup: FOLFIRINOX versus gemcitabine for metastatic pancreatic cancer. N. Engl. J. Med. 364, 1817–1825 (2011). https://doi.org/10.1056/NEJMoa1011923.

142. Girardi, D.M., Faria, L.D.B.B., Teixeira, M.C., Costa, F.P., Hoff, P.M.G., Fernandes, G.S.: Second-Line Treatment for Advanced Pancreatic Adenocarcinoma: Is There a Role for Gemcitabine? J. Gastrointest. Cancer. 50, 860–866 (2019). https://doi.org/10.1007/s12029-018-0166-4.
143. Kindler, H.L., Niedzwiecki, D., Hollis, D., Sutherland, S., Schrag, D., Hurwitz, H., Innocenti, F., Mulcahy, M.F., O'Reilly, E., Wozniak, T.F., Picus, J., Bhargava, P., Mayer, R.J., Schilsky, R.L., Goldberg, R.M.: Gemcitabine plus bevacizumab compared with gemcitabine plus placebo in patients with advanced pancreatic cancer: phase III trial of the Cancer and Leukemia Group B (CALGB 80303). J. Clin. Oncol. Off. J. Am. Soc. Clin. Oncol. 28, 3617–3622 (2010). https://doi.org/10.1200/JCO.2010.28.1386.
144. Moore, M.J., Goldstein, D., Hamm, J., Figer, A., Hecht, J.R., Gallinger, S., Au, H.J., Murawa, P., Walde, D., Wolff, R.A., Campos, D., Lim, R., Ding, K., Clark, G., Voskoglou-Nomikos, T., Ptasynski, M., Parulekar, W., National Cancer Institute of Canada Clinical Trials Group: Erlotinib plus gemcitabine compared with gemcitabine alone in patients with advanced pancreatic cancer: a phase III trial of the National Cancer Institute of Canada Clinical Trials Group. J. Clin. Oncol. Off. J. Am. Soc. Clin. Oncol. 25, 1960–1966 (2007). https://doi.org/10.1200/JCO.2006.07.9525.
145. Gounder, M.M., Razak, A.A., Somaiah, N., Chawla, S., Martin-Broto, J., Grignani, G., Schuetze, S.M., Vincenzi, B., Wagner, A.J., Chmielowski, B., Jones, R.L., Riedel, R.F., Stacchiotti, S., Loggers, E.T., Ganjoo, K.N., Le Cesne, A., Italiano, A., Garcia Del Muro, X., Burgess, M., Piperno-Neumann, S., Ryan, C., Mulcahy, M.F., Forscher, C., Penel, N., Okuno, S., Elias, A., Hartner, L., Philip, T., Alcindor, T., Kasper, B., Reichardt, P., Lapeire, L., Blay, J.-Y., Chevreau, C., Valverde Morales, C.M., Schwartz, G.K., Chen, J.L., Deshpande, H., Davis, E.J., Nicholas, G., Gröschel, S., Hatcher, H., Duffaud, F., Herráez, A.C., Beveridge, R.D., Badalamenti, G., Eriksson, M., Meyer, C., von Mehren, M., Van Tine, B.A., Götze, K., Mazzeo, F., Yakobson, A., Zick, A., Lee, A., Gonzalez, A.E., Napolitano, A., Dickson, M.A., Michel, D., Meng, C., Li, L., Liu, J., Ben-Shahar, O., Van Domelen, D.R., Walker, C.J., Chang, H., Landesman, Y., Shah, J.J., Shacham, S., Kauffman, M.G., Attia, S.: Selinexor in Advanced, Metastatic Dedifferentiated Liposarcoma: A Multinational, Randomized, Double-Blind, Placebo-Controlled Trial. J. Clin. Oncol. Off. J. Am. Soc. Clin. Oncol. 40, 2479–2490 (2022). https://doi.org/10.1200/JCO.21.01829.
146. Kawai, A., Araki, N., Hiraga, H., Sugiura, H., Matsumine, A., Ozaki, T., Ueda, T., Ishii, T., Esaki, T., Machida, M., Fukasawa, N.: A randomized, double-blind, placebo-controlled, Phase III study of pazopanib in patients with soft tissue sarcoma: results from the Japanese subgroup. Jpn. J. Clin. Oncol. 46, 248–253 (2016). https://doi.org/10.1093/jjco/hyv184.
147. GEMZAR FDA AccessData, https://www.accessdata.fda.gov/drugsatfda_docs/label/2011/020509s069lbl.pdf.

148. Hong, J.Y., Nam, E.M., Lee, J., Park, J.O., Lee, S.-C., Song, S.-Y., Choi, S.H., Heo, J.S., Park, S.H., Lim, H.Y., Kang, W.K., Park, Y.S.: Randomized double-blinded, placebo-controlled phase II trial of simvastatin and gemcitabine in advanced pancreatic cancer patients. Cancer Chemother. Pharmacol. 73, 125–130 (2014). https://doi.org/10.1007/s00280-013-2328-1.
149. Kindler, H.L., Ioka, T., Richel, D.J., Bennouna, J., Létourneau, R., Okusaka, T., Funakoshi, A., Furuse, J., Park, Y.S., Ohkawa, S., Springett, G.M., Wasan, H.S., Trask, P.C., Bycott, P., Ricart, A.D., Kim, S., Van Cutsem, E.: Axitinib plus gemcitabine versus placebo plus gemcitabine in patients with advanced pancreatic adenocarcinoma: a double-blind randomised phase 3 study. Lancet Oncol. 12, 256–262 (2011). https://doi.org/10.1016/S1470-2045(11)70004-3.
150. Nakai, Y., Isayama, H., Sasaki, T., Sasahira, N., Tsujino, T., Toda, N., Kogure, H., Matsubara, S., Ito, Y., Togawa, O., Arizumi, T., Hirano, K., Tada, M., Omata, M., Koike, K.: A multicentre randomised phase II trial of gemcitabine alone vs gemcitabine and S-1 combination therapy in advanced pancreatic cancer: GEMSAP study. Br. J. Cancer. 106, 1934–1939 (2012). https://doi.org/10.1038/bjc.2012.183.
151. Ozaka, M., Matsumura, Y., Ishii, H., Omuro, Y., Itoi, T., Mouri, H., Hanada, K., Kimura, Y., Maetani, I., Okabe, Y., Tani, M., Ikeda, T., Hijioka, S., Watanabe, R., Ohoka, S., Hirose, Y., Suyama, M., Egawa, N., Sofuni, A., Ikari, T., Nakajima, T.: Randomized phase II study of gemcitabine and S-1 combination versus gemcitabine alone in the treatment of unresectable advanced pancreatic cancer (Japan Clinical Cancer Research Organization PC-01 study). Cancer Chemother. Pharmacol. 69, 1197–1204 (2012). https://doi.org/10.1007/s00280-012-1822-1.
152. Bruix, J., Cheng, A.-L., Meinhardt, G., Nakajima, K., De Sanctis, Y., Llovet, J.: Prognostic factors and predictors of sorafenib benefit in patients with hepatocellular carcinoma: Analysis of two phase III studies. J. Hepatol. 67, 999–1008 (2017). https://doi.org/10.1016/j.jhep.2017.06.026.
153. Sorafenib, https://www.ema.europa.eu/en/documents/product-information/nexavar-epar-product-information_en.pdf.
154. Park, J.-W., Kim, Y.J., Kim, D.Y., Bae, S.-H., Paik, S.W., Lee, Y.-J., Kim, H.Y., Lee, H.C., Han, S.Y., Cheong, J.Y., Kwon, O.S., Yeon, J.E., Kim, B.H., Hwang, J.: Sorafenib with or without concurrent transarterial chemoembolization in patients with advanced hepatocellular carcinoma: The phase III STAH trial. J. Hepatol. 70, 684–691 (2019). https://doi.org/10.1016/j.jhep.2018.11.029.
155. Qin, S., Bi, F., Gu, S., Bai, Y., Chen, Z., Wang, Z., Ying, J., Lu, Y., Meng, Z., Pan, H., Yang, P., Zhang, H., Chen, X., Xu, A., Cui, C., Zhu, B., Wu, J., Xin, X., Wang, J., Shan, J., Chen, J., Zheng, Z., Xu, L., Wen, X., You, Z., Ren, Z., Liu, X., Qiu, M., Wu, L., Chen, F.: Donafenib Versus Sorafenib in First-Line Treatment of Unresectable or Metastatic Hepatocellular Carcinoma: A Randomized, Open-Label, Parallel-Controlled Phase II-III Trial. J. Clin. Oncol. Off. J. Am. Soc. Clin. Oncol. 39, 3002–3011 (2021). https://doi.org/10.1200/JCO.21.00163.

156. Kudo, M., Ueshima, K., Yokosuka, O., Ogasawara, S., Obi, S., Izumi, N., Aikata, H., Nagano, H., Hatano, E., Sasaki, Y., Hino, K., Kumada, T., Yamamoto, K., Imai, Y., Iwadou, S., Ogawa, C., Okusaka, T., Kanai, F., Akazawa, K., Yoshimura, K.-I., Johnson, P., Arai, Y., SILIUS study group: Sorafenib plus low-dose cisplatin and fluorouracil hepatic arterial infusion chemotherapy versus sorafenib alone in patients with advanced hepatocellular carcinoma (SILIUS): a randomised, open label, phase 3 trial. Lancet Gastroenterol. Hepatol. 3, 424–432 (2018). https://doi.org/10.1016/S2468-1253(18)30078-5.
157. Lyu, N., Wang, X., Li, J.-B., Lai, J.-F., Chen, Q.-F., Li, S.-L., Deng, H.-J., He, M., Mu, L.-W., Zhao, M.: Arterial Chemotherapy of Oxaliplatin Plus Fluorouracil Versus Sorafenib in Advanced Hepatocellular Carcinoma: A Biomolecular Exploratory, Randomized, Phase III Trial (FOHAIC-1). J. Clin. Oncol. Off. J. Am. Soc. Clin. Oncol. 40, 468–480 (2022). https://doi.org/10.1200/JCO.21.01963.
158. Choi, Y.H., Zhang, C., Liu, Z., Tu, M.-J., Yu, A.-X., Yu, A.-M.: A Novel Integrated Pharmacokinetic-Pharmacodynamic Model to Evaluate Combination Therapy and Determine In Vivo Synergism. J. Pharmacol. Exp. Ther. 377, 305–315 (2021). https://doi.org/10.1124/jpet.121.000584.
159. Matsumoto, T., Masuo, Y., Tanaka, A., Kimura, T., Ioroi, T., Yamakawa, T., Kitahara, H., Kato, Y.: A physiologically based pharmacokinetic and pharmacodynamic model for disposition of FF-10832. Int. J. Pharm. 627, 122250 (2022). https://doi.org/10.1016/j.ijpharm.2022.122250.
160. Edginton, A.N., Zimmerman, E.I., Vasilyeva, A., Baker, S.D., Panetta, J.C.: Sorafenib metabolism, transport, and enterohepatic recycling: physiologically based modeling and simulation in mice. Cancer Chemother. Pharmacol. 77, 1039–1052 (2016). https://doi.org/10.1007/s00280-016-3018-6.
161. Zhang, L., Sinha, V., Forgue, S.T., Callies, S., Ni, L., Peck, R., Allerheiligen, S.R.B.: Model-based drug development: the road to quantitative pharmacology. J. Pharmacokinet. Pharmacodyn. 33, 369–393 (2006). https://doi.org/10.1007/s10928-006-9010-8.
162. Jain, L., Woo, S., Gardner, E.R., Dahut, W.L., Kohn, E.C., Kummar, S., Mould, D.R., Giaccone, G., Yarchoan, R., Venitz, J., Figg, W.D.: Population pharmacokinetic analysis of sorafenib in patients with solid tumours. Br. J. Clin. Pharmacol. 72, 294–305 (2011). https://doi.org/10.1111/j.1365-2125.2011.03963.x.
163. Mishra-Kalyani, P.S., Amiri Kordestani, L., Rivera, D.R., Singh, H., Ibrahim, A., DeClaro, R.A., Shen, Y., Tang, S., Sridhara, R., Kluetz, P.G., Concato, J., Pazdur, R., Beaver, J.A.: External control arms in oncology: current use and future directions. Ann. Oncol. Off. J. Eur. Soc. Med. Oncol. 33, 376–383 (2022). https://doi.org/10.1016/j.annonc.2021.12.015.
164. Booth, C.M., Cescon, D.W., Wang, L., Tannock, I.F., Krzyzanowska, M.K.: Evolution of the randomized controlled trial in oncology over

three decades. J. Clin. Oncol. Off. J. Am. Soc. Clin. Oncol. 26, 5458–5464 (2008). https://doi.org/10.1200/JCO.2008.16.5456.
165. Serrano, C., Rothschild, S., Villacampa, G., Heinrich, M.C., George, S., Blay, J.-Y., Sicklick, J.K., Schwartz, G.K., Rastogi, S., Jones, R.L., Rutkowski, P., Somaiah, N., Navarro, V., Evans, D., Trent, J.C.: Rethinking placebos: embracing synthetic control arms in clinical trials for rare tumors. Nat. Med. 29, 2689–2692 (2023). https://doi.org/10.1038/s41591-023-02578-z.
166. Sundaram, V., Selvaganesan, P., Deo, S., Karnib, M.: The importance of randomization in clinical research. Indian J. Thorac. Cardiovasc. Surg. 38, 562–565 (2022). https://doi.org/10.1007/s12055-022-01401-7.
167. Kumar, G., Chaudhary, P., Quinn, A., Su, D.: Barriers for cancer clinical trial enrollment: A qualitative study of the perspectives of healthcare providers. Contemp. Clin. Trials Commun. 28, 100939 (2022). https://doi.org/10.1016/j.conctc.2022.100939.
168. Unger, J.M., Vaidya, R., Hershman, D.L., Minasian, L.M., Fleury, M.E.: Systematic Review and Meta-Analysis of the Magnitude of Structural, Clinical, and Physician and Patient Barriers to Cancer Clinical Trial Participation. J. Natl. Cancer Inst. 111, 245–255 (2019). https://doi.org/10.1093/jnci/djy221.
169. Unger, J.M., Cook, E., Tai, E., Bleyer, A.: The Role of Clinical Trial Participation in Cancer Research: Barriers, Evidence, and Strategies. Am. Soc. Clin. Oncol. Educ. Book Am. Soc. Clin. Oncol. Annu. Meet. 35, 185–198 (2016). https://doi.org/10.1200/EDBK_156686.
170. FDA. 2001a. Guidance for Industry: E10 Choice of Control Group and Related Issues in Clinical Trials., https://www.fda.gov/media/71349/download.
171. FDA. 2019. Draft Guidance for Industry: Rare Diseases: Natural History Studies for Drug Development., https://www.fda.gov/regulatory-information/search-fda-guidance-documents/rare-diseases-natural-history-studies-drug-development.
172. Cowey, C.L., Mahnke, L., Espirito, J., Helwig, C., Oksen, D., Bharmal, M.: Real-world treatment outcomes in patients with metastatic Merkel cell carcinoma treated with chemotherapy in the USA. Future Oncol. Lond. Engl. 13, 1699–1710 (2017). https://doi.org/10.2217/fon-2017-0187.
173. Gökbuget, N., Kelsh, M., Chia, V., Advani, A., Bassan, R., Dombret, H., Doubek, M., Fielding, A.K., Giebel, S., Haddad, V., Hoelzer, D., Holland, C., Ifrah, N., Katz, A., Maniar, T., Martinelli, G., Morgades, M., O'Brien, S., Ribera, J.-M., Rowe, J.M., Stein, A., Topp, M., Wadleigh, M., Kantarjian, H.: Blinatumomab vs historical standard therapy of adult relapsed/refractory acute lymphoblastic leukemia. Blood Cancer J. 6, e473 (2016). https://doi.org/10.1038/bcj.2016.84.
174. Burger, H.U., Gerlinger, C., Harbron, C., Koch, A., Posch, M., Rochon, J., Schiel, A.: The use of external controls: To what extent can it currently be recommended? Pharm. Stat. 20, 1002–1016 (2021). https://doi.org/10.1002/pst.2120.

175. Pocock, S.J.: The combination of randomized and historical controls in clinical trials. J. Chronic Dis. 29, 175–188 (1976). https://doi.org/10.1016/0021-9681(76)90044-8.
176. Hobbs, B.P., Carlin, B.P., Mandrekar, S.J., Sargent, D.J.: Hierarchical commensurate and power prior models for adaptive incorporation of historical information in clinical trials. Biometrics. 67, 1047–1056 (2011). https://doi.org/10.1111/j.1541-0420.2011.01564.x.
177. Hobbs, B.P., Sargent, D.J., Carlin, B.P.: Commensurate Priors for Incorporating Historical Information in Clinical Trials Using General and Generalized Linear Models. Bayesian Anal. 7, 639–674 (2012). https://doi.org/10.1214/12-BA722.
178. Viele, K., Berry, S., Neuenschwander, B., Amzal, B., Chen, F., Enas, N., Hobbs, B., Ibrahim, J.G., Kinnersley, N., Lindborg, S., Micallef, S., Roychoudhury, S., Thompson, L.: Use of historical control data for assessing treatment effects in clinical trials. Pharm. Stat. 13, 41–54 (2014). https://doi.org/10.1002/pst.1589.
179. Chen, M.-H., Ibrahim, J.G.: Power prior distributions for regression models. Stat. Sci. 15, (2000). https://doi.org/10.1214/ss/1009212673.
180. Ibrahim, J.G., Chen, M.-H., Sinha, D.: On Optimality Properties of the Power Prior. J. Am. Stat. Assoc. 98, 204–213 (2003). https://doi.org/10.1198/016214503388619229.
181. Neuenschwander, B., Branson, M., Spiegelhalter, D.J.: A note on the power prior. Stat. Med. 28, 3562–3566 (2009). https://doi.org/10.1002/sim.3722.
182. Pan, H., Yuan, Y., Xia, J.: A Calibrated Power Prior Approach to Borrow Information from Historical Data with Application to Biosimilar Clinical Trials. J. R. Stat. Soc. Ser. C Appl. Stat. 66, 979–996 (2017). https://doi.org/10.1111/rssc.12204.
183. Schmidli, H., Gsteiger, S., Roychoudhury, S., O'Hagan, A., Spiegelhalter, D., Neuenschwander, B.: Robust meta-analytic-predictive priors in clinical trials with historical control information. Biometrics. 70, 1023–1032 (2014). https://doi.org/10.1111/biom.12242.
184. BCG report on Transforming Clinical Trials with Real-World Evidence, https://www.bcg.com/publications/2021/synthetic-control-arms-changing-clinical-trials.
185. Asar, Ö., Ritchie, J., Kalra, P.A., Diggle, P.J.: Joint modelling of repeated measurement and time-to-event data: an introductory tutorial. Int. J. Epidemiol. 44, 334–344 (2015). https://doi.org/10.1093/ije/dyu262.
186. Alsefri, M., Sudell, M., García-Fiñana, M., Kolamunnage-Dona, R.: Bayesian joint modelling of longitudinal and time to event data: a methodological review. BMC Med. Res. Methodol. 20, 94 (2020). https://doi.org/10.1186/s12874-020-00976-2.
187. Ibrahim, J.G., Chu, H., Chen, L.M.: Basic concepts and methods for joint models of longitudinal and survival data. J. Clin. Oncol. Off. J. Am. Soc. Clin. Oncol. 28, 2796–2801 (2010). https://doi.org/10.1200/JCO.2009.25.0654.

188. Rizopoulos, D., Ghosh, P.: A Bayesian semiparametric multivariate joint model for multiple longitudinal outcomes and a time-to-event. Stat. Med. 30, 1366–1380 (2011). https://doi.org/10.1002/sim.4205.
189. Rizopoulos, D., Molenberghs, G., Lesaffre, E.M.E.H.: Dynamic predictions with time-dependent covariates in survival analysis using joint modeling and landmarking. Biom. J. Biom. Z. 59, 1261–1276 (2017). https://doi.org/10.1002/bimj.201600238.
190. Andrinopoulou, E.-R., Rizopoulos, D., Takkenberg, J.J., Lesaffre, E.: Combined dynamic predictions using joint models of two longitudinal outcomes and competing risk data. Stat. Methods Med. Res. 26, 1787–1801 (2017). https://doi.org/10.1177/0962280215588340.
191. Kerioui, M., Mercier, F., Bertrand, J., Tardivon, C., Bruno, R., Guedj, J., Desmée, S.: Bayesian inference using Hamiltonian Monte-Carlo algorithm for nonlinear joint modeling in the context of cancer immunotherapy. Stat. Med. 39, 4853–4868 (2020). https://doi.org/10.1002/sim.8756.
192. Desmée, S., Mentré, F., Veyrat-Follet, C., Sébastien, B., Guedj, J.: Using the SAEM algorithm for mechanistic joint models characterizing the relationship between nonlinear PSA kinetics and survival in prostate cancer patients. Biometrics. 73, 305–312 (2017). https://doi.org/10.1111/biom.12537.
193. Kerioui, M., Bertrand, J., Bruno, R., Mercier, F., Guedj, J., Desmée, S.: Modelling the association between biomarkers and clinical outcome: An introduction to nonlinear joint models. Br. J. Clin. Pharmacol. 88, 1452–1463 (2022). https://doi.org/10.1111/bcp.15200.
194. Cerou, M., Thai, H.-T., Deyme, L., Fliscounakis-Huynh, S., Comets, E., Cohen, P., Cartot-Cotton, S., Veyrat-Follet, C.: Joint modeling of tumor dynamics and progression-free survival in advanced breast cancer: Leveraging data from amcenestrant early phase I-II trials. CPT Pharmacomet. Syst. Pharmacol. 13, 941–953 (2024). https://doi.org/10.1002/psp4.13128.
195. Kerioui, M., Beaulieu, M., Desmée, S., Bertrand, J., Mercier, F., Jin, J.Y., Bruno, R., Guedj, J.: Nonlinear Multilevel Joint Model for Individual Lesion Kinetics and Survival to Characterize Intra-Individual Heterogeneity in Patients with Advanced Cancer. Biometrics. 79, 3752–3763 (2023). https://doi.org/10.1111/biom.13912.
196. Krishnan, S.M., Laarif, S.S., Bender, B.C., Quartino, A.L., Friberg, L.E.: Tumor growth inhibition modeling of individual lesion dynamics and interorgan variability in HER2-negative breast cancer patients treated with docetaxel. CPT Pharmacomet. Syst. Pharmacol. 10, 511–521 (2021). https://doi.org/10.1002/psp4.12629.
197. Green, A.K., Reeder-Hayes, K.E., Corty, R.W., Basch, E., Milowsky, M.I., Dusetzina, S.B., Bennett, A.V., Wood, W.A.: The project data sphere initiative: accelerating cancer research by sharing data. The Oncologist. 20, 464-e20 (2015). https://doi.org/10.1634/theoncologist.2014-0431.
198. Petersson, K.J.F., Hanze, E., Savic, R.M., Karlsson, M.O.: Semiparametric distributions with estimated shape parameters.

Pharm. Res. 26, 2174–2185 (2009). https://doi.org/10.1007/s11095-009-9931-1.
199. Nathani, P., Gopal, P., Rich, N., Yopp, A., Yokoo, T., John, B., Marrero, J., Parikh, N., Singal, A.G.: Hepatocellular carcinoma tumour volume doubling time: a systematic review and meta-analysis. Gut. 70, 401–407 (2021). https://doi.org/10.1136/gutjnl-2020-321040.
200. Depaoli, S., Winter, S.D., Visser, M.: The Importance of Prior Sensitivity Analysis in Bayesian Statistics: Demonstrations Using an Interactive Shiny App. Front. Psychol. 11, 608045 (2020). https://doi.org/10.3389/fpsyg.2020.608045.
201. Convergence and efficiency diagnostics for Markov Chains, https://mc-stan.org/rstan/reference/Rhat.html.
202. Vehtari, A., Gelman, A., Gabry, J.: Practical Bayesian model evaluation using leave-one-out cross-validation and WAIC. Stat. Comput. 27, 1413–1432 (2017). https://doi.org/10.1007/s11222-016-9696-4.
203. Jacqmin-Gadda, H., Thiébaut, R., Chêne, G., Commenges, D.: Analysis of left-censored longitudinal data with application to viral load in HIV infection. Biostat. Oxf. Engl. 1, 355–368 (2000). https://doi.org/10.1093/biostatistics/1.4.355.